UNIVERSITÀ DEGLI STUDI DI PALERMO
Dottorato di Ricerca in Information and Communication Technologies
Dipartimento di Ingegneria
Settore Scientifico Disciplinare ING-INF/01

TRANSITION METAL OXIDES AS SELECTIVE CONTACTS FOR C-SI SOLAR CELLS

IL DOTTORE
ING. DANIELE SCIRE'

IL COORDINATORE
PROF.SSA ILENIA TINNIRELLO

IL TUTOR
PROF.SSA ISODIANA CRUPI

CICLO XXXIII
ANNO CONSEGUIMENTO TITOLO 2021

Summary

The production of energy from the combination of renewable sources can satisfy society's needs, providing a balanced and distributed energy supply. The exploitation of solar energy as a primary production source is gaining traction worldwide in response to the energy crisis, depletion of fossil fuel resources and environmental concerns due to greenhouse effects. The photovoltaic market is, indeed, rapidly growing with the crystalline silicon solar cell architecture dominating the technology field. In this context, the industrial and scientific community has a keen interest in increasing the cells' power conversion efficiency by developing new materials, highly efficient structures, and new manufacturing processes. The silicon heterojunction technology (HJT) employes a stack of hydrogenated amorphous silicon (a-Si:H) implementing the so-called passivating contacts, allowing for an efficient charge carrier collection and limiting, at the same time, the recombination losses. On the other hand, a-Si:H presents a sensible parasitic absorption of photons and a limited thermal budget. Other materials, such as the transition metal oxides (TMO), gained interest thanks to their excellent optoelectronic properties, granting for a low parasitic absorption, with low-cost and straightforward deposition processes.

After introducing the main issues related to the photovoltaics and the HJT solar cells in Chapter 1, Chapter 2 emphasizes the application and optimization of the TMOs in the solar cells architectures by reviewing the recent developments in crystalline silicon solar cells using transition metal oxides as carrier selective contacts. Specifically, the most recent improvements have been obtained with thin films of the sub-stoichiometric oxides of V_2O_5, MoO_3, WO_3, NiO, TiO_2, ZnO. The performances of the cells exploiting such contacts are compared in terms of Fill Factor (*FF*), short-circuit current density (J_{SC}), open-circuit voltage (V_{OC}) and efficiency (η). Furthermore, the technological point of view is addressed by comparing the employed deposition techniques.

Chapter 3 describes the main characterization techniques and equipment employed during this PhD research for the deposition and the characterization of the transition metal oxides.

Chapter 4 focuses on the role of molybdenum oxide as doping-free carrier selective contact in heterojunction solar cells. For modeling-based optimization of such contact, knowledge of the molybdenum oxide defect density of states (DOS) is crucial and a method to extract the defect density through nondestructive optical measures, including the contribution given by small polaron optical transitions, was developed and here reported. As

part of the analysis, molybdenum oxide samples have been evaluated after post-deposition thermal treatments. The oxide layers were deposited by thermal evaporation during the research period at the *Photovoltaic Materials and Devices group* at the Delft University of Technology.

Chapter 5 is dedicated to the role of titanium oxide as electron selective contact in heterojunction solar cells. Also, for this transition metal oxide, the knowelendge of the density of states is essential in order to optimize the cells implementing it. The titania films here characterized were deposited by pulsed laser deposition during the research period at the *Thin Film Laboratory* at the University of Palermo.

Chapter 6 reports the transition metal oxides for the selective carrier contact implemented in the crystalline silicon solar cells technology. However, the lack of optimization in these particular architectures results in inferior performing cells due to an S-shaped electrical characteristic. In this chapter, we fabricated solar cells showing S-shaped J-V curve. Therefore, an analysis of the reasons for such behavior was carried out using a model involving the series of a standard cell equivalent circuit with a Schottky junction to explain these atypical performances obtaining a good match of the experimental curves with the simulated curves. The parameters of the equivalent circuits are extrapolated and discussed focus on the reasons behind the low-performance cells and eventually give valuable information for the subsequent optimization process.

Sommario

La produzione di energia dalla combinazione di fonti rinnovabili può soddisfare le esigenze della società, fornendo un approvvigionamento energetico equilibrato e distribuito. L'utilizzo dell'energia solare come fonte di produzione primaria è in continua crescita in tutto il mondo in risposta alla crisi energetica, all'esaurimento delle risorse di combustibili fossili e alle giuste preoccupazioni sulle problematiche ambientali dovute all'inquinamento e all'effetto serra. Nel mercato fotovoltaico in rapida crescita, la tecnologia dominante è rappresentata dalle celle solari in silicio cristallino. In questo contesto, la comunità industriale e scientifica ha un deciso interesse nell'incrementare l'efficienza di conversione delle celle solari sviluppando nuovi materiali, strutture altamente efficienti e nuovi processi di fabbricazione. La tecnologia delle celle al silicio ad eterogiunzione (HJT) impiega una stratificazione di silicio amorfo idrogenato (a-Si:H) che implementa i cosiddetti contatti passivanti e selettivi, i quali consentono una raccolta efficiente dei portatori di carica e limitando, allo stesso tempo, le perdite di ricombinazione. Inoltre, il silicio amorfo idrogenato è caratterizzato da assorbimenti parassiti e limitato budget termico. Un'alternativa molto interessante Altri materiali, come gli ossidi dei metalli di transizione (TMO), hanno raccolto interesse grazie alle loro eccellenti proprietà optoelettroniche, che garantiscono un basso assorbimento parassitario, con processi di deposizione semplici ed economici.

Dopo aver introdotto le nozioni principali del fotovoltaico e delle celle solari HJT nel Capitolo 1, il Capitolo 2 esamina l'applicazione e l'ottimizzazione dei TMO nelle celle solari enfatizzando i recenti sviluppi di tali materiali nelle celle al silicio cristallino. Nello specifico sono trattati i seguenti ossidi: V_2O_5, MoO_3, WO_3, NiO, TiO_2, ZnO. Le prestazioni delle celle che sfruttano tali contatti sono confrontate in termini di fattore di riempimento (*FF*), densità di corrente di cortocircuito (J_{SC}), tensione a circuito aperto (V_{OC}) ed efficienza (η). Infine, vengono confrontate e discusse le tecniche di deposizione impiegate.

Il Capitolo 3 descrive le principali tecniche di caratterizzazione e le apparecchiature utilizzate durante il dottorato per la realizzazione e lo studio degli ossidi dei metalli di transizione.

Il Capitolo 4 si concentra sul ruolo dell'ossido di molibdeno come contatto selettivo *doping-free* nelle celle solari a eterogiunzione. Per l'ottimizzazione dei contatti basati su questo materiale, la conoscenza della densità degli stati dovuti ai difetti (DOS) è fondamentale. Per questo, è stato sviluppato un metodo per estrapolare la DOS attraverso

misure ottiche non distruttive, includendo il contributo dato alle transizioni ottiche dai polaroni. I film sono stati depositati per evaporazione termica durante il periodo di ricerca effettuato presso il *Photovoltaic Materials and Devices group* della Delft University of Technology.

Il Capitolo 5, invece, è dedicato al ruolo dell'ossido di titanio come contatto selettivo degli elettroni nelle celle solari a eterogiunzione. Anche per questo ossido, la conoscenza della densità degli stati è essenziale per l'ottimizzazione delle celle che lo implementano. I film di titania sono stati depositati mediante *pulsed laser deposition* eseguita durante il periodo di ricerca presso il *Thin Film Laboratory* dell'Università di Palermo.

Il Capitolo 6 riporta l'implementazione degli ossidi di metalli di transizione nella tecnologia delle celle solari al silicio cristallino. Tuttavia, la mancanza di ottimizzazione in questa particolare architettura si traduce in celle con prestazioni inferiori a causa di una caratteristica elettrica a forma di S. Per spiegare queste prestazioni atipiche, è stata effettuata un'analisi delle ragioni di tale comportamento utilizzando un modello che coinvolge la serie di un circuito equivalente di cella standard con una giunzione Schottky, ottenendo una buona corrispondenza tra curve sperimentali e le curve simulate. I parametri dei circuiti equivalenti sono estrapolati e discussi evidenziando i motivi che stanno alla base delle basse prestazioni fornendo, infine, delle preziose informazioni per il successivo processo di ottimizzazione delle celle solari.

Contents

1 Introduction 1

1.1 Solar energy conversion 2

1.1.1 Loss mechanisms 3

1.1.2 Equivalent circuit model 4

1.2 c-Si solar cell architecture 6

1.2.1 c-Si heterojunction technology 7

References 10

2 Background on the Transition Metal Oxides 17

2.1 TMO as hole selective contact 17

2.1.1 Molybdenum trioxide 18

2.1.2 Tungsten trioxide 21

2.1.3 Vanadium pentoxide 22

2.1.4 Nickel oxide 24

2.2 TMO as electron selective contact 26

2.2.1 Titanium dioxide 27

2.2.2 Zinc Oxide 29

2.3 Conclusions 31

References 33

3 Experimental Details 38

3.1 TMO fabrication methods 38

3.1.1 Thermal evaporation 38

3.1.2 Pulsed laser deposition 40

3.1.3 RF plasma enhanced chemical vapor deposition 41

3.2 TMO characterization techniques 42

3.2.1 X-ray photoelectron spectroscopy 42

3.2.2 Spectroscopic ellipsometry 44

3.2.3 Raman spectroscopy 44
3.2.4 Photothermal deflection spectroscopy 45
References 47
4 Density of States in Molybdenum Oxide 49
4.1 Introduction 49
4.2 Methodology 50
4.2.1 Density of States evaluation 50
4.2.2 Experimental details 52
4.3 Results and discussion 53
4.3.1 Chemical and structural properties 53
4.3.2 Opto-electrical characterization 55
4.3.3 Application in HJT solar cells 62
4.4 Conclusions 63
References 64
5 Density of States in Titanium Oxide 73
5.1 Introduction 73
5.2 Methodology 74
5.2.1 Density of states evaluation 74
5.2.2 Experimental details 75
5.3 Results and discussion 76
5.3.1 Chemical and structural characterization 76
5.3.2 Optical characterization 79
5.4 Conclusions 85
References 86
6 TMO Application in HJT Cells 92
6.1 Introduction 92
6.2 Experimental details 93
6.3 Optoelectrical characterization 95

6.3.1 Film characterization 95
6.4 Solar cell parameters extraction 100
6.4.1 Theoretical model 100
6.4.2 Parameters extraction 102
6.5 Conclusions 105
References 106
7 Conclusions 110
List of the Figures 112
List of the Tables 115
List of the Equations 116
Acknowledgement 117

1 Introduction

Renewable solar energy production is gaining traction worldwide in response to the energy crisis, depletion of fossil fuel resources and environmental concerns due to greenhouse effects. Indeed, the photovoltaic (PV) market is rapidly growing [1] with commercially available solar cells predominantly made of crystalline silicon (c-Si) [2], which is an abundant material, relatively cheap and easy to process. Furthermore, with thin-film technology, lighter cells are obtained, saving material and enabling for flexible substrates and opening new frontiers in the application field.

The industrial and scientific community has a keen interest in further increasing the power conversion efficiency by developing new materials, highly efficient structures and new manufacturing processes. Indeed, industrial-grade solar cells have overcome the 24% mark [3] with PERC (passivated emitter rear cell) architecture and the 25% mark [4, 5] with silicon heterojunction technology (HJT). The latter one combines the advantages of thin-film silicon technology with a c-Si absorber to selectively collect the generated carriers. By employing the so-called passivating contacts, the HJT technology allows collecting the charge carriers efficiently limiting, at the same time, the recombination losses [6, 7].

Typically, HJT are made of a stack of hydrogenated amorphous silicon (a-Si:H) [8–11] for surface passivation and doped layers that allow high open-circuit voltage, V_{OC}, in solar cells leading to record efficiencies, η, above 26% [11, 12]. On the other hand, a-Si:H presents a sensible parasitic absorption of photons [13] and a limited thermal budget [7]. Besides, a-Si:H is also a relatively poor conductor, suffering from high recombination. As an alternative, other materials gained interest, such as the transition metal oxides (TMO); indeed, TMO presents excellent optoelectronic properties granting for a low parasitic absorption [14]. Moreover, TMOs deposition can be carried out with simple and low-cost processes [15].

In this chapter an overview of topics from PV and HJT is discussed, providing a solid background for the original results presented in the following chapters.

1.1 Solar energy conversion

The photovoltaic effect describes the conversion of light into electric current. It exploits the energy of a photon incident on a semiconductor to excite an electron from an initial energy level E_i to a higher energy level E_f, as shown in Figure 1.1a. Photons can only be absorbed if the energy levels E_i and E_f are such that their difference is equal to the energy of the photon, $E_{ph} = E_f - E_i$. If a photon with energy smaller than the bandgap E_G reaches the semiconductor, it will not be absorbed but will pass through the material without interaction. An electron, which is excited from E_i to E_f, generates a hole on E_i, which behaves like a positive elementary charge. The absorption of a photon, therefore, leads to the formation of an electron-hole pair. If the incident photon has an energy greater than E_G, an electron-hole pair is generated and part of the energy is lost in the form of heat (thermalization), as shown in Figure 1.1b.

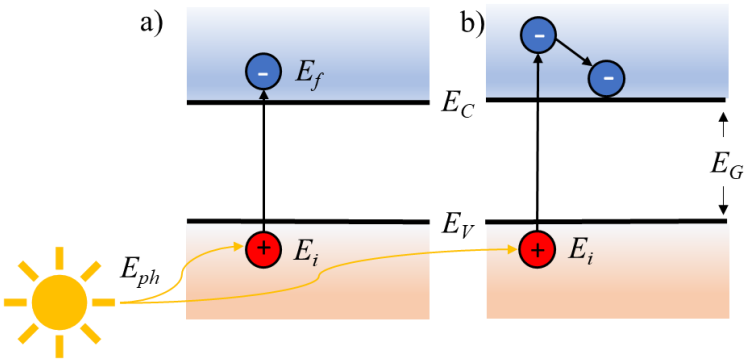

Figure 1.1 *Photon absorption in a semiconductor: a) photon energy E_{ph} equal to E_G; b) E_{ph} greater than E_G*

The maximum conversion efficiency from radiative energy to chemical energy is limited by thermodynamics, the efficiency of which has been calculated at 67% for the sun's unconcentrated black body radiation and 85% for full concentrated sunlight [16], taking into account that the photon energy conversion can yield more than one electron-hole pair [17]. Usually, the electron-hole pair recombines, meaning the electron will fall back to the initial energy level E_i. The excess of energy will then be released in lattice vibrations, emitted as a photon or transferred to other charge carriers. An electric field can be exploited to separate the electron-hole pair, effectively extracting their energy by generating a current. A p-n junction forms the simplest solar cell: electrons and holes diffuse and recombine at the interface, creating the so-called depletion zone; in such a region, the absence of the charge carrier forms an electric field that contrasts the charge diffusion until a dynamic equilibrium is reached. As long as the cell is under illumination, the photo-generated pairs in the depletion zone are separated by the electric field, providing the expected flow of electrons.

The photons absorbed outside the depletion zone will also be converted into electron-hole pairs, but since the internal electric field does not accelerate them, the probability of recombination will be higher. The photo-generated current then flows to an external circuit until they get collected by the other contact of the solar cell device, where they finally recombine with the holes (Figure 1.2).

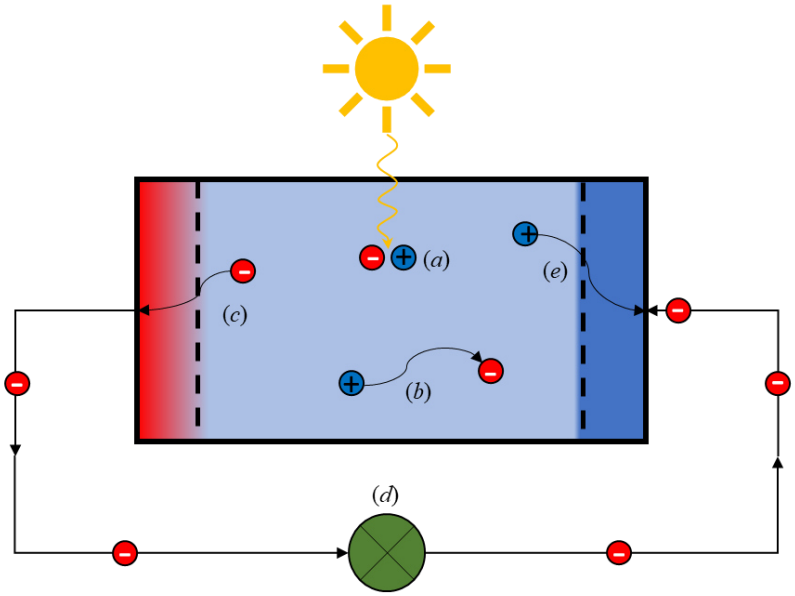

Figure 1.2 *Photogenerated carriers behavior inside a p-n junction: a) generation of electron-hole pairs from photon absorption; b) recombination losses; c) separation and emission of electrons; d) the electrons flow through the external circuit e) hole collection at the back contact.*

1.1.1 Loss mechanisms

The study of the loss mechanisms is the foremost essential for solar cell design, leading to the design rules to optimize the material, efficiently exploit the spectrum and adopt adequate light management. Indeed, solar cell performances depend on the intrinsic one-dimensional diode efficiency and the extrinsic losses (i.e., contact shadowing, series resistance, losses arising from nonuniform illumination, to cite a few).

The main contributions to the efficiency cutback are:

- Series resistance: the contacts form a parasitic series resistance at the interface between the silicon and the metal, which, of course, causes dissipation by Joule's effect, reducing effectively the power transferred to the external circuit. In polycrystalline silicon cells, this effect is further enhanced due to boundaries between the crystal grains.
- Shunt resistance: the voltage output of the cell is reduced by a leakage current caused by a current flowing through local defects in the junction or at the edges

of the solar cell.

- Parasitic recombination: the photo-generated electron-hole pairs are excess carriers and can recombine before being collected by the contacts and delivered to the external circuit; indeed, in the path from the generation point towards the junction, they can meet charges of opposite sign or trap states and recombine.
- Shading: due to the contact on the front side, the light transmission is limited, reducing the number of photons reaching the junctions and being converted into hole-electron pairs.
- Reflection: the solar cell architecture comprises different layers, each with a different reflectivity (wavelength-dependent), so that part of the incident energy is not transmitted and absorbed in the junction underneath.
- Solar spectrum mismatch: the sunlight has a broad spectrum, ranging from ultraviolet to infrared rays, but only the photons with energy higher than the absorption material bandgap generate electron-hole pairs; their excess energy is lost as heat, *thermalization losses*. Photons with energy lower than the bandgap are not absorbed and their energy is lost, *transmission lost*.

1.1.2 Equivalent circuit model

The DC electrical characteristic of a cell under illumination is given in terms of output current, *I,* and output voltage, *V*. Several models have been developed to describe the *I-V* curve of a solar cells depending on its architecture and behavior. If the device behaves under illumination as an ideal diode, it is possible to use the simple single diode model, including the losses (1.1) shown in the equivalent circuit in Figure 1.3.

$$I(V) = I_0 \left[\exp\left(\frac{q(V - I \cdot R_S)}{k_B T}\right) - 1\right] + \frac{V - I \cdot R_S}{R_P} - I_{ph} \tag{1.1}$$

Such model comprises constants (the electron charge q, the temperature T and the Boltzmann's constant K_B) and five parameters: the photogenerated current I_{ph}, the reverse saturation current I_o, the diode ideality factor n, the series resistance R_S and the shunt resistance R_P.

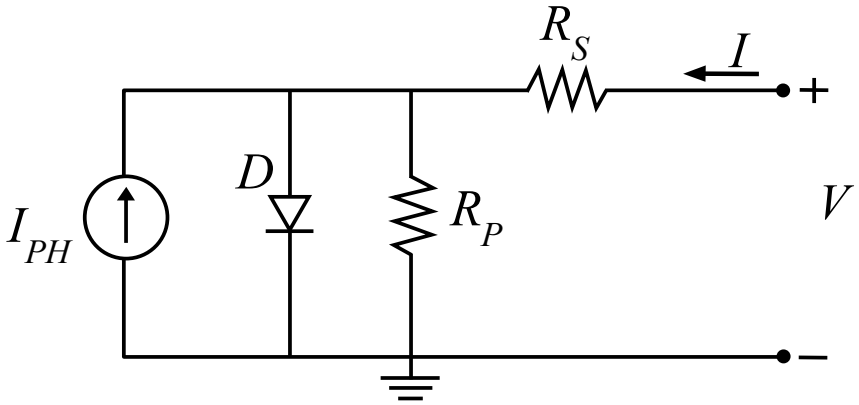

Figure 1.3 *Equivalent circuit of a solar cell based on the single diode model*

The parallel resistance represents a conductive path through the solar cell edges determining a leakage current. Instead, the series resistance represents the voltage drop across the metal contacts. An increase in R_s results in a reduction in the output voltage, while a decrease in R_p reduces the output current. In this simplified model, high-quality solar cells present a low series resistance (≈ 0), a high shunt resistance ($\approx \infty$) and an ideality factor close to 1.

Figure 1.4 shows the typical DC characteristic of a solar cell under illumination from which several performances index can be derived. For standardization purposes, this electrical measurement is done under the so-called *standard test condition* (STC) at a fixed device temperature (25°C) illuminated by AM1.5 (solar zenith angle 48.19°) spectrum with a total irradiance of 1000 W/m^2.

- I_{SC}: the *short-circuit current*; it is the maximum current through the external circuit when the voltage across the solar cell is zero. It depends on the incident radiative energy investing the solar cell and on the solar cell area;
- V_{OC}: the *open-circuit voltage*; it is the maximum voltage across the solar cell when no current passes through. It depends on the photo-generated current and on the saturation current.
- P_{MPP}: the *maximum power point*; it is found at the peak point of the power-voltage (P-V) characteristic where the cell gives its best performances ($P_{max} = V_{MPP}\, I_{MPP}$).
- *FF*: the *fill factor*; it is defined as the ratio between P_{max} and V_{OC} product with I_{SC}. This factor is a measure of the squareness of the *I-V* characteristics.
- η: the *conversion efficiency*; it is defined as the ratio between the maximum output power and the incident power under STC. The latter is obtained by multiplying the irradiance by the solar cell area.

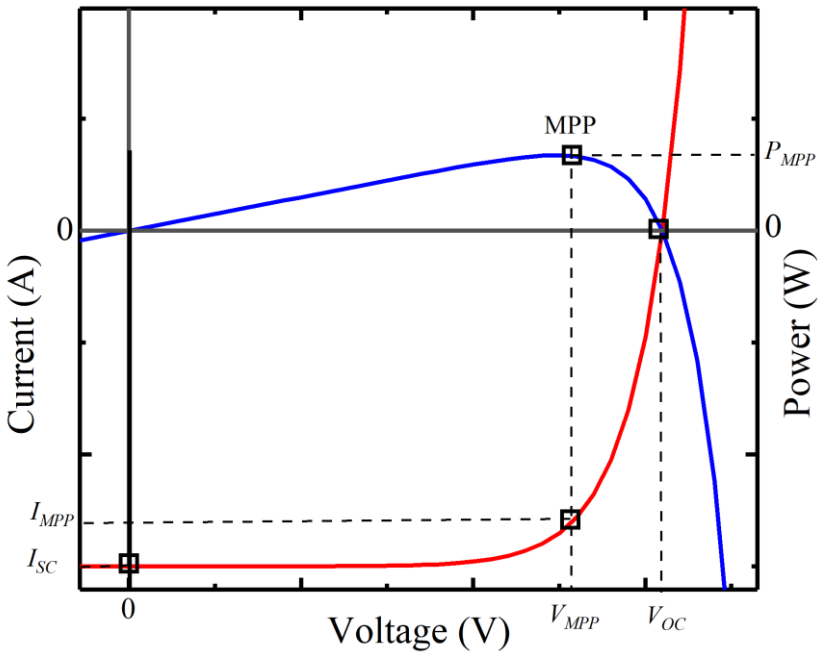

Figure 1.4 *I-V characteristic of a typical solar cell under illumination (red line); P-V characteristic (blue line) with the maximum power point (MPP).*

Another essential parameter is the EQE (*External Quantum Efficiency*), which measures the number of photons incident on the solar cell converted into electron-hole pairs. It depends on the wavelength and is evaluated by illuminating the solar cell with monochromatic light of wavelength λ and measuring the resulting photocurrent $I(\lambda)$ as expressed in (1.2).

$$EQE(\lambda) = \frac{I(\lambda)}{q\,\Psi(\lambda)} \tag{1.2}$$

where Ψ(λ) is the spectral photon flow. It should be remarked that the measured current depends on the bias voltage; therefore, the measurements is carried out at a fixed voltage.

1.2 c-Si solar cell architecture

The basic structure of a crystalline silicon (c-Si) solar cell is sketched in Figure 1.5. It is formed by a layer of an n-type semiconductor (the emitter) on top of a p-doped semiconductor (the *absorber*). Most industrial solar cells are produced from p-type silicon wafers, typical thicknesses between 100 and 300 μm, grown by the Czochralski method (crystalline) or by *silicon casting* (polycrystalline) [18]. The emitter layer on the front is a film of about 300 nm. Indeed, since most of the light is absorbed in the front of the solar cell, a thin emitter layer allows that charge generation occurs within the diffusion length of the p-n junction, limiting the parasitic absorption of light. Simultaneously, the reflection losses are

minimized by applying an anti-reflective coating (ARC) [18], generally made of SiO, SiO_2, SiN_x, TiO_2, Al_2O_3 or ZnS [19].

The solar cell is completed by two metal contacts on the front and the back of the device. The best collection of carriers is achieved with an ohmic contact; therefore, the *work function* (*WF*) of the metal needs to be compatible with the semiconductor *electronic affinity* (χ) [20]. If this requirement is not fulfilled, a *Schottky* barrier is formed, limiting the charge transport and ruining the performance of the cell. Typically, the materials used for the metal contacts are Cu, Ag, Al [21]. The front metal contact, acting as unwelcome shading object, are generally optimized by implementing specific geometry as bus-bar and fingers in an H-grid pattern. The back contact is generally a direct deposition of metal without any particular geometry; a *Back Surface Field* (BSF) can also be implemented to limit the recombination losses by heavily *p*-doping the interface with the back. Since the absorber is a *p*-type wafer, the presence of a heavily doped (p^+) region introduces an *n-p* junction, which acts as a barrier preventing minority electrons in the *p* zone from spreading and recombine to the back surface [18].

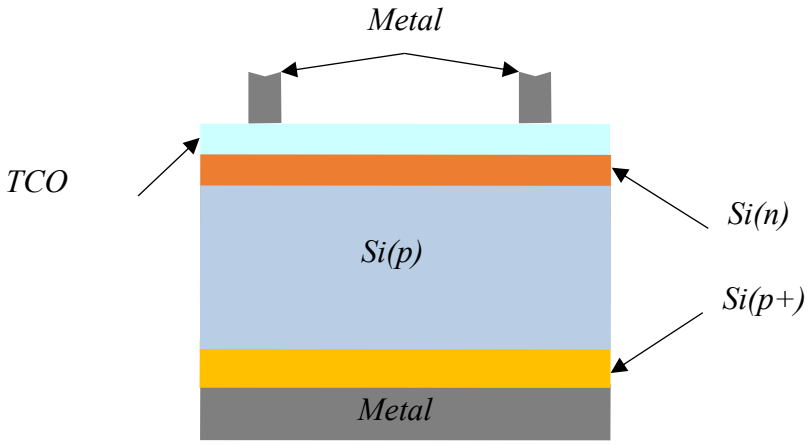

Figure 1.5 *Architecture of a simple solar cell*

1.2.1 c-Si heterojunction technology

A promising innovation in the photovoltaic field is given by the HJT (Heterojunction Technology), with several industries and research centers investing in developing such technology, such as Enel Green Power, which set up an automated 200MWp/y production line in 2019 under the European Union's Horizon 2020 research and innovation program [22].

The first heterojunction solar cell was introduced in 1983 [23] as a bottom cell in a tandem junction solar cell. Later, Sanyo (now Panasonic Sanyo) developed a more advanced

structure including a thin buffer layer of undoped hydrogenated amorphous silicon (a-Si:H) between the c-Si wafer and doped a-Si:H layer [24], obtained the so-called *heterojunction intrinsic thin-layer* (HIT) solar cell. The passivating selective contacts are an essential element of this architecture, reducing the recombination processes and allowing high efficiencies.

A typical structure of a modern heterojunction solar cell is schematized in Figure 1.6. It consists of a c-Si wafer passivated on both sides with thin layers of intrinsic hydrogenated amorphous silicon (a-Si:H(i)). These layers are subsequently *p*-doped and *n*-doped to form the front emitter and the Back Surface Field. The thickness of the a-Si:H(i) layer is optimized to achieve good passivation of the absorber limiting the losses introduced by its low conductivity. The thickness of the doped a-Si:H layer is also designed to be as thin as possible to prevents parasitic absorption. The absorber is made of high-quality *n*-doped silicon with a thickness of around 300µm. The front contact (designed with a grid pattern) is deposited on top of a transparent conductive oxide (TCO), which improves the surface conductivity and acts as an anti-reflection coating.

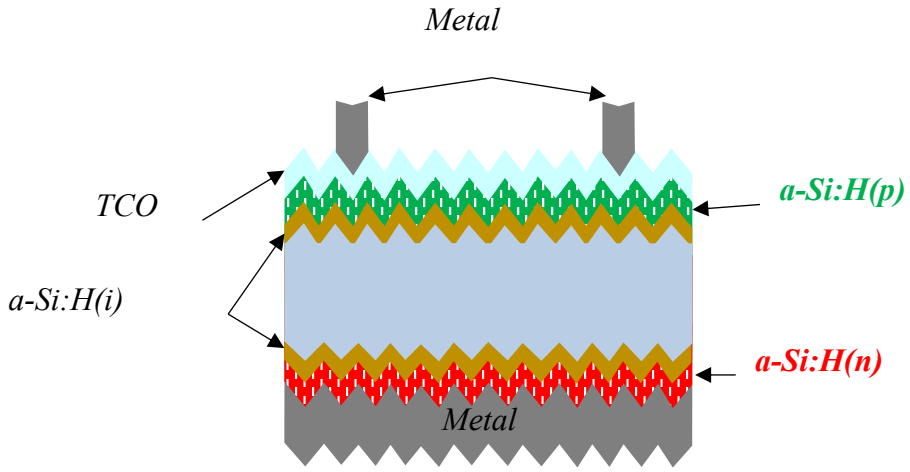

Figure 1.6 *Schematic of a heterojunction solar cell*

The primary source of defects in the heterojunction cell is attributed to the *dangling bonds,* i.e., interrupted atomic bonds on the surface of the crystalline silicon. Indeed, in c-Si, each silicon atom is bonded with four other silicon atoms, whereas on the surface, one of the bonds is missing producing an unpaired electron (dangling bonds). The dangling bonds at the interface cause recombination losses being essentially trap-centers for carriers and limit the solar cell performances. A response to this problem is the *field-effect passivation,* which reduces excess carrier concentration by introducing an embedded electric field; it is obtained by placing a highly doped a-Si:H(n) on the c-Si [25]. Another strategy is the *chemical passivation*, achieved by inserting a thin film of a-Si:H(i) at the interface between the emitter

and c-Si. The hydrogen atoms of a-Si:H bind to the available bonds, reducing the dangling bonds substantially. This technique grants a low surface recombination rate yielding solar cells with open-circuit voltages above 750 mV [26].

The band diagram of a heterojunction silicon solar cell is shown in Figure 1.7. It is worth noting that the electron transport is blocked by the high energy barrier from the absorber to the emitter while the photogenerated holes are trapped in an energy well. This energy well limits the collection of holes; on the other hand, holes can overcome the thin a-Si:H(i) layer thanks to thermionic emission, direct tunneling, or trap-assisted tunneling (TAT). The backside situation is reverted with a high barrier preventing holes diffusion and a small energy barrier for the electrons. Nonetheless, this barrier is not a limit for electron transport, which occurs by tunneling effect.

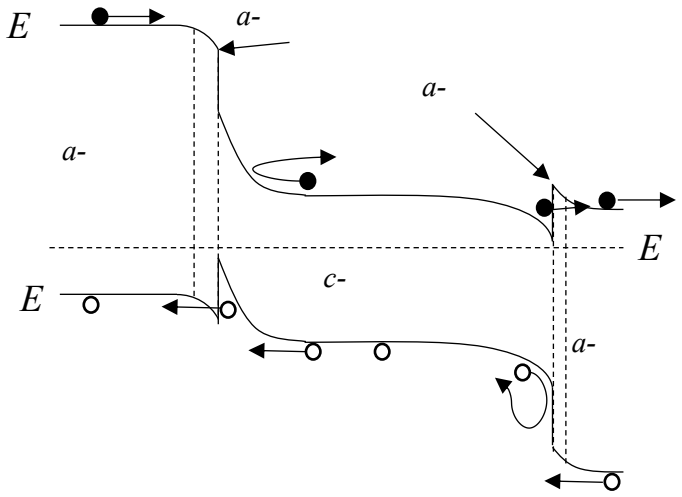

Figure 1.7 *Band diagram of a typical HJT cell*

In summary, the a-Si:H(i-n/p) interfaces act as carrier selective contacts (CSCs), providing passivation and allowing the transport of only one type of carrier. Nevertheless, hydrogenated amorphous silicon presents some disadvantages, such as the limited thermal [13] budget and the parasitic absorption introduced by large defects concentration [7]. Moreover, some concerns are related to the use of toxic and flammable precursors in the Plasma Enhanced Chemical Vapor Deposition (PECVD) process used to grown the doped a-Si:H layers [27]. In this context, the transition metal oxides, which present remarkable optoelectronic properties, including low parasitic absorption, are gaining particular interest to replace the doped amorphous silicon layer [14]. Moreover, some of the involved deposition methods require low-cost processes and materials [15].

A review of some of the best cells obtained exploiting TMO as carrier selective contact will be discussed in the next chapter of this thesis.

References

[1] ITRPV, "International Technology Roadmap for Photovoltaic", October 2020.

[2] S. Philipps, "Photovoltaics Report 2020," Fraunhofer Institute for Solar Energy Systems ISE, 2020. [Online]. Available: https://www.ise.fraunhofer.de/content/dam/ise/de/documents/publications/studies/Photovoltaics-Report.pdf. [Accessed: 08-Jun-2020].

[3] LONGi solar, "LONGi Solar sets new bifacial mono-PERC solar cell world record at 24.06 percent," 2019. [Online]. Available: https://en.longi-solar.com/home/events/press_detail/id/89.html. [Accessed: 08-Jun-2020].

[4] D. Chen *et al*., "Defect engineering of p-type silicon heterojunction solar cells fabricated using commercial-grade low-lifetime silicon wafers", Prog. Photovoltaics Res. Appl., 2019, doi: https://doi.org/10.1002/pip.3230.

[5] B. Asaba, "Hanergy's SHJ Technology achieves 25.11% Conversion Efficiency," 2019. [Online]. Available: https://www.arabianindustry.com/utilizzties/news/2019/nov/19/hanergys-shj-technology-achieves-2511-conversion-efficiency-6269848/. [Accessed: 08-Jun-2020].

[6] S. De Wolf, A. Descoeudres, Z. C. Holman, and C. Ballif, "High-efficiency Silicon Heterojunction Solar Cells: A Review", *Green*, vol. 2, no. 1, pp. 7–24, Jan. 2012, doi: https://doi.org/10.1515/green-2011-0018.

[7] J. Melskens, B. W. H. Van De Loo, B. Macco, L. E. Black, S. Smit, and W. M. M. Kessels, "Passivating Contacts for Crystalline Silicon Solar Cells: From Concepts and Materials to Prospects*", IEEE J. Photovoltaics*, vol. 8, no. 2, pp. 373–388, 2018 doi: https://doi.org/10.1109/JPHOTOV.2018.2797106.

[8] K. Masuko *et al.,* "Achievement of more than 25% conversion efficiency with crystalline silicon heterojunction solar cell", *IEEE J. Photovoltaics,* vol. 4, no. 6, pp. 1433–1435, 2014, doi: https://doi.org/10.1109/JPHOTOV.2014.2352151.

[9] H. A. Gatz, J. K. Rath, M. A. Verheijen, W. M. M. Kessels, and R. E. I. Schropp, "Silicon heterojunction solar cell passivation in combination with nanocrystalline silicon oxide emitters", *Phys. Status Solidi*, vol. 213, no. 7, pp. 1932–1936, Jul. 2016, doi: https://doi.org/10.1002/pssa.201532945.

[10] G. Yang *et al.,* "High-efficiency black IBC c-Si solar cells with poly-Si as carrier-selective passivating contacts", *Sol. Energy Mater. Sol. Cells*, vol. 186, pp. 9-13, 2018 doi: https://doi.org/10.1016/j.solmat.2018.06.019.

[11] K. Yoshikawa *et al.,* "Silicon heterojunction solar cell with interdigitated back contacts for a photoconversion efficiency over 26%", *Nat. Energy*, vol. 2, no. 5, May 2017, doi: https://doi.org/10.1038/nenergy.2017.32.

[12] M. A. Green *et al*., "Solar cell efficiency tables (version 49)", *Prog. Photovoltaics Res. Appl.,* vol. 25, no. 1, pp. 3–13, 2017, doi: https://doi.org/10.1002/pip.2855.

[13] Z. C. Holman *et al.,* "Current Losses at the Front of Silicon Heterojunction Solar Cells", *IEEE J. Photovoltaics*, vol. 2, no. 1, pp. 7–15, Jan. 2012, doi: https://doi.org/10.1109/JPHOTOV.2011.2174967.

[14] L. G. Gerling *et al*., "Transition metal oxides as hole-selective contacts in silicon heterojunctions solar cells", *Sol. Energy Mater. Sol. Cells*, vol. 145, pp. 109–115, 2016, doi: https://doi.org/10.1016/j.solmat.2015.08.028.

[15] C. Yu, S. Xu, J. Yao, and S. Han, "Recent advances in and new perspectives on crystalline silicon solar cells with carrier-selective passivation contacts", *Crystals*, vol. 8, no. 11, 2018, doi: https://doi.org/10.3390/cryst8110430.

[16] R. Brendel, Jürgen H. Werner, H. J. Queisser, "Thermodynamic efficiency limits for semiconductor solar cells with carrier multiplication", *Solar Energy Materials and Solar Cells*, vol. 41–42, pp. 419–425, Jun. 1996, doi: https://doi.org/10.1016/0927-0248(95)00125-5.

[17] S. Kolodinski, J. H. Werner, T. Wittchen, and H. J. Queisser, "Quantum efficiencies exceeding unity due to impact ionization in silicon solar cells", *Applied Physics Letters*, vol. 63, no. 17, pp. 2405-2407, Oct. 1993, doi: https://doi.org/10.1063/1.110489.

[18] K. Jäger, O. Isabella, A. Smets, R. Van Swaaij, and M. Zeman, "Crystalline silicon solar cells" in *Solar Energy - The physics and engineering of photovoltaic conversion, technologies and systems*, Cambridge, U.K.: UIT Cambridge, 2016, ch. 12, pp. 153-176.

[19] A. Uzum, *et al*., "Sprayed and Spin-Coated Multilayer Antireflection Coating Films for Nonvacuum Processed Crystalline Silicon Solar Cells", *Hindawi International Journal of Photoenergy,* vol. 2017, 2017, doi:

https://doi.org/10.1155/2017/3436271.

[20] S.M. Sze and Kwok K. Ng, *Physics of Semiconductor Devices*, 3rd edition, 2007 John Wiley & Sons, Inc., April 10th, 2006, doi: 10.1002/0470068329, doi: https://doi.org/10.1002/0470068329.

[21] A. Ebong and N. Chen, "Metallization of crystalline silicon solar cells: A review", in *High Capacity Optical Networks and Emerging/Enabling Technologies*, Istanbul, 2012, pp. 102-109, doi: https://doi.org/10.1109/HONET.2012.6421444.

[22] Ampere project, "AMPERE 200MWp/y HeteroJunction (HJT) Solar Cell and Module Manufacturing Line". [Online]. Available: https://ec.europa.eu/info/funding-tenders/opportunities/portal/screen/opportunities/horizon-results-platform/23809;needList=7 [Accessed: 02-Oct-2020]

[23] K. Okuda, H. Okamoto, and Y. Hamakawa, "Amorphous Si/polycrystalline Si stacked solar cell having more than 12% conversion efficiency", *Japanese Journal of Applied Physics*, vol. 22, no. 9A, pp. L605–L607, 1983 doi: https://doi.org/10.1143/JJAP.22.L605.

[24] M. Tanaka *et al*., "Development of new a-Si/c-Si heterojunction solar cells: ACJ-HIT (artificially constructed junction-heterojunction with intrinsic thin-layer)", *Japanese Journal of Applied Physics,* vol. 31, no. Part 1, No. 11, pp. 3518–3522, 1992, doi: https://doi.org/10.1143/JJAP.31.3518.

[25] B. Hoex, J. J. H. Gielis, M. C. M. van de Sanden, and W. M. M. Kessels, "On the c-Si surface passivation mechanism by the negative-charge-dielectric Al2O3", *Journal of Applied Physic*s, vol. 104, no. 11, Dec 2008, doi: https://doi.org/10.1063/1.3021091.

[26] C. Battaglia, A. Cuevas, and S. De Wolf, "High-efficiency Crystalline Silicon Solar Cells: Status and Perspectives", *Energy Environ. Sci*., vol. 9, no. 5, pp. 1552-1576, 2016, doi: https://doi.org/10.1039/C5EE03380B.

[27] S. Sanyal *et al*., "Hole Selective Contacts: A Brief Overview", *Current Photovoltaic Research*, vol. 7, no. 1, pp. 9-14, 2019, doi: https://doi.org/10.21218/CPR.2019.7.1.009.

2 Background on the Transition Metal Oxides

Several attempts have been conducted in the last decades to improve the modern crystalline silicon solar cell in terms of efficiency, impact factor and power output; a major breakthrough in the photovoltaic field was given by the development of passivated selective contacts resulting in great improvement of the solar cells performances [1]. Many materials are adequate for this purpose; among these, thin films of a-Si:H have taken the lead. However, the performance limitations introduced by the relatively high optical absorption and recombination losses of a-Si:H led to a study of novel types of heterojunction between c-Si and high transparency transition metal oxides (TMO). TMOs have recently been shown to be a viable alternative to doped amorphous silicon layers in HJT, thanks to their wide range of working function in the range of 3–7 eV, the high transparency (E_G> 3eV) and the natural presence of p/n-type doping without any additional processing. Furthermore, they can be deposited at a temperature lower than 200 °C, increasing the simplification of the process and reducing costs. Nevertheless, TMO can also passivate the c-Si surface, making them excellent candidates for passivating selective contacts rising the scientific community's interest, with several research groups involved in their application in PV [2-10].

In this chapter, recent developments in crystalline silicon solar cells using transition metal oxides as carrier selective contact are reviewed. Specifically, the most recent improvements have been obtained with thin films of the sub-stoichiometric oxides of V_2O_5, MoO_3, WO_3, NiO, TiO_2, ZnO. The performances of the cells exploiting such contacts are compared in terms of Fill Factor (FF), short-circuit current density (J_{SC}), open-circuit voltage (V_{OC}) and efficiency (η). Furthermore, the technological point of view will also be addressed by comparing the employed deposition techniques.

2.1 TMO as hole selective contact

The working principle of TMO-based *p*-contact relies on the extensive work function of the TMOs and the native *n*-doping of such material, which contributes to the band bending at the interface with the absorber. Figure 2.1 depicts the energy band diagram of a solar cell exploiting a-Si:H(i)/TMO as *p*-contact. The high bandgap of the TMO and its native *n*-type doping induces a strong band-bending at the interface with the absorber creating a barrier at the interface between the TMO layer and the intrinsic a-Si:H [11]. Such barrier blocks efficiently the electron inducing an inversion layer for the photogenerated holes which can

be extracted by tunneling mechanisms [12], i.e., the *band to band* (BTB) and the *trap assisted* (TA).

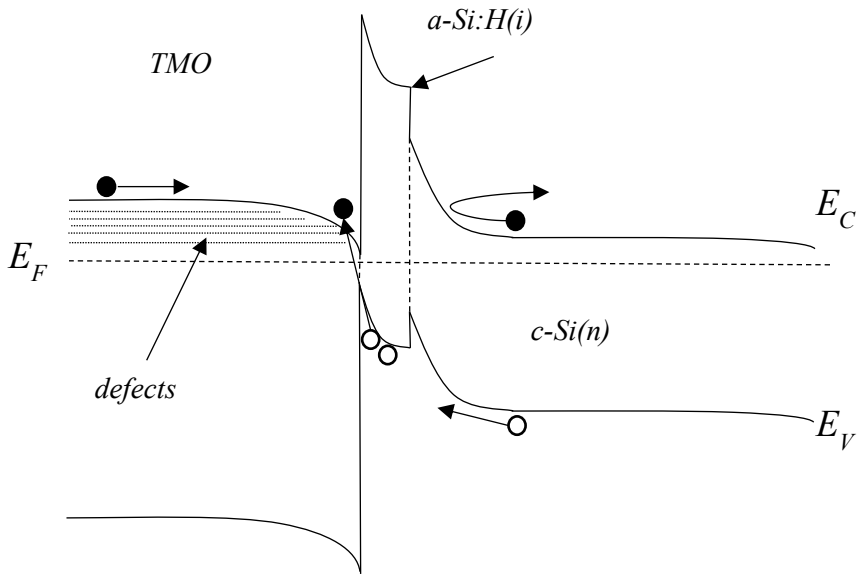

Figure 2.1 *Band diagram of a c-Si cell with a TMO-based p-contact*

2.1.1 Molybdenum trioxide

Molybdenum trioxide (MoO_3), in its sub-stoichiometric form MoO_x (x <3), is one of the most exploited transition metal oxides due to its high stability. Sub-stoichiometric films of MoO_3 present oxygen vacancies and an excess of metal atoms acting as *n*-type doping influencing most of the material's electrical and optical properties. In his crystalline phase, molybdenum oxide has an orthorhombic structure (α phase) or a monoclinic structure (β phase); both structures are essentially constituted by the octahedra of MoO_6 that share the angle [13]. The orthorhombic phase (α-MoO_3) has a layered structure, which consists of double layers of MoO_6 octahedra held together by covalent bonds in the (100) and (001) directions and by Van der Waals forces in the (010) direction. In recent years enormous efforts have been made to exploit the optical and electrical properties of MoO_x thin films in many different industrial applications such as photocatalysis, optoelectronic devices, photovoltaics, sensors, batteries. Moreover, several techniques are suitable to deposit this material, such as thermal evaporation, CVD, electrodeposition, spray pyrolysis, Pulsed Laser Deposition (PLD) [13] and DC magnetron sputtering [14]. Many scholars investigated the application of MoO_x in solar cells [2, 5, 15, 16]. A remarkable efficiency of 22.5% (with an FF of 80%), using a combination of aSi:H(i)/MoO_x/hydrogen-doped indium oxide/Cu, was achieved in 2015 [5], but the highest efficiency was achieved in 2020 with 23.5% [16].

The subsequent discussion is related to the results reported in [16] and a sketch of

the employed architecture is presented in Figure 2.2. The manufacturing process started from a 180 µm thick textured c-Si(*n*) wafer. A stack consisting of a-Si:H(i)/a-Si:H(n) was deposited on the backside by PECVD at 200 °C. A layer of a-Si:H(i) is then deposited on the front side. A pre-annealing in the air at 250 °C for 20 minutes, before the deposition of MoO_x, is performed to reduce the hydrogen content in the front layer of a-Si:H(i). After removing the surface oxide in an aqueous hydrofluoric acid solution diluted to 1%, the MoO_x layer is grown by thermal evaporation on the front side. The deposition of MoO_x is carried out in a vacuum chamber with pressure of 4×10^{-6} mbar and a deposition rate of 0.03 nm/s. Finally, 70 nm of Indium Tin oxide (ITO) was sputtered on the front side (70 nm). On the backside, 150 nm of ITO and 100 nm of Ag were deposited by sputtering. Finally, a metal grid was screen-printed on the front using a low-temperature silver paste, cured at 130 °C.

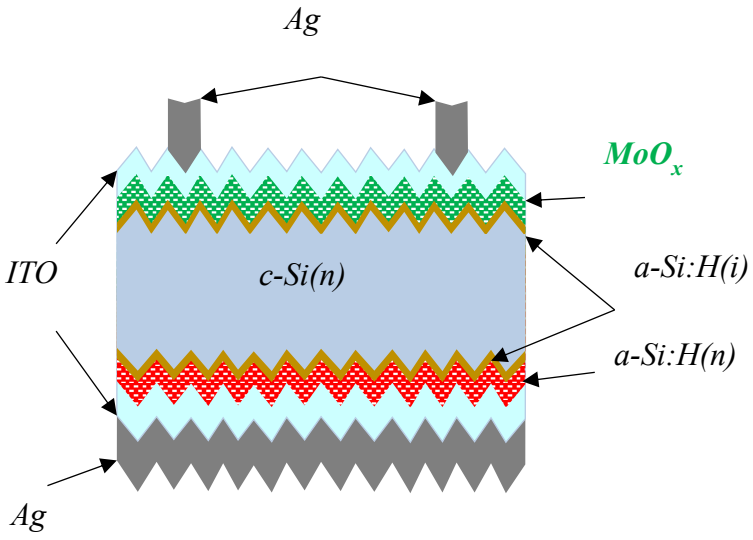

Figure 2.2 *HJT solar cells structures using MoO_x as hole-selective-contact.*

MoO_x presents a high work function (5.7 eV - 6.9 eV), guaranteeing hole selectivity; however, the passivation properties of this material are not considered sufficient; therefore, a thin film of a-Si:H(i) is usually applied between the molybdenum oxide and the c-Si. Nonetheless, MoO_x replaces the a-Si:H(p) film of a standard HJT solar cell on its illuminated side, reducing parasitic absorption at shorter wavelengths thanks to its high bandgap (about 3 eV). The presence of intrinsic a-Si:H on the front side causes some parasitic absorption below 500 nm, which partially contributes to the cell's short-circuit current density (J_{SC}); interestingly, the same consideration is not valid for the layer of doped a-Si:H.

An intense degradation, characterized by a drop in the *FF*, was observed after thermal treatment, such as annealing, above 130 °C. This degradation is due to the reduction of the CSC holes selectivity and can be attributed to several factors: formation of an interlayer

between MoO_x and TCO, formation of SiO_x at the MoO_x/a-Si:H interface, and reduction of MoO_x by H desorbing from adjacent layers decreasing its work function. Nonetheless, the MoO_x-based contact presents high transparency; thus, it is more advantageous than the standard a-Si:H(p) layer. A promising strategy, indeed, is to reduce further the thickness of MoO_x. However, as the MoO_x/a-Si:H(i) interface presents a higher recombination rate than the a-Si:H(p)/a-Si:H(i) interface, this may affect passivation requiring in compensation a thicker a-Si:H layer than the standard HJT.

The measured V_{OC} shows a significant gain with respect to a thicker a-Si:H(i) layer (10 nm). The best results were achieved with the thinnest MoO_x layer of 4 nm resulting in a V_{OC} 727 mV. Regarding the J_{SC}, both MoO_x and a-Si:H(i) resulted in a descending trend as their thickness increase. The best achievement J_{SC}, of about 40 mA/cm^2, occurred with the 6 nm thick amorphous silicon and 4 nm thick molybdenum oxide. For the fill factor, researchers' analysis showed that the thinnest MoO_x layer was sufficient to guarantee an adequate carrier selectivity resulting in *FF* up to 82%. Moreover, the analysis proved that the *FF* is independent of the a-Si:H(i) thickness while relies mostly on the MoO_x thickness. It should be remarked that for standard HJT cell with hole selective contact of a-Si:H(p), the thickness of a-Si:H(i) has a significant impact on the *FF*, suggesting that the MoO_x layer provides better selectivity than a-Si:H(p). Nevertheless, differently from the a-Si:H(p), the increase in the thickness of MoO_x decreases in the *FF*. The fill factor drop is linked to an increasing series resistance introduced by the thicker MoO_x film. The electrical characterization also reported the presence of a sub-optimal *J-V* characteristic (S-shape). The use of a thinner MoO_x layer mitigated this effect, although it was also reported for the cell with the thinnest MoO_x layer (4 nm). Nonetheless, cell performances have no significant impact as this architecture reported a higher efficiency than the reference HJT cell. The thinnest layers analyzed for MoO_x and a-Si:H(i) gave the best performance of the device, highlighting that such stacks simultaneously allow for high selectivity, passivation and good charge carrier transport. Instead, thicker layers lead to higher series resistances and optical losses. Finally, the performances of the champion cell reported in [16] are listed in Table 2.1.

Table 2.1 *Performances of the champion cell exploiting the MoO_x contact [16]*

J_{SC} (mA/cm^2)	V_{OC} (mV)	*FF* %	η %
39.15	727.5	82	23.5

2.1.2 Tungsten trioxide

Tungsten oxide (WO_3), in its sub-stoichiometric form WO_x (x <3), is also used as a hole selective contact in HJT solar cells; moreover, it is a non-toxic and inexpensive material [17]. Many researchers have studied this material as a possible alternative to the a-Si:H(p) of classical HJT cells [7, 11, 18], emphasizing the importance of the stoichiometric coefficient x to improve the performance of the cell [18]. However, it is not easy to fine-tune the stoichiometric coefficient of such oxides when deposited by the thermal evaporation method. Therefore, Pulsed Laser Deposition and DC magnetron sputtering can be exploited to deposit WO_x as hole selective contact in c-Si HJT solar cells [18, 19], allowing the tuning of the stoichiometry and optimizing the density of oxygen vacancies in the WO_x film. In this paragraph, a review of the results shown in [19] is reported.

The WO_x films were deposited by DC magnetron sputtering. The stoichiometry of the WO_x film was controlled through the O_2/Ar ratio present in the deposition chamber, varying it in the 0.15-0.3 range. The cell fabrication started from the deposition of a-Si:H(i) on both sides of an n-type c-Si wafer (200µm thick). The hole selective contact was made with 15 nm WO_x film deposited directly on one side by DC magnetron sputtering with a substrate temperature of 180 °C in O_2/Ar environment at a pressure of 2.67×10^{-3} mbar; for the *n* carrier selective contact, a doped hydrogenated micro-crystalline silicon film was deposited on the other side by PECVD. ITO 80 nm thick was deposited directly on the WO_x film by RF magnetron sputtering at a substrate temperature of 180 °C. Finally, the front contact grid and the full back contact were made both of silver paste. A representation of this architecture is sketched in Figure 2.3.

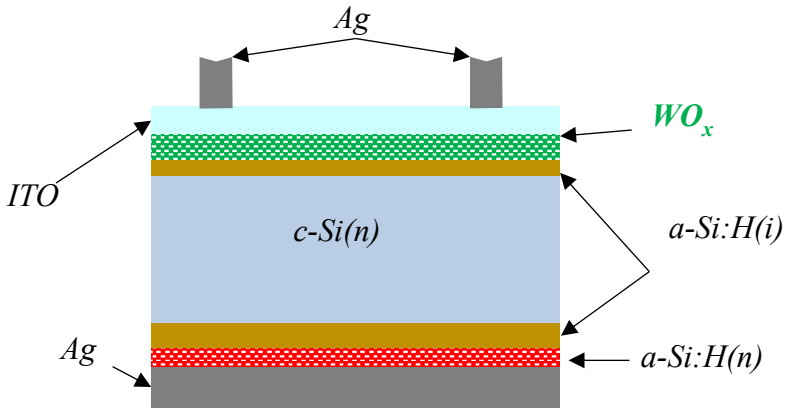

Figure 2.3 *Structure of a HJT with a WO_x hole selective contact*

The authors reported different behaviors of J_{SC} by varying the thickness and the stoichiometric coefficient of the WO_x film. In particular, x has a higher impact on the losses of J_{SC} than the thickness of the carrier selective contact layer. In general, a thickness of 15 nm of WO_x selective contact was sufficient to ensure good performance for the devices. The performances of the device (in terms of V_{OC}, J_{SC}, FF and η) as a function of x were analyzed, showing a rise both in V_{OC} and J_{SC} when x increases from 2.72 to 2.77; in particular, the rise of the open-circuit voltage is 3.3% (663 to 685 mV) and of the short-circuit current is 5.5% (34.7 to 36.6 mA/cm^2). The researchers explained that the J_{SC} rising trend is due to the transmissivity of the tungsten oxide sample, which increases linearly as the x approach the full stoichiometry (x≈3).

Nevertheless, the conductivity of the WO_x film decreases with an increasing x value. The maximum conductivity is reached for the lowest x, of about 2.72. This material has a lower conductivity than a-Si:H(p) by orders of magnitude. The efficiency η also decreases with increasing x; in particular, the best efficiency of 13.3% was reached with the minimum x equal to 2.72; differently, when the tungsten oxide is deposited with a stoichiometric coefficient of 2.77, the efficiency is lower than 6%. On the other hand, an improvement in V_{OC} is expected for higher x: when the stoichiometry is closer to that of WO_3, the concentration of oxygen vacancies is reduced, the work function increases leading to a more substantial band bending at the WO_x/c-Si interface with a consequent V_{OC} increase. Both the stoichiometric coefficient and the conductivity of the film need to be as high as possible to obtain simultaneously high V_{OC}, J_{SC} and FF. Moreover, the fill factor is predominant to obtain high efficiency, so it is unnecessary to choose a high x value [18].

The list of the performances of the champion cells of [19] is presented in Table 2.2.

Table 2.2 *Performances of the champion cell exploiting the WO_x contact [19]*

Stochiometric coefficient (x)	J_{SC} *(mA/cm^2)*	V_{OC} *(mV)*	*FF* *%*	η *%*
2.72	34.7	663	50%	13.3%
2.77	36.6	685	21%	below 6%

2.1.3 Vanadium pentoxide

Vanadium bound to oxygen to form a variety of compound with different structures such as VO (rock salt), VO_2 (rutile), V_2O_3 (corundum), V_2O_4 (rutile), V_6O_{13} (monoclinic), V_2O_5 (orthorhombic). Among these, vanadium pentoxide (V_2O_5) presents large bandgap and

work function (E_G=2.8eV, *WF*=6.7 eV [13]) and rised interest thanks to its chemical and thermal stability, besides for its various magnetic, optical and electrical properties. Indeed, vanadium pentoxide is a stable material suitable for a wide range of applications in optical electronics, photovoltaic, Li batteries, humidity sensors and electrochromic devices. Several deposition methods are used to prepare films of V_2O_5, i.e., vapor deposition techniques such as thermal evaporation, electron beam evaporation, RF magnetron sputtering, DC sputtering, PLD, CVD and PECVD [14]. A thin film of vanadium pentoxide can also be used as a hole selective contact for the HJT solar cell architecture. Such application has been studied by many researchers in recent years [20, 22, 23].

An interesting example is given in [23], where the absorber is a monocrystalline n-type silicon wafers with orientation (100). Such high-quality silicon allows for a high carrier lifetime, ensuring that most recombination paths are limited at surfaces. After standard cleaning and immersion in 1% HF, all substrates are loaded into a PECVD system to deposit the electron selective contact consisting of a stack of intrinsic and doped amorphous hydrogenated silicon carbide a-SiC_x:H(i\n) (x≈0.2). Two types of cells were obtained: one received random texturing of the front surface by alkaline etching (t-V_2O_5), while the other was polished on both surfaces (f-V_2O_5). For both cells, 20 nm thick films of V_2O_5 thermally evaporated made the hole selective contacts; the deposition pressure was 8×10^{-6} mbar, deposition rate of 0.2 Å/s and the substrate remained at room temperature during the process. The ARC on the front was made of sputtered ITO, the cell with texturing exploited a layer of a-SiC_x:H (x≈1) deposited by PECVD as the back reflector then laser-fired to obtain an array of locally-diffused point contacts of Ti/Al deposited by e-beam. The flat cell used ITO as a back reflector and the electrode was finalized with an evaporated silver contact. The front contact was equal for both cells and was made by thermally evaporated Ag with a grid pattern. A sketch of these architectures is presented in Figure 2.4.

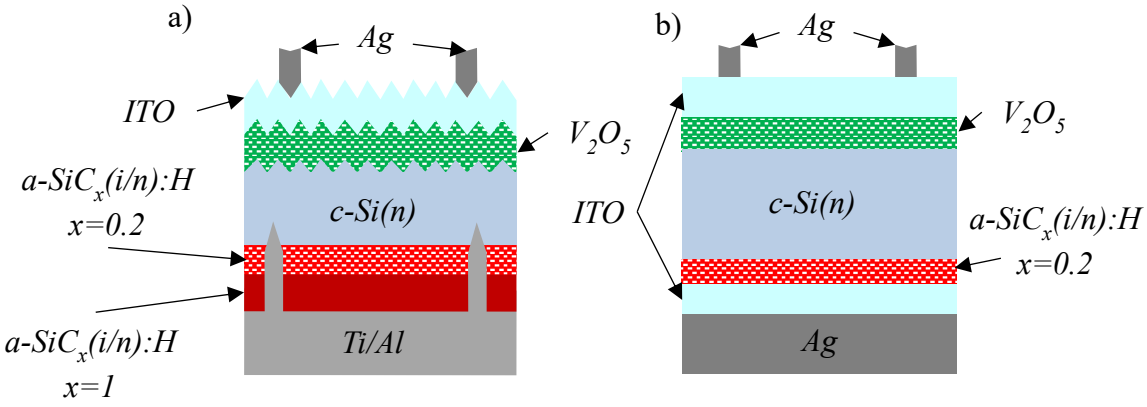

Figure 2.4 *Structure of HJT cell exploiting V_2O_5 as CSC: a) with pyramidal texturing, b) without texturing*

The dominant loss mechanism of these cells is the Shockley-Read-Hall (SRH), recombination process due to lattice defects and impurity atoms. These defects create available energy states within the energy gap at the V_2O_5/c-Si interface where electrons and holes can recombine. The use of V_2O_5 has shown excellent passivation properties allowing carrier lifetime of about 200 μs for the flat cells, which, remarkably, is about an order of magnitude higher than the textured architecture. The performance of V_2O_5-based cells is related to the reduction of surface recombination by improved passivation, resulting in higher open-circuit voltages. While textured devices using V_2O_5 exhibit higher short circuit currents thanks to its improved light management, the solar cell architectures with flat vanadium oxide granted higher open-circuit voltage due to its better passivation of the V_2O_5/c-Si.

Finally, the quality of these cells was evaluated through the performance parameters. The list of the performances of the champion cells of [23] is presented in

Table 2.3 *Performances of the champion cell exploiting the V_2O_5 contact [23]*

Texturing	J_{SC} (mA/cm^2)	V_{OC} (mV)	FF %	η %
Textured	34.5	605	74.7%	15.6%
Flat	32.5	662	70.6%	15.2%

2.1.4 Nickel oxide

Another candidate material in the TMO family is the substoichiometric nickel oxide (NiO), used as a dopant-free selective hole contact in HJT solar cells thanks to its remarkable optical and electrical properties. However, there have been no significant developments in the photovoltaic field for this promising material as hole selective contact, probably due to several issues in the pure NiO/Si(*n*) HJT solar cell, such as the carrier transport associated with Ni vacancies, defect states at the NiO/Si interface and low material conductivity. Nonetheless, several studies focus on improving the properties of the NiO film by introducing other metals compatible with the Ni^{2+}ion, i.e., Li [24, 25], Na [26] and K [27]. Besides, numerous studies have been conducted to analyze the changes in the optical and electrical properties of NiO when Cu is added. The exact incorporation mechanism of Cu is not well understood since Cu has different oxidation states (usually +1 and +2). The results here discussed are related to the result achieved by Yang et al. in 2018 [28] by introducing Cu in the NiO film.

The addition of Cu in the NiO film (NiO:Cu) improves the work function and conductivity of the film resulting in a greater built-in voltage and allowing for better hole transport in the HJT cells implemented with NiO:Cu/Si(*n*). Such carrier selective contact is made of a mixture of metallic Cu, Cu_2O and CuO. In particular, Cu_2O increases the concentration of holes and improves the work function and the acceptor-ions concentration; all these parameters are essential for achieving good performances in a solar cell. CuO, on the other hand, introduces defect states in the bandgap, which is undesirable as it increases the parasitic absorption as well as the recombination losses, deteriorating the quality of the interface.

The solar cell developed in [28] was made from a 180 μm crystalline silicon wafer (*n*-type with orientation (100)). The surface passivation was obtained by ultra-thin nitric acid oxidation of Si (NAOS) by immersing the wafer in a 68% aqueous HNO_3 solution. Two different architectures were then made: a reference one with a thin film of NiO, and the other one with NiO:Cu. Both depositions were carried out by RF magnetron sputtering with a substrate temperature of 300 °C, deposition pressure of 8×10^{-3} mbar and Ar flux of 50 sccm. The precursor used for both depositions was a ceramic target of NiO; in particular, for the NiO:Cu deposition, square chips of metallic Cu was bonded on top of the NiO target with Ag paste. After deposition, the samples were cooled in an O_2 atmosphere at 103 Pa to limit the oxygen vacancy content. The ITO anti-reflective layer was deposited by sputtering at room temperature. A thin film of magnesium (Mg) was introduced to improve the back surface field. A metal Ag grid was deposited by thermal evaporation on the front side and with a full deposition on the backside. Finally, all devices were annealed at 200 °C to improve the ITO layer conductivity and partially repair the damage caused by sputtering. The sketch of the solar cells here described is shown in Figure 2.5.

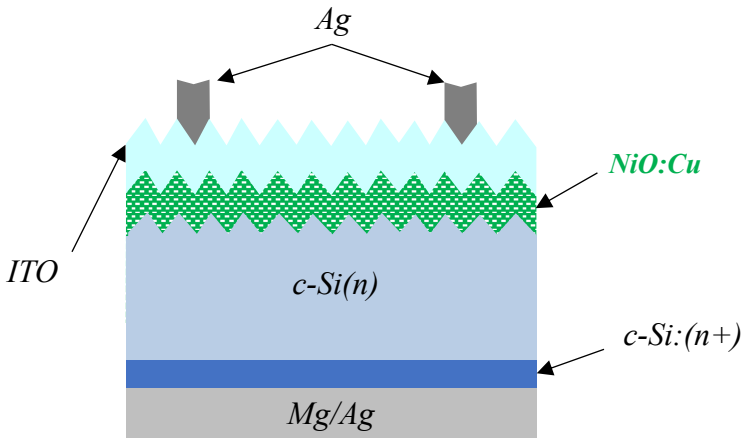

Figure 2.5 *Structure of a HJT solar cell with a NiO:Cu hole selective contact*

Devices with NiO hole selective contact presented V_{OC} of 260 mV, J_{SC} of 36.6 mA/cm^2, *FF* of 45.4% and η of 4.3%. Remarkably, these results represent a record for the NiO/Si HJT cells (without Cu). Regarding the hole selective contact made of NiO:Cu (27.1% Cu content), the efficiency of the device significantly increases to 9.1%, improving the open-circuit voltage (378 mV) and reaching 67.7% *FF.* With a higher Cu concentration in the CSC, an intense drop in the *FF* was observed (60.2%). The J_{SC} was negatively affected by the Cu presence in the CSC, reaching the value of 35.6 mA/cm^2. Such an effect was related to the increased absorption of the CSC introduced by the Cu content. Indeed, optical characterizations showed that as the Cu content increases, the absorption increases; moreover, when the Cu content reached 95.8%, the dominant component in the NiO:Cu was the copper oxide resulting in a HJT Cu_xO/Si solar cell with very low J_{SC} and *FF*.

The conductivity of NiO:Cu films has also been studied in function of the Cu concentration resulting in an increment at first and then a slight decrement with increasing Cu concentration. The conductivity increment mainly derives from the high concentration of electrons in the NiO:Cu film. Moreover, the conductivity increment improved the *FF*; on the other hand, the carriers mobility was negatively affected by the increasing Cu. The saturation current density of the devices was also analyzed from experimental characterization, highlighting a trend in the copper concentration: as the percentage of Cu rise from 17.1% to 27.1%, J_0 decreases; this behavior also explains the improvement of V_{OC}. By further increasing the concentration of Cu, J_0 drastically increases, causing a decrease in V_{OC}. Finally, the performances of the champion cell reported in [28] are listed in Table 2.4.

Table 2.4 *Performances of the champion cell exploiting the NiO:Cu (27.1% Cu content) contact [28]*

J_{SC} (mA/cm^2)	V_{OC} (mV)	*FF* %	η %
35.6	*378*	*67.7%*	*9.1%*

2.2 TMO as electron selective contact

Thin films of transition metal oxides are currently exploited as electron selective contacts; the working principle for such *n*-contact relies on the low work function of the exploited TMOs (i.e., TiO_2 ZnO TaO [29]), which allows the band alignment of the conduction band of the c-Si with the conduction band of the TMO. Depending on the *WF*, such alignment can be characterized by a small band offset tunneled by the electrons.

Figure 2.6 depicts the solar cell band diagram exploiting a-Si:H(i)/TMO as *n*-contact. The TMO large bandgap and its native *n*-type doping introduce a barrier that efficiently blocks the holes without limiting the electron transport.

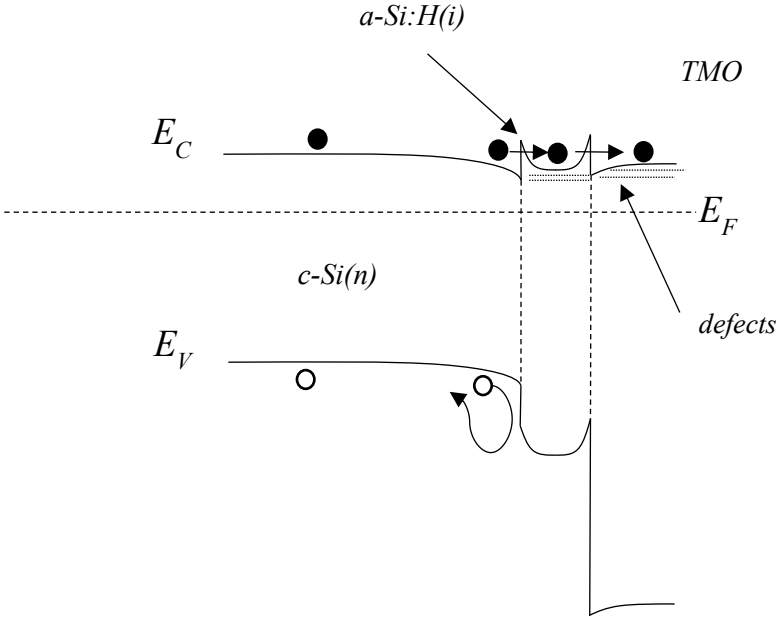

Figure 2.6 *band diagram of a c-Si cell with a TMO-based n-contact*

2.2.1 Titanium dioxide

Titanium dioxide in its sub-stoichiometric form (TiO_x) (x <2) represents a suitable choice for the electron selective contact. Indeed, such material presents a large offset in the valence band (E_V), which forms a barrier that blocks the hole transport; at the same time, it presents a good alignment of the conduction bands presenting a small offset (ΔE_C), allowing the electrons to pass through the selective contact. The formation of the sub-stoichiometric TiO_x compound is essential to achieve adequate selectivity and passivation. The presence of oxygen vacancies is necessary for achieving a low contact resistivity; in fact, the film conductivity rise as oxygen vacancies increment provides *n*-type doping.

TiO_x is one of the most employed TMOs as a selective *n* contact with several studies highlights the characteristics of such material and its implementation in HJT [8, 30-33]. Among these, in this section, the contribution given by Cho et al. [33] in 2018 will be discussed. In this contribution, an interesting comparison is made between the so-called "ATOM" contact (**a**-Si:H(i)/**T**iO_x/*low-w**o**rk-function-**m**etal*), standard a-Si:H(n) contact and a-Si:H(i)/Ca/Al contact stack. The ATOM contact is obtained by inserting a thin layer of TiO_x between a-Si:H(i) and Ca.

The solar cells discussed were made of a c-Si(*n*) wafer with a thickness of 165 μm.

The front side of the wafer has been textured, while the backside is chemically lapped. After cleaning in HF:HCl:O_3 and in HF:HCl, the a-Si:H(i/p) stack was deposited on the textured front side. Subsequently, after a quick cleaning in HF, the 8 nm a-Si:H(i) layer was deposited by PECVD on the backside. After immersion in HF, 2 nm of TiO_x were deposited by Atomic Layer Deposition (ALD) to obtain the so-called ATOM contact; the substrate temperature was set at 200 °C, the Ti precursor was titanium tetra-isopropoxide (TTIP) while H_2O was used for the oxidant precursor. The ITO layer was deposited by sputtering. The front metal grid was screen printed with Ag paste and subsequently cured at 175 °C. The back metallization was carried out with Ca and Al evaporation; these two depositions were subsequent without breaking the vacuum. A sketch of such architecture is presented in Figure 2.7.

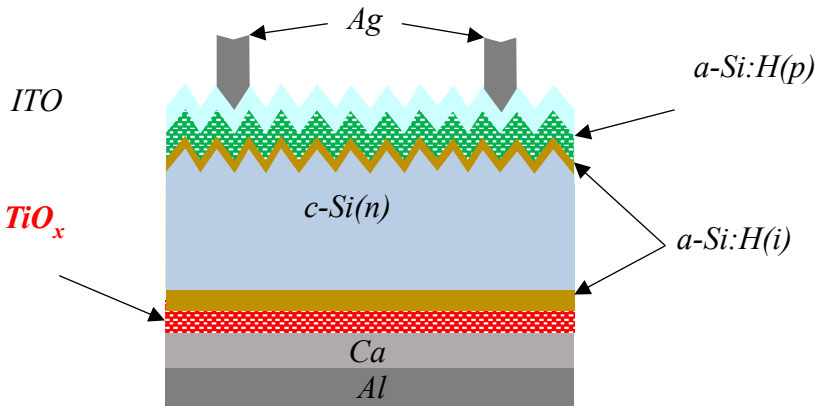

Figure 2.7 *Structure of an HJT solar cell with an ATOM contact*

Results reported in [34] highlighted that every solar cell presents relatively low J_{SC} values due to parasitic absorption in the ITO and in the a-Si:H(i/p) stack on the front side of the cells. The average J_{SC} is similar for all the solar cells, with the standard HJT cell presenting a slightly higher value. An average improvement was observed with the ATOM contact in V_{OC} (36 mV rise) and *FF* (2.3% rise) with respect to the solar cell exploiting the a-Si:H(i)/Ca/Al contact. Although the cell exploiting the TiO_x film shows a V_{OC} of 711 mV, all the performances of such cells are lower than the reference HJT standard cell.

Optical characterization has shown high parasitic absorption in the front stack at short wavelengths for the ATOM contact causing a lower J_{SC} than the a-Si:H(i)/Ca/Al contact. At longer wavelengths, there was no difference between the cell with the a-Si:H(i)/Ca/Al contact and the cell with the ATOM contact leading to the conclusion that the TiO_x contribution to absorption is negligible. Lower series resistance was observed for the ATOM cell, mainly due to two factors: (i) the height of the Schottky barrier at the CSC interface reduced by the introduction of TiO_x in combination with the low work function metal (Ca);

(ii) the growth of a SiO_x layer between TiO_x and a-Si:H(i) generating a dipole at the SiO_x/TiO_x interface, producing a downward band bending.

The performance of the back contacts was also studied through the *Suns-V_{OC}* characterization technique. Such characterization technique was proposed for the first time by Sinton and Cuevas [35], and involves the simultaneous measurements of the V_{OC} of the solar cell under test vs the corresponding incident light intensity. The cell with a-Si:H(i)/Ca/Al contact revealed a high resistivity value, mainly due to the Ca/Al back contact; interestingly, the ATOM contacts showed a lower resistivity leading to higher V_{OC} values than the reference cells.

The fill factor was also studied for the cells highlighting that the implementation of the ATOM contact results in cells with higher *FF* respect to the ones implementing the a-Si:H(i)/Ca/Al. However, the exploitation of the ATOM contact was not able to produce solar cells with performances comparable to the standard HJT cells. Indeed, ATOM contact presents higher R_S than the reference cells. The higher series resistance of the ATOM contact-based cells could be explained from the resistivity rise introduced by the absence of an a-Si:H(n) layer, alternatively by the relatively thin back metal layer.
Finally, the performances of the champion cell reported in [33] are listed in Table 2.5.

Table 2.5 *Performances of the champion cell exploiting the ATOM contact [33]*

J_{SC} (mA/cm^2)	V_{OC} (*mV*)	*FF* %	η %
35.1	711	72.9%	18.2%

2.2.2 Zinc Oxide

A less common metal oxide that can act as an n-type selective contact is the zinc oxide (ZnO). This material has a work function (4.45 eV), which allows the alignment with the c-Si conduction band in the HJT solar cells; moreover, it can be straightforwardly deposited by chemical solution deposition as well as by PLD [34] and sputtering [36]. The work function and conductivity of ZnO can be modified by introducing Li [37] or Al [38], allowing the tuning of the electronic properties of the ZnO and, therefore, obtaining a flexible material for the electron selective contact. Also, ZnO has an excellent passivation effect when deposited directly on the c-Si wafer. Moreover, the chemical solution deposition can lead to significant cost-reduction compared with vacuum deposition methods. Here, the

chemical solution deposition of Al-doped ZnO (AZO) will be discussed, which, compared to Li-doped ZnO, leads to higher efficiency.

According to Ding et al. [38], zinc oxide and AZO were spin-coated into n-type textured c-Si(*n*) wafer to replace a-Si:H(*n*) as a selective contact for electrons in heterojunction solar cells. The ZnO precursor was synthesized using zinc acetate dihydrate (ZnAc-2H_2O), ethanolamine (EA) and dimethoxyethanol (DME). Specifically, 1 g of ZnAc-2H_2O was dissolved in 20 ml of DME. Then 280 µl of EA was added into the solution. Subsequently, the mixture was stirred for 12 hours at room temperature. The AZO precursor synthesis was similar except that 10 mg of aluminum nitrate ($Al(NO_3)_3$-9 (H_2O)) mixed with 1 g of ZnAc-2H_2O were dissolved in 60 ml of DME. An oriented n-type crystalline silicon wafer (100) with a thickness of 220 µm was used to make the solar cells. An alkaline texturing was used to form the random pyramidal texture. Both sides of the wafer were passivated with 6 nm of a-Si:H(i) while 10 nm of a-Si:H(p) were deposited by PECVD on the front side as *p*-contact. The anti-reflective coating was made of 80 nm of sputtered ITO layer on top of the a-Si:H(p) layer. The front metal grid was deposited by silver thermally evaporated. The ZnO and ZnO:Al precursor was applied by spin-coating on the backside of the device (less than 6000 rpm). The devices were then annealed at 200 °C for 30 minutes to form the electron selective contact. Finally, a 400 nm Al electrode was thermally evaporated on the backside. The structure of the solar cells as described, is shown in Figure 2.8.

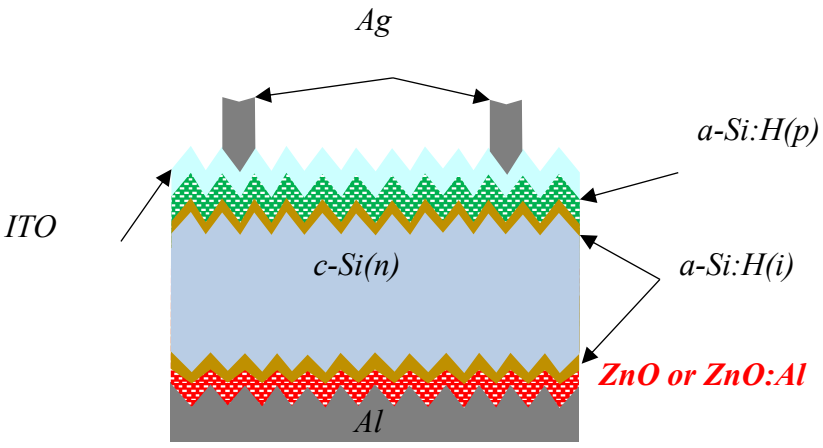

Figure 2.8 *Structure of a HJT with n selective contact with ZnO or Zn:O*

Although the spin-coating deposition ensured a good coverage on the textured silicon surface, the presence of a rough substrate caused an uneven layer thickness. The uniformity of the thickness is closely related to the precursor concentration; in particular, a precursor highly concentrated leads to a less uniform film. Besides, a thick layer of ZnO can affect

negatively the charge carrier collection. Nonetheless, less than 10 nm of ZnO with 50% surface coverage resulted in an adequate electron selective contact. The 6 nm thick a-Si:H(i) layer, deposited before the ZnO, ensured, in addition to an excellent passivation effect, an increase in V_{OC} compared to the case in which the ZnO is deposited directly on the c-Si. In particular the stack c-Si/a-Si:H(i)/ZnO/Al reached a V_{OC} of 629.1 mV. Doping with aluminum improves conductivity by about two orders of magnitude compared to undoped ZnO, resulting in lower series resistance and a higher *FF* and $V_{OC.}$ It is worth noting that the reduction of the precursor concentration improves the carrier collection, increasing the device's performance further.

Furthermore, the absorption coefficients of ZnO and ZnO:Al is much lower than doped hydrogenated amorphous silicon. Therefore, they are an exciting choice for bi-facial solar cells. Doping with aluminum, however, has the disadvantage of weakening the passivation effect of ZnO. Researchers affirmed that the ITO on the front side and all the metal contacts were not optimized and they claimed that through further optimization, efficiency greater than 20% can be reached ZnO selective contact in HJT solar cells.

The list of the performances of the champion cells of [38] is presented in Table 2.6.

Table 2.6 *Performances of the champion cell exploiting the ZnO contact [38]*

n-contact	J_{SC} *(mA/cm²)*	V_{OC} *(mV)*	*FF* *%*	η *%*
ZnO	37.19	629.1	63.31%	15.51%
ZnO:Al	38.23	672.1	71.95%	18.46%

2.3 Conclusions

The use of TMOs as carrier selective contact represents a viable alternative to the more common a-Si:H. Transition metal oxides with high work function such as molybdenum oxide, tungsten oxide, and vanadium allow for a good alignment of the TMO's valence band with the conduction band of the c-Si allowing for an efficient collection of the photogenerated holes while blocking the electrons. Instead, for the electron selective contact, a lower work function material, such as titanium oxide and zinc oxide, makes a good alignment between the TMO and absorber conduction bands, allowing the electron transport while blocking the holes. It is worth noting that for both types of CSC, extensive knowledge of the materials optical and electrical properties is fundamental in the optimization process

of such contacts.

Moreover, the information regarding the defect density of states (DOS) at the TMO interface was highlighted by several scholars to be essential for understanding the tunnelling mechanisms, improving the conductivity of the material and address the parasitic absorption [1, 4, 6, 7, 19, 23-27]. Different simulation studies are reported to optimize CSC employed in HJT solar cells [39, 40] but the limitation given by the lack of data on DOS has been exceeded simulating the solar cells with different defect-DOS distributions. On the one hand, this approach allows the optimization of the carrier selective contact; on the other hand, the results of such analysis may not be reproduced in an actual solar cell. Therefore, the characterization of the transition metal oxides defect density of states is important to answer for the researchers' request for reliable and accurate information that can be used for their simulations and subsequent optimization of the doping-free solar cells. Such characterizations will be discussed in the following chapters of this thesis.

References

[1] C. Yu, S. Xu, J. Yao, S. Han, "Recent Advances in and New Perspectives on Crystalline Silicon Solar Cells with Carrier-Selective Passivation Contacts", *Crystals*, vol. 8, no. 11, 2018, doi: https://doi.org/10.3390/cryst8110430.

[2] Battaglia *et al*., "Hole selective MoOx contact for silicon solar cells", *Nano Lett*., vol. 14, no. 2, pp. 967–971, Feb. 2014, doi: https://doi.org/10.1021/nl404389u.

[3] J. Shi *et al*., "MoOx modified ITO/a-Si:H(p) contact for silicon heterojunction solar cell application", *Mater. Res. Bull.*, vol. 97, pp. 176–181, 2018, doi: https://doi.org/10.1016/j.materresbull.2017.09.005.

[4] M. Bivour, J. Temmler, H. Steinkemper, and M. Hermle, "Molybdenum and tungsten oxide: High work function wide band gap contact materials for hole selective contacts of silicon solar cells", *Sol. Energy Mater. Sol. Cells*, vol. 142, pp. 34–41, 2015, doi: https://doi.org/10.1016/j.solmat.2015.05.031.

[5] J. Geissbühler *et al*., "22.5% Efficient Silicon Heterojunction Solar Cell With Molybdenum Oxide Hole Collector", *Appl. Phys. Lett*., vol. 107, no. 8, 2015, doi: https://doi.org/10.1063/1.4928747.

[6] K. Mallem *et al*., "Molybdenum oxide: A superior hole extraction layer for replacing p-type hydrogenated amorphous silicon with high efficiency heterojunction Si solar cells", *Mater. Res. Bull*., vol. 110, pp. 90–96, Feb. 2019, doi: https://doi.org/10.1016/j.materresbull.2018.10.018.

[7] M. Mews, A. Lemaire, and L. Korte, "Sputtered Tungsten Oxide as Hole Contact for Silicon Heterojunction Solar Cells", *IEEE J. Photovoltaics*, vol. 7, no. 5, pp. 1209–1215, 2017, doi: https://doi.org/10.1109/JPHOTOV.2017.2714193.

[8] X. Yang, Q. Bi, H. Ali, K. Davis, W. V. Schoenfeld, and K. Weber, "High-Performance TiO2-Based Electron-Selective Contacts for Crystalline Silicon Solar Cells", *Adv. Mater.*, pp. 5891–5897, 2016, doi: https://doi.org/10.1002/adma.201600926.

[9] R. García-Hernansanz *et al.,* "Transport mechanisms in silicon heterojunction solar cells with molybdenum oxide as a hole transport layer", *Sol. Energy Mater. Sol. Cells*, vol. 185, no. January, pp. 61–65, 2018, doi: https://doi.org/10.1016/j.solmat.2018.05.019.

[10] H. Wu *et al*., “Improving CNT-Si solar cells by metal chloride-to-oxide transformation”, *Nano Res*., vol. 13, no. 2, pp. 543–550, 2020 doi: https://doi.org/10.1007/s12274-020-2648-5.

[11] L. G. Gerling, C. Voz, R. Alcubilla, and J. Puigdollers, “Origin of passivation in hole-selective transition metal oxides for crystalline silicon heterojunction solar cells*”, J. Mater. Res*., vol. 32, no. 2, pp. 260-268, 2017, doi: https://doi.org/10.1557/jmr.2016.453.

[12] P. Procel, P. Löper, F. Crupi, C. Ballif, and A. Ingenito, “Numerical simulations of hole carrier selective contacts in p-type c-Si solar cells”, *Sol. Energy Mater. Sol. Cells*, vol. 200, Sep. 2019, doi: https://doi.org/10.1016/j.solmat.2019.109937.

[13] D. Scirè *et al*., "Analysis of Transition Metal Oxides based Heterojunction Solar Cells with S-shaped J-V curves," *2020 AEIT International Annual Conference (AEIT)*, Catania, Italy, 2020, pp. 1-6, doi: https://doi.org/10.23919/AEIT50178.2020.9241142.

[14] S. A. Elkot, W. Mohamed, M. Elrouby, H. M. Ali: “Structure, Optical, Corrosion, and Photocatalytic Properties of Thermally Evaporated Molybdenum Trioxide Thin Films Deposited on Different Substrates”, *International Journal of New Horizons in Physics*, vol. 7, no. 1, pp. 7-17, 2019.

[15] H. Mehmood, T. Tauqeer, H. Nasser, S. Hussain, R. Turan, “Effect of Hole-Selective Molybdenum Oxide Work Function and Silicon Wafer Resistivity on Dopant-Free Asymmetric Silicon Heterostructure Solar Cell”, *2017 International Renewable and Sustainable Energy Conference (IRSEC)*, pp. 1-5, Tangier, 2017, doi: https://doi.org/10.1109/IRSEC.2017.8477335.

[16] J. Dréon , Q. Jeangros, J. Cattin, J. Haschke, L. Antognini, C. Ballif, M. Boccard: “23.5%-efficient silicon heterojunction silicon solar cell using molybdenum oxide as hole-selective contact”, *Nano Energy*, vol. 70, pp. 1-7, Apr. 2020, doi: https://doi.org/10.1016/j.nanoen.2020.104495.

[17] H. Chen, D. Jan, C. Chen, K. Huang, Y. Luo, J. Chen: “Investigation of optical and structural properties of WO3 thin films with different sputtering depositions”, *Proceedings of SPIE*, vol. 8486, Oct. 2012, doi: https://doi.org/10.1117/12.897017.

[18] T. A. Tran *et al*., “Effects of oxidation state on photovoltaic properties of reactively magnetron sputtered hole-selective WOx contacts in silicon heterojunction solar

cells", *Semiconductor Science and Technology*, vol. 35, no. 4, 2020, doi: https://doi.org/10.1088/1361-6641/ab74ec.

[19] Y.S.Zou *et al.*, "Structural and optical properties of WO3 films deposited by pulsed laser deposition", *Journal of Alloys and Compounds* , vol. 583, pp. 465-470, Jan. 2014, doi: https://doi.org/10.1016/j.jallcom.2013.08.166.

[20] L. G. Gerling, G. Masmitja, C. Voz, P. Ortega, J. Puigdollers, R. Alcubilla, "Back junction n-type silicon heterojunction solar cells with V2O5 hole selective contact", *Energy Procedia,* vol. 92, pp. 633–637, 2016, doi: https://doi.org/10.1016/j.egypro.2016.07.029.

[21] K.V. Madhuri, M. Bujji Babu: "Structural and spectroscopic characterisation of V2O5 thin films", *Materials Today: Proceedings*, vol. 19, no. 6, pp. 2693–2696, 2019, doi: https://doi.org/10.1016/j.matpr.2019.10.141.

[22] S. Sanyal, *et al*., "Hole Selective Contacts: A Brief Overview", *Current Photovoltaic Research*, vol. 7, no. 1, pp. 9-14, 2019, doi: https://doi.org/10.21218/CPR.2019.7.1.009.

[23] O. Almora, L. G. Gerling, C. Voz, R. Alcubillab, J. Puigdollersb, G. Garcia-Belmontea, "Superior performance of V2O5 as hole selective contact over other transition metal oxides in silicon heterojunction solar cells", *Solar Energy Materials and Solar Cells*, vol 168, pp. 221–226, 2017, doi: https://doi.org/10.1016/j.solmat.2017.04.042.

[24] F. H. Hsu, N. F. Wang, Y. Z. Tsai, Y. S. Cheng and M. P. Houng, "A new p-Ni1-xO:Li/n-Si heterojunction solar cell fabricated by RF magnetron sputtering", *J. Phys. D: Appl. Phys*., vol. 46, no. 27, Jun. 2013, doi: https://doi.org/10.1088/0022-3727/46/27/275104.

[25] T. Dutta, P. Gupta, A. Gupta, and J. Narayan, "Effect of Li doping in NiO thin films on its transparent and conducting properties and its application in heteroepitaxial p-n junctions", *Journal Of Applied Physics*, vol. 108, no. 8, 2010, doi: https://doi.org/10.1063/1.3499276.

[26] Y. R. Denny, K. Lee, C. Park, S. K. Oh, H. J. Kang, D. Yang, S. Seo, "Electronic, electrical and optical properties of undoped and nadoped NiO thin films", *Thin Solid Films*, vol. 591, part B, pp. 255–260, 2015, doi: https://doi.org/10.1016/j.tsf.2015.04.043.

[27] N. Wang, C. Q. Liu, C. Q. L. B. Wen, H.L. Wang, S.M. Liu, W.W. Jiang, W. Y. Ding, W. P. Chai, "Structural, electrical and optical properties of K-doped NiO films prepared by rapid pyrolysis sol-gel technique", *Thin Solid Films*, vol. 616, pp. 587-593, Oct. 2016, doi: https://doi.org/10.1016/j.tsf.2016.08.051.

[28] X. Yang, J. Guo, Y. Zhang, W. L., Y. Sun: "Hole-selective NiO:Cu contact for NiO/Si heterojunction solar cells"; *Journal of Alloys and Compounds*, vol. 747, pp. 563-570, May 2018, doi: https://doi.org/10.1016/j.jallcom.2018.03.067.

[29] Y. Xinbo *et al*.,"Tantalum Nitride Electron-Selective Contact for Crystalline Silicon Solar Cells", *Advanced Energy Materials*, vol.8, no. 20, Jul. 2018, doi: https://doi.org/10.1002/aenm.201800608.

[30] K. A. Nagamatsu *et al.*, "Titanium dioxide/silicon hole-blocking selective contact to enable double-heterojunction crystalline silicon-based solar cell", *Applied Physics Letters,* vol. 106, no. 12, Mar. 2015, doi: https://doi.org/10.1063/1.4916540.

[31] X. Yang, K. Weber, "N-type silicon solar cells featuring an electron-selective TiO2 contact", *2015 IEEE 42nd Photovoltaic Specialist Conference (PVSC)*, New Orleans, LA, 2015, doi: https://doi.org/10.1109/PVSC.2015.7356139.

[32] J. Cho *et al*., "Evidence of TiOx reduction at the SiOx/TiOx interface of passivating electron- selective contacts", *AIP Conference Proceedings* vol. 1999, no.1, 2018, doi: https://doi.org/10.1063/1.5049268.

[33] J. Cho *et al*., "Passivating electron-selective contacts for silicon solar cells based on an a-Si:H/TiOx stack and a low work function metal", *Prog. Photovolt. Res. Appl*., vol. 26, no. 10, pp. 835–845, Oct. 2018, doi: https://doi.org/10.1002/pip.3023.

[34] H. Agura, A. Suzuki, T. Matsushita, T. Aoki, M. Okuda, "Low resistivity transparent conducting Al-doped ZnO films prepared by pulsed laser deposition", *Thin Solid Films*, vol. 445, no. 2, pp. 263–267, Dec. 2003, doi: https://doi.org/10.1016/S0040-6090(03)01158-1.

[35] R. Sinton, A. Cuevas, "A quasi-steady-state open-circuit voltage method for solar cell characterization", in *Proc. of 16th European Photovoltaic Solar Energy Conf.,* Glasgow, Scotland; 2000, pp. 1152-1155. [Online]. Available: https://www.sintoninstruments.com/wp-content/uploads/sinton-epvsc16-pcd.pdf [Accessed: 11-Apr-2021]

[36] Y. Zhang et al., "Crystal growth of undoped ZnO films on Si substrates under

different sputtering conditions", *Journal of Crystal Growth*, vol. 243, no. 3-4, pp. 439-443, Sept. 2002, doi: https://doi.org/10.1016/S0022-0248(02)01569-5.

[37] Z. Wang et al., "Modulation-doped ZnO as high performance electron-selective layer for efficient silicon heterojunction solar cells", *Nano Energy*, vol. 54, pp. 99-105, Dec. 2018, https://doi.org/10.1016/j.nanoen.2018.10.010.

[38] J. Ding, Y. Zhou, G. Dong, M. Liu, D. Yu, F. Liu, "Solution-processed ZnO as the efficient passivation and electron selective layer of silicon solar cells", *Progress in Photovoltaics*, vol.26, no 12, pp. 974-980, Dec. 2018, doi: https://doi.org/10.1002/pip.3044.

[39] C. Messmer, M. Bivour, J. Schon, S. W. Glunz, and M. Hermle, "Numerical Simulation of Silicon Heterojunction Solar Cells Featuring Metal Oxides as Carrier-Selective Contacts", *IEEE J. Photovoltaics*, vol. 8, no. 2, pp. 456–464, 2018, doi: https://doi.org/10.1109/JPHOTOV.2018.2793762.

[40] R. A. Vijayan *et al.*, "Hole-Collection Mechanism in Passivating Metal-Oxide Contacts on Si Solar Cells: Insights from Numerical Simulations", *IEEE J. Photovoltaics*, vol. 8, no. 2, pp. 473–482, 2018,doi: https://doi.org/10.1109/JPHOTOV.2018.2796131.

3 Experimental Details

In this section, the main characterization techniques and equipment employed for the deposition and the characterization of the transition metal oxides are listed and briefly discussed.

The TMOs films were deposited through Physical Vapor Deposition (PVD) methods, whereas the other layers of the solar cell stacks exploited the Chemical Vapor Deposition (CVD) techniques. PVD involves generating a vapor stream and its subsequent condensation in a thin film in a vacuum chamber. The term PVD encompasses several techniques including thermal evaporation, sputtering and Pulsed Laser Deposition (PLD), which will be analyzed afterwards. The main difference between the various PVD techniques lies in how the vapor flow is generated from the material precursor (target). Moreover, deposition can be carried out in vacuum or atmosphere of one or more gases altering the chemical composition of the deposited film.

3.1 TMO fabrication methods

3.1.1 Thermal evaporation

Atoms and molecules are removed during the deposition in a vapor stream from a precursor target in a crucible; such vapor stream then condenses forming a film on the substrate placed in front of the target. Generally, the target material is heated to an appropriate temperature, depending on the material and the deposition pressure. The deposition system involves using a vacuum chamber with a pressure generally lower than 1.33×10^{-4} mbar allowing a long free mean path for the evaporated material. This technique is commonly used for materials with a melting temperature lower than 1500 °C [1]. The precursor melting can be achieved by heating, through Joule's effect, the crucible, typically made of carbon, molybdenum, tantalum or tungsten. Furthermore, the crucibles are made in different shapes, including baskets, ships and wires.

Thermal evaporation is a straightforward technique that allows a high deposition rate and can be achieved with relatively low-cost equipment. However, thermal evaporation is not suitable for film manufacturing from different materials, such as alloys, due to different melting points and vapor pressures of the precursor elements [2]. Figure 3.1 schematically shows the thermal evaporation process while the employed system is a PROVAC PRO500S

metal evaporator located at Delft University of Technology (see Figure 3.2). This technique was used for the deposition of the samples of molybdenum oxide investigated in this PhD project and discussed on Chapter 4.

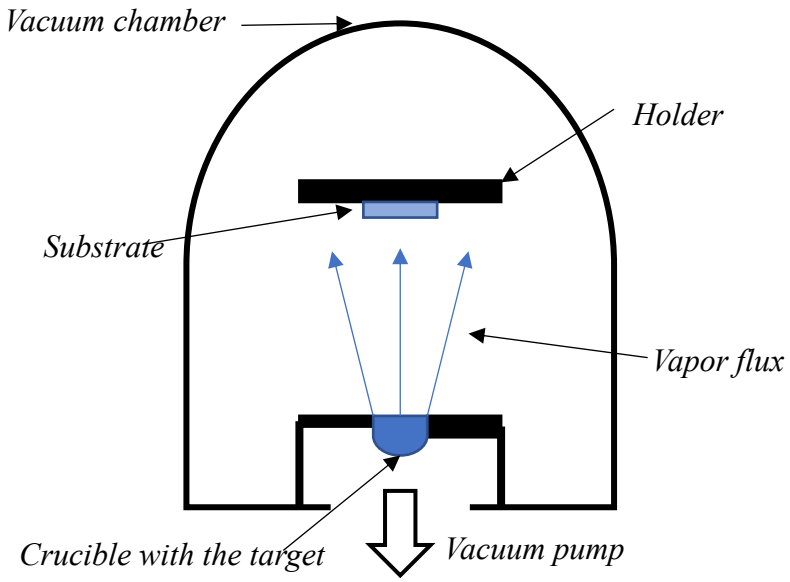

Figure 3.1 *Thermal evaporation deposition process*

Figure 3.2 *The PROVAC PRO 500S metal evaporator at the Delft University of Technology*

3.1.2 Pulsed laser deposition

The Pulsed Laser Deposition (PLD) is a physical vapor deposition technique where a power laser is used to irradiate the target surface of creating a vapor stream condensed on a substrate. PVD is a reliable and easily implemented deposition method that maintains the stoichiometry of the precursor material on the deposited films [3]. Furthermore, this method is suitable for depositing different materials such as superconductors, oxides, nitrides, carbides, semiconductors, metals and polymer with high deposition rates [4], besides it is also capable of synthesizing nanopowders and nanorods [5].

The deposition process is conducted in a vacuum chamber; Nd:YAG and excimer laser are usually employed [3]. Furthermore, a focused laser beam allows for a small target area (with a surface even lower than 1 cm^2) [4]. The substrate is faced in front of the target at a distance of 2-10 cm. Each laser pulse vaporizes a small amount of the target, creating a plasma, the so-called *plume*. The vaporized material is expelled perpendicularly to the target surface. One of the main drawbacks of PLD is the uneven uniformity of the deposited films due to the highly unidirectional nature of the *plume*. Nonetheless, this problem is usually overcome by putting in rotation the substrate and adopting a raster scan of the target.

The quality and the deposition rate depend on many parameters: laser wavelength, laser pulse duration, pulse frequency, laser energy density, substrate target distance, substrate temperature, gas in the chamber and pressure of that gas. During the deposition, it is possible to work under a vacuum or in the presence of a reactive gas. By changing the deposition conditions, the thickness, stoichiometry and density of the deposited material can be controlled. Furthermore, it is possible to vary the substrate temperature, thus enabling the growth of amorphous and crystalline films [6]. Another highly influential deposition parameter is the partial pressure of oxygen (PO_2). For example, during the growth of oxides, oxygen is required to achieve the desired stoichiometric transfer between target and substrate. Otherwise, the film will be sub-stoichiometric due to oxygen vacancies. This feature can be exploited to control the stoichiometry of the deposited films used as carriers selective contacts in solar cells [7]. Figure 3.3 presents a simplified PLD system, while Figure 3.4 presents the PLD setup of the *Thin Film Laboratory* at the University of Palermo, where the samples of titanium oxide, investigated in this PhD project, and discussed on Chapter 5, have been synthetized. Likewise, the PLD system was used for the deposition of the samples of molybdenum and tungsten oxide discussed in Chapter 6.

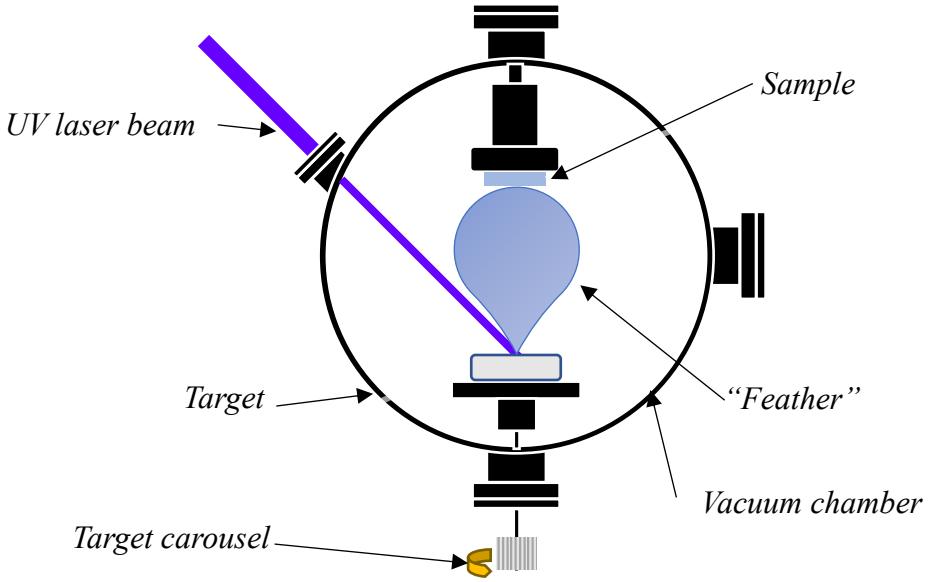

Figure 3.3 *Pulsed Laser Deposition system*

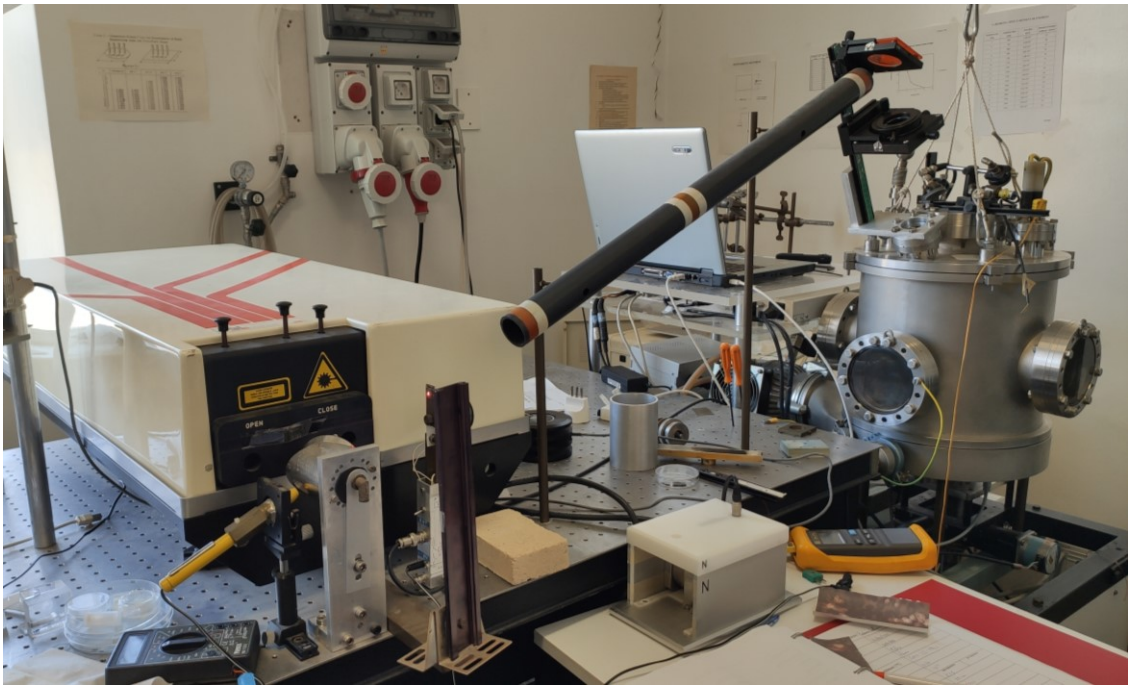

Figure 3.4 *Pulsed laser deposition setup at the Thin Film Laboratory (University of Palermo)*

3.1.3 RF plasma enhanced chemical vapor deposition

Radio Frequency Plasma Enhanced Chemical Vapor Deposition (RF-PECVD) is a deposition method where plasma is generated from an RF source [8]. The substrate is placed between two perpendicular electrodes and a radio frequency discharge between them is used to ionize precursor gases into a plasma between the electrodes. A bias voltage applied at the

electrodes accelerates the ionized atoms (or molecules) towards the substrate, where they condensate in a thin film [8]. The RF-PECVD setup is usually composed by a multi-chamber system consisting of a central transport chamber equipped with a robot arm and several deposition process chambers connected to the transport chamber. In the process chambers intrinsic and doped amorphous silicon and silicon alloys can be deposited. Such system can be programmed to deposit automatically complex multilayer structures, i.e., solar cells. Cross-contamination between the different processes is prevented by using dedicated processing chambers for each deposition. Figure 3.5 presents the RF-PECVD setup employed at the Delft University of Technology, where the solar cells investigated in this PhD project, and discussed on Chapter 6, have been synthetized.

Figure 3.5 *Radio frequency plasma enhanced chemical vapor deposition setup at Delft University of Technology*

3.2 TMO characterization techniques

3.2.1 X-ray photoelectron spectroscopy

The X-ray Photoelectron Spectroscopy (XPS) is a characterization technique that allows the analysis of the sample's surface composition; furthermore, it can provide information regarding the oxidation states of the elements forming the sample. The XPS analysis is based on the photoelectric effect: a X-ray beam provides the energy to the sample, such energy is absorbed by the atoms in surface and transferred to an electron which is

subsequently expelled from the atom (photoemission) and, therefore, detected. The measurement process occurs in a high vacuum environment, at a pressure of about 10^{-8} mbar. The kinetic energy (KE) of the photo emitted electrons is measured, giving information on the element from which they are originated. The KE of the expelled electrons depends on the energy of the incident radiation ($h\nu$) and on the binding energy (BE), that is, the energy needed to extract the electron from the atom. The BE is indicative of the chemical element involved in the photoemission and can be extrapolated from the kinetic energy as expressed in (3.1) where Φ is the extraction work of the spectrometer detector:

$$BE = h\nu - KE - \Phi \tag{3.1}$$

The obtained spectrum leads to a qualitative and quantitative chemical analysis of the atoms present on the surface. The assignment of a peak of the spectrum to an atomic species occurs by correlating the measured BE with the information present in the literature [9]. Furthermore, a curve fitting procedure of the XPS spectrum can be used to identify the oxidation state of the element present on the surface.

The XPS measurements presented in this thesis were carried out at the Department of Chemistry of the University of Catania and the Institute for the Study of Nanostructured Materials (ISMN) of the National Research Council in Palermo. Figure 3.6 presents the XPS analysis setup at the ISMN and is composed of the VG Microtech ESCA 3000 Multilab spectrometer.

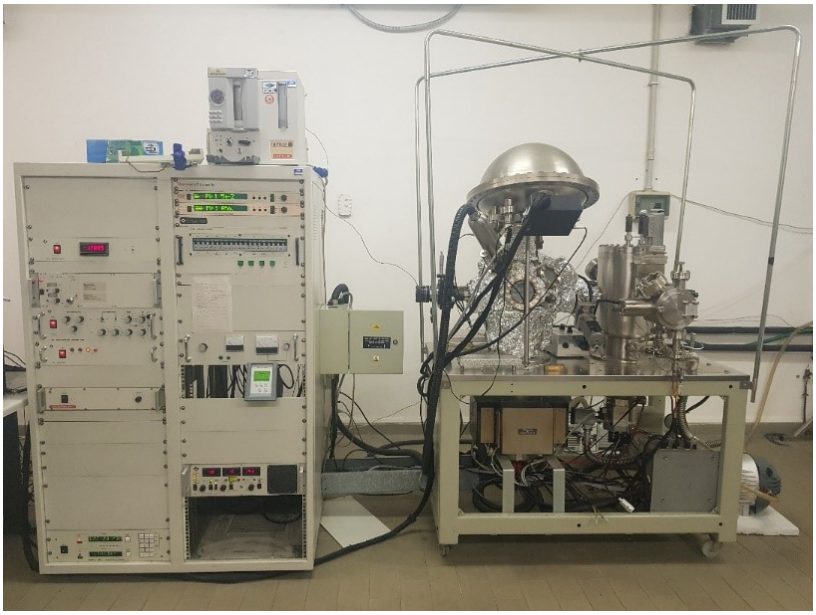

Figure 3.6 *X-ray photoelectron spectroscopy setup at the Institute for the Study of Nanostructured Materials (National Research Council)*

3.2.2 Spectroscopic ellipsometry

Spectroscopic Ellipsometry (SE) is an optical characterization technique based on the shift in light's polarization after interaction with the sample under test. A Xenon lamp combined with a polarizer is generally used as a light source to irradiate the sample. A fraction of the light irradiating the sample is reflected and finally detected by wavelength in amplitude and phase. SE is a fast and reliable non-destructive characterization technique which provides information about the film's properties such as thickness, optical band gap and complex refractive index [10]. However, these properties are extrapolated from the experimental data through a fitting procedure requiring an accurate optical model e.g., Tauc-Lorentz, Cody-Lorentz, Tauc. The spectroscopic ellipsometry measurements setup used for the measurement presented in this thesis is an M-2000F J.A. Woollam Co Spectroscopic Ellipsometer [11] located at the Delft University of Technology.

3.2.3 Raman spectroscopy

The Raman spectroscopy technique is used to observe low-frequency modes in thin films, using the inelastic scattering of monochromatic light. Due to the illumination with monochromatic light, the incident photons interact with the atoms and molecules in the lattice, resulting in scattering of the incident photons. The scattering process is dominated by the Rayleigh scattering, which is an elastic form of scattering, i.e., the photon energy is conserved while its direction is changed. A rarer process is the inelastic scattering, the so-called Raman scattering, resulting in a reduction (Stokes) or increase (anti-Stokes) of the scattered photon energy [12]; measuring the spectrally dependent Raman scattering intensity results in a spectrum, indicating the atomic lattice acoustic and optical modes. Raman spectroscopy is suitable for analyzing various materials such as raw minerals, organic, polymer and semiconductors. The interpretation of Raman spectra and the comparison with results in the literature allow for identifying the material under test highlighting, furthermore, the presence of a crystalline phase [13]. Raman spectra were measured using a Renishaw InVia setup located at the Delft University of Technology (see Figure 3.7), with a 25 mW Ar laser as excitation source with a wavelength of 514 nm and focused on a spot of approximately 1 μm.

Figure 3.7 *Raman spectroscopy setup at Delft University of Technology*

3.2.4 Photothermal deflection spectroscopy

Photothermal Deflection Spectroscopy (PDS) is a non-destructive optical absorption measurement technique based on excited carriers thermal relaxation. A xenon lamp is used as the light source, and its light is passed through a monochromator and a chopper before illuminating a sample submerged in non-toxic liquid perfluorohexane fluorinert FC-72. At the same time, a laser beam is aligned to be tangent to the film surface. Due to absorption of the chopped monochromatic light, electrons are excited and subsequently thermalize, heating the liquid in which the sample is immersed. The liquid refractive index is thermal-dependent therefore, the heating of the FC-72 produces a deflection in the laser beam measured by two photodiodes. The laser deflection determines the absorption coefficient of the film with a dynamic detection range in the optical absorptance up to 4 orders of magnitude [14, 15] and measures transmittance (T), reflectance (R) and absorptance (A) spectra on the same spot of the sample simultaneously, allowing for the correction of interference fringes [16]. The T, R and A spectra are calibrated with a cuvette with FC-72, a sapphire sample, and carbon nanotubes, respectively. The PDS setup employed is shown in Figure 3.8.

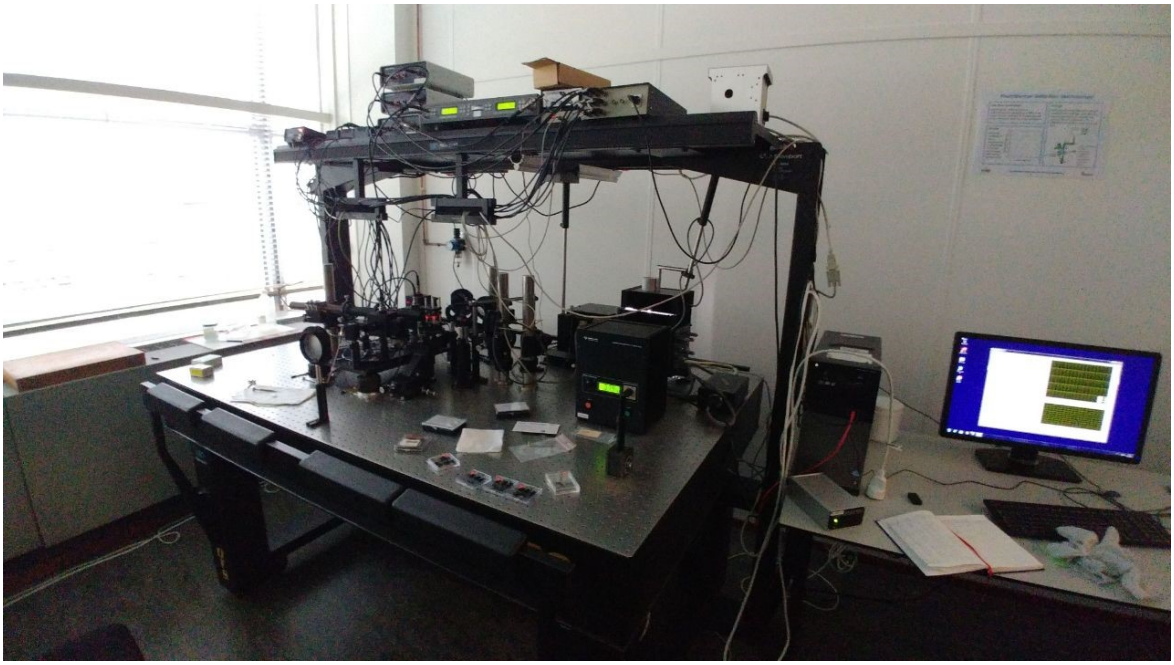

Figure 3.8 *Photothermal deflection spectroscopy setup at Delft University of Technology*

References

[1] D. M. Mattox, "Vacuum Evaporation and Vacuum Deposition" in Handbook of *Physical Vapor Deposition (PVD) Processing*, pp. 288-342 1998, doi: https://doi.org/10.1016/B978-081551422-0.50006-1.

[2] R. J. Martín-Palma, A. Lakhtakia: "Vapor-Deposition Techniques" in *Engineered Biomimicry,* pp. 383-398, 2013, doi: https://doi.org/10.1016/B978-0-12-415995-2.00015-5.

[3] R. Eason: "Pulsed Laser Deposition of Complex Materials: Progress Towards Applications" in *Pulsed Laser Deposition of Thin Films Applications-Led Growth of Functional Materials*, Hoboken, NJ, USA: John Wiley & Sons, Inc., 2006, ch. 1, sec. 1, pp. 3-31, doi: http://dx.doi.org/10.1002/0470052120.

[4] H.U. Krebs *et al.*, "Pulsed Laser Deposition (PLD) - a Versatile Thin Film Technique", in *Advances in Solid State Physics*, Berlin, Germany, Springer-Verlag, 2003, vol. 43, pp. 505-518, doi: https://doi.org/10.1007/978-3-540-44838-9_36.

[5] S.R.V.S. Prasanna, K. Balaji, S. Pandey, S. Rana, "Metal Oxide Based Nanomaterials and Their Polymer Nanocomposites" in *Nanomaterials and Polymer Nanocomposites,* Elsevier, 2019, ch. 4, pp. 123-144, doi: https://doi.org/10.1016/B978-0-12-814615-6.00004-7.

[6] I.W. Boyd. "Thin Film Growth by Pulsed Laser Deposition", *Ceramics International*, vol. 22, no. 5, pp. 429-434, 1996, doi: https://doi.org/10.1016/0272-8842(95)00086-0.

[7] M. Mews, L. Korte, B. Rech, "Oxygen vacancies in tungsten oxide and their influence on tungsten oxide/silicon heterojunction solar cells", Solar Energy Materials and Solar Cells, vol. 158, part 1, pp. 77-83, Dec. 2016, doi: https://doi.org/10.1016/j.solmat.2016.05.042.

[8] S.R. Droes, T.T. Kodas, M.J Hampden-Smith, "Plasma-Enhanced Chemical Vapor Deposition (PECVD)", in *Carbide, Nitride and Boride Materials Synthesis and Processing*, London, UK, Chapman & Hall, 1997, ch. 23, sec. 8, pp. 579-603, doi: https://doi.org/10.1007/978-94-009-0071-4_23.

[9] *NIST X-ray Photoelectron Spectroscopy Database,* U.S. Department of Commerce, Measurement Services Division of the National Institute of Standards and Technology (NIST), Sept. 2012, http://dx.doi.org/10.18434/T4T88K.

[10] J. W. Weber, V. E. Calado, M. C. M. Van De Sanden, "Optical constants of graphene measured by spectroscopic ellipsometry", *Appl. Phys. Lett.*, vol. 97, no. 9, 2010, doi: https://doi.org/10.1063/1.3475393

[11] J.A Woollam Co, "M-2000 Ellipsometer". [Online]. Available: https://www.jawoollam.com/products/m-2000-ellipsometer

[12] D. Harris, M. Bertolucci, "Vibrational Spectroscopy" in *Symmetry and Spectroscopy: An Introduction to Vibrational and Electronic Spectroscopy*, New York, NJ, USA, Dover Pub. Inc., 1989, ch. 3, pp. 93-224.

[13] B. Chase, "A New Generation of Raman Instrumentation", *Appl. Spectrosc.*, vol. 48, no. 7, pp. 14A-19A, 1994, doi: https://doi.org/10.1366%2F0003702944029848.

[14] Z. Remes, R. Vasudevan, K. Jarolimek, A. Smets. M. Zeman, "The optical spectra of a-Si:H and a-SiC:H thin films measured by the absolute Photothermal Deflection Spectroscopy (PDS)", *Solid State Phenom*., vol. 213, pp. 19-28, 2014, doi: https://doi.org/10.4028/www.scientific.net/SSP.213.19.

[15] M. Singh, R. Santbergen; L. Mazzarella; A. Madrampazakis, G. Yang, R. Vismara, Z. Remes, A. Weeber, M. Zeman, O. Isabella, "Optical characterization of poly-SiO*x* and poly-SiC*x* carrier-selective passivating contacts", *Sol*. *Energy Mater*. *Sol*. *Cells,* vol. 210, 2020, doi: https://doi.org/10.1016/j.solmat.2020.110507.

4 Density of States in Molybdenum Oxide

The application of molybdenum oxide in the photovoltaic field is gaining traction as this material can be deployed in doping-free heterojunction solar cells in the role of hole selective contact. For modeling-based optimization of such contact, knowledge of the molybdenum oxide defect density of states (DOS) is crucial. In this chapter, a method to extract the defect density through nondestructive optical measures, including the contribution given by small polaron optical transitions is reported. The presence of defects related to oxygen-vacancy and of polaron is supported by the results of our opto-electrical characterizations along with the evaluation of previous observations. As part of the analysis, molybdenum oxide samples have been evaluated after post-deposition thermal treatments. Quantitative results are in agreement with the result of density functional theory showing the presence of a defect band fixed at 1.1 eV below the conduction band edge of the oxide.

4.1 Introduction

Typically, HJT structures use a stack of hydrogenated amorphous silicon [1–4] for surface passivation and doped layers that allow high open-circuit voltage in solar cells leading to record efficiencies above 26% [4, 5]. However, a-Si:H layers also exhibit parasitic absorption of photons [6] and a limited thermal budget [7]. In this respect, the use of transition metal oxides (TMO) as an alternative to the doped amorphous silicon layers [8] is gaining particular interest owing to their remarkable optoelectronic properties including low parasitic absorption. Moreover, TMOs deposition can be carried out with simple and low-cost processes [9]. In fact, several groups devoted research works on TMOs-based solar cells [10–19], achieving conversion efficiency values up to 23.5% [20]. Interestingly, TMOs exhibit electronic properties favorable for electron transport as in the case of zinc oxide (ZnO) [21] or titanium dioxide (TiO_2) [22] and also for hole transport as in the case of molybdenum trioxide (MoO_3) [23], vanadium pentoxide (V_2O_5) [24] or tungsten trioxide (WO_3) [15]. In particular, amorphous sub-stochiometric MoO_x (x~3) is the most common TMO for the hole selective contact [9–14]. This material presents good hole selectivity and its large energy gap (around 3 eV) allows optical gain respect to a standard a-Si:H(p) [13].

On the other hand, the hole collection capability of MoO_x is subordinate on its work function and density of trap states near the conduction band [25]. Both properties depend on

Part of this chapter was published in Nano Res., 2020, doi: 10.1007/s12274-020-3029-9 and in Solid State Electron., 2021, doi: 10.1016/j.sse.2021.108135 and was presented at E-MRS 2019 Fall Meeting and at INFOS 2021.

the deposition parameters and post-deposition treatments such as annealing [26]. It should be noted that any optimization of TMOs-based cells requires extensive knowledge of the TMO defect density of states, since it actively contributes to the carrier transport [9] and significantly changes the electrical properties and the passivation ability of the material [27]. For molybdenum oxide, the defect density is derived from the oxygen vacancies [10]. Albeit prior researches reported on the molybdenum oxide DOS [10, 28], the quantitative effect of oxygen vacancies on the density of states in the bandgap of the material has not yet thoroughly investigated, thus restraining the dissemination of accurate optimizations of HJT cells based on MoO_x. Indeed, the need for accurate information on TMO DOS has been highlighted in the optimization efforts of these layers in HJT solar cells by numerical analysis [25, 26]; nevertheless, in these papers, limited data on DOS have been overcome assuming different defect distributions.

This work aims to broaden the current understanding of the transition metal oxide defect density of states, expanding the comprehension on this topic and providing information for accurate and reliable simulations. To obtain accurate results on the DOS, we carried out a compositional and morphological analysis as well as an electro-optical characterization of several MoO_x samples analyzing the effects of post-deposition thermal treatment. Indeed, the annealing studies have been used previously to deepen the understanding of the optoelectrical properties of TMOs [29–31].

We finally estimate the density of states of such samples exploiting the linkage of the absorption coefficient of the material with the DOS [32–34]. Moreover, we considered the effects introduced by small polaron on the absorption coefficient [35]. For this purpose, an absolute photothermal deflection spectroscopy (PDS) setup [34, 36] has been used to evaluate the absorption in a wide spectral range. This innovative approach can be possibly applied to also other transition metal oxides.

4.2 Methodology

4.2.1 Density of States evaluation

We have fitted the PDS absorption spectra, α(hν), by using the so-called one-electron approximation [32]:

$$\alpha(h\nu) = \frac{C}{h\nu}\int N_i(E)F(E)N_f(E+h\nu)[1-F(E+h\nu)]dE \qquad (4.1)$$

where $h\nu$ is the photon energy, C depends on the refractive index and the momentum

matrix elements and is assumed constant for all the optical transitions [32, 37, 38], $N_i(E)$ and $N_f(E)$ represent the density of the initial occupied states and the final empty states, respectively, and $F(E)$ is the Fermi-Dirac function, which describes the probability of energy bands occupancy. The DOS can be modeled as the superposition of several contributions. Following previous works [32, 37, 39], we assume the zero reference for the energy at the edge of the conduction band and the following DOS distributions as in Eq. (4.2): parabolic for valence and conduction bands ($N_{VB}(E)$ and $N_{CB}(E)$ respectively), exponential for the valence and conduction extended states in the band tails ($N_{VBT}(E)$ and $N_{CBT}(E)$) respectively), and a single Gaussian distribution for the inter-bands states related to n-type defects ($N_D(E)$):

$$DOS(E) = \begin{cases} N_{VB}(E) = N_V\sqrt{-E + E_G + E_{0V}} & E < 0 \\ N_{CB}(E) = N_C\sqrt{E - E_{0C}} & E \geq 0 \\ N_{VBT}(E) = N_V\sqrt{\dfrac{E_{0V}}{2}}\ \exp\left(-\dfrac{E + E_G}{E_{0V}}\right) & E > E_G \\ N_{CBT}(E) = N_C\sqrt{\dfrac{E_{0C}}{2}}\exp\left(\dfrac{E}{E_{0C}}\right) & E < 0 \\ N_D(E) = \dfrac{A_D}{\sqrt{2\pi W^2}}\exp\left[-\dfrac{1}{2}\left(\dfrac{E + E_D}{W}\right)^2\right] & E_G < E < 0 \end{cases} \tag{4.2}$$

where N_V, equal to $7.92 \cdot 10^{17}$ $cm^{-3}eV^{-3/2}$, and N_C, equal to $6.78 \cdot 10^{18}$ $cm^{-3}eV^{-3/2}$, are the densities of states at the mobility edge of the valence and the conduction band, respectively; the values have been calculated [40] considering the values of effective masses for electrons and holes reported in [41]; E_{0V} and E_{0C} are the widths of the valence and the conduction band tails; E_G is the energy gap; A_D is the area of the Gaussian distribution while E_D is the position of the Gaussian mean respect to the conduction band and W is the full width at half maximum. The defects modelled with the Gaussian distribution are related to the desorption of oxygen from the lattice of the MoO_x [42].

This extrapolation technique is suitable for materials featuring an absorption spectrum that increases monotonically i.e., amorphous silicon, germanium alloys and polycrystalline silicon. However, transition metal oxides commonly present a peak in the sub-gap absorption region [29], adding complexity to the one-electron approximation. This sub-band absorption peak has been ascribed to a small polaron [43–47], a quasi-particle that describes the interaction of a trapped electron with the surrounding atoms [47, 48]. Furthermore, small polaron is a typical feature of transition metal oxides [44, 49–53]. Thus, to achieve the best fit of the absorption coefficients, we introduce an additive term in Eq.

(4.1) to take into consideration the polaron contribution. The polaron absorption, $\alpha_p(E)$, is modeled with a weakly asymmetric Gaussian peak [44, 45, 53]:

$$\alpha_p(h\nu) = \frac{A_p}{h\nu} \exp\left(-\frac{\left(h\nu - 2E_p\right)^2}{8E_p\, E_{op}}\right) \tag{4.3}$$

where A_p, is the pre-exponential factor, E_p is the polaron binding energy, and E_{op} is the longitudinal-optical phonon energy. The values for these parameters are extrapolated from the fitting process. The presence of small polarons in MoO_x is further confirmed by the effect of thermal annealing on the absorption spectra (see Figure 4.3). As stated above, the absorption increase in the annealed samples is likely to be ascribed to reactions of reduction, from Mo^{6+} to Mo^{5+} states. These reduced states produce crystallographic defects where electrons are confined, the so-called *color centers* [29, 49, 54],. The formation of such color centers is closely linked to the presence of polaron [49, 55, 56]. Moreover, small polarons are considered responsible for the conductivity in molybdenum oxide [57].

Introducing the polaron contribution in Eq. (4.1) gives the following equation:

$$\alpha(h\nu) = \frac{C}{h\nu} \int N_i(E) F(E) N_f(E + h\nu)[1 - F(E + h\nu)]dE + \alpha_p(h\nu) \tag{4.4}$$

4.2.2 Experimental details

Layers of molybdenum oxide were deposited by physical vapor deposition (PVD) technique on quartz substrates. The Molybdenum (VI) oxide (Sigma-Aldrich, 99.98%) precursor was thermally evaporated in a vacuum chamber at $5 \cdot 10^{-6}$ mbar at rates between 0.2 and 0.5 nm/s. To obtain uniform layers with thicknesses aiming at 20, 50 and 100 nm, the substrates were continuously rotated at 10 rpm during the deposition process. Afterward, the samples were annealed for 30 minutes at different temperatures (100, 130, 150, 200 and 250 °C) and by varying the environment conditions: ambient air (atmospheric pressure), hydrogen (2 mbar) or argon (2 mbar). After the deposition, in order to avoid any additional oxidation process in the MoO_x due to the air exposure [58], the samples were stored and sealed in a nitrogen environment.

The thicknesses of the layers were evaluated employing spectroscopic ellipsometry (SE) using a combination of Tauc-Lorentz and Gaussian oscillators [59]. To get information on the composition of the samples, X-ray photoelectron spectra (XPS) were measured. Samples were excited with Al-Kα X-ray radiation using pass energy of 5.85 eV. The structural evaluation of the MoO_x films has been investigated by a Raman spectroscopy

acquired at 514 nm excitation wavelength. The optical absorption of the samples was extracted from a photothermal deflection spectroscopy (PDS) setup [34, 36], by measuring the deflection of a He-Ne laser beam tangent to the sample edge. This deflection is proportional to the absorption within the sample and exhibits superior sensitivity over transmittance/reflectance spectrophotometry; as such, it has been extensively used to analyze electronic defects in semiconductors [60] and recently, to characterize amorphous transition metal oxides as MoO_x, WO_x and VO_x [61]. Finally, measurements of conductivity have been performed in a co-planar configuration after the deposition of two aluminum electrodes on the MoO_x films.

4.3 Results and discussion

We evaluate the DOS of various MoO_x films for different thermal processes, environments and layer thicknesses. An insight on the material is given through compositional and morphological analysis including an optoelectrical characterization. All collected data are used for the extraction of the DOS and used to investigate the application of MoO_x as hole-selective passivating contact in HJT solar cells. Here, we highlight the decisive role that these defect states play in an efficient trap assisted tunneling (TAT) transport.

4.3.1 Chemical and structural properties

The composition and the presence of oxygen vacancies in the MoO_x samples were evaluated through XPS. The results shown in Figure 4.1 are related to the 50-nm thick sample annealed in air at 100 °C. The Mo 3d binding region is hereby deconvoluted: a doublet structure with peaks at 232.8 and 235.9 eV can be highlighted; the spin-orbit separation is 3.0 eV and the intensity ratio between the two component peaks is given as 3:2. Thus, the Mo 3d level is resolved with the superposition of two doublet components: a dominating doublet associated with the Mo^{6+} [62, 63] and a weak doublet shifted 2 eV to lower energy. This last component is caused by some surface reduction during the deposition process in a vacuum and it is reported as Mo^{5+} states associated to oxygen vacancies [64]; moreover, it has been previously shown that these reduced states can be further increased by post-deposition annealing [62, 65, 66]. In our case, XPS measurements show the presence of Mo^{5+} states in all the evaluated samples.

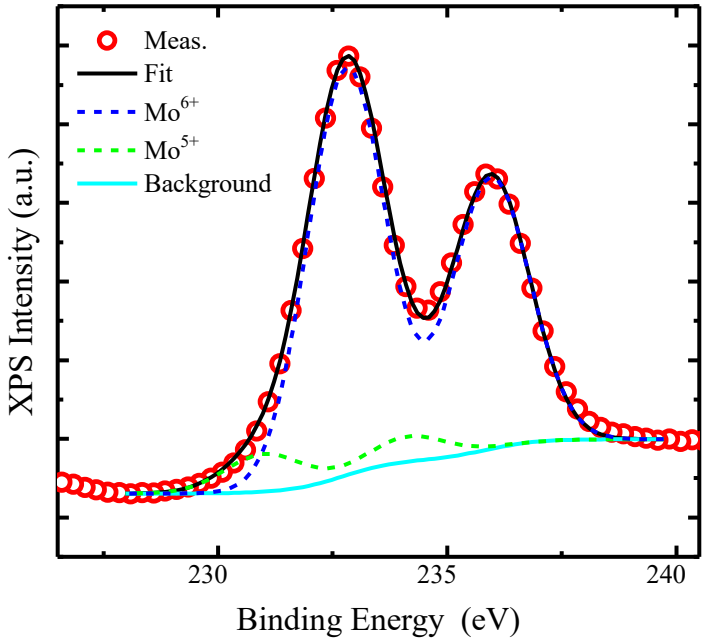

Figure 4.1 *X-ray deconvoluted photoelectron spectrum of the Mo 3d binding region, of the 50-nm thick MoO_x sample annealed in air at 100 °C. Al Kα X-ray satellite structures were subtracted before to process the data.*

To identify whether our deposited films present crystalline phases after annealing, we evaluated their Raman spectra. Figure 4.2 depicts the results in case of the 100-nm thick MoO_x layers annealed in air at 250°C and 100°C. The as-deposited sample is also shown as a reference for the analysis. We observe that (i) there are no sharp peaks in the spectra and (ii) the signal can be likely referred to as some background due to the substrate [67], indicating that the material is amorphous. Presence of broad peaks of low intensity at 470 and 830 cm^{-1}, related to the stretching mode for α-MoO_3 crystalline phase [68], can be noted in the as-deposited and in the annealed at 100 °C sample; these peaks decrease at 250°C while the one at 970 cm^{-1} start to increase suggesting that the material maintains the amorphous disordered structure and a longer annealing time with a higher temperature is required to start crystallization [30, 64]. Similar behavior was measured for 20-nm and 50-nm thick samples annealed in Air and H_2, but they are not reported here for the sake of brevity.

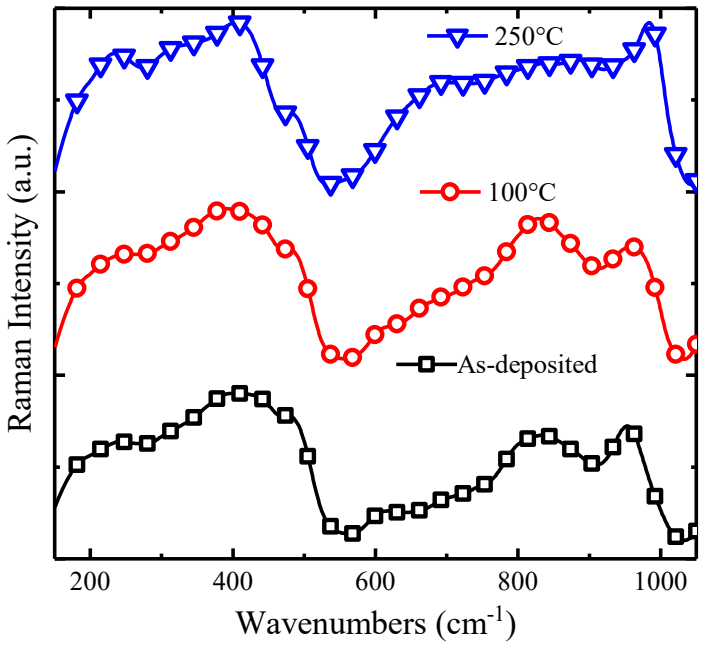

Figure 4.2 *Raman spectra of the 100-nm thick MoO_x layer as-deposited and after annealing in air at 100 and 250 °C. The curves are displaced vertically in the graph for better visualization.*

4.3.2 Opto-electrical characterization

Figure 4.3 depicts the absorption spectra of 20-nm thick molybdenum samples: each series of measurements is grouped according to the annealing gas (air, hydrogen and argon). It is noteworthy that similar trends were also observed for 50-nm and 100-nm thick samples. Essentially, the absorption in each spectrum grows from lower energies to a peak located around 1.5 eV; then it decreases to a valley around 2.5-3 eV and finally rises exponentially. These absorption measurements are consistent with other results described in the literature [29, 30]. There are no significant differences between the curves in the energy interval 3-4 eV; while the peak observed in the Vis-NIR range tendentially grows as the annealing temperature rises. This increase in the absorption is likely to be referred to MoO_x reduction in the annealed samples. The only exception occurs in the sample annealed in air at 250 °C (see Figure 4.3a), which presents an absorption coefficient slightly smaller than the one annealed at 200 °C. The oxidation reaction of the MoO_x can explain this saturation phenomenon during annealing when oxygen is present, bringing evidence that annealing in the oxygen-rich atmosphere slows down the generation of oxygen vacancies. In fact, when argon and hydrogen are used for the annealing, the oxidation reaction does not occur and the absorption spectrum of the sample at 250 °C is higher than the one annealed at 200 °C, as noticeable in Figure 4.3b and Figure 4.3c.

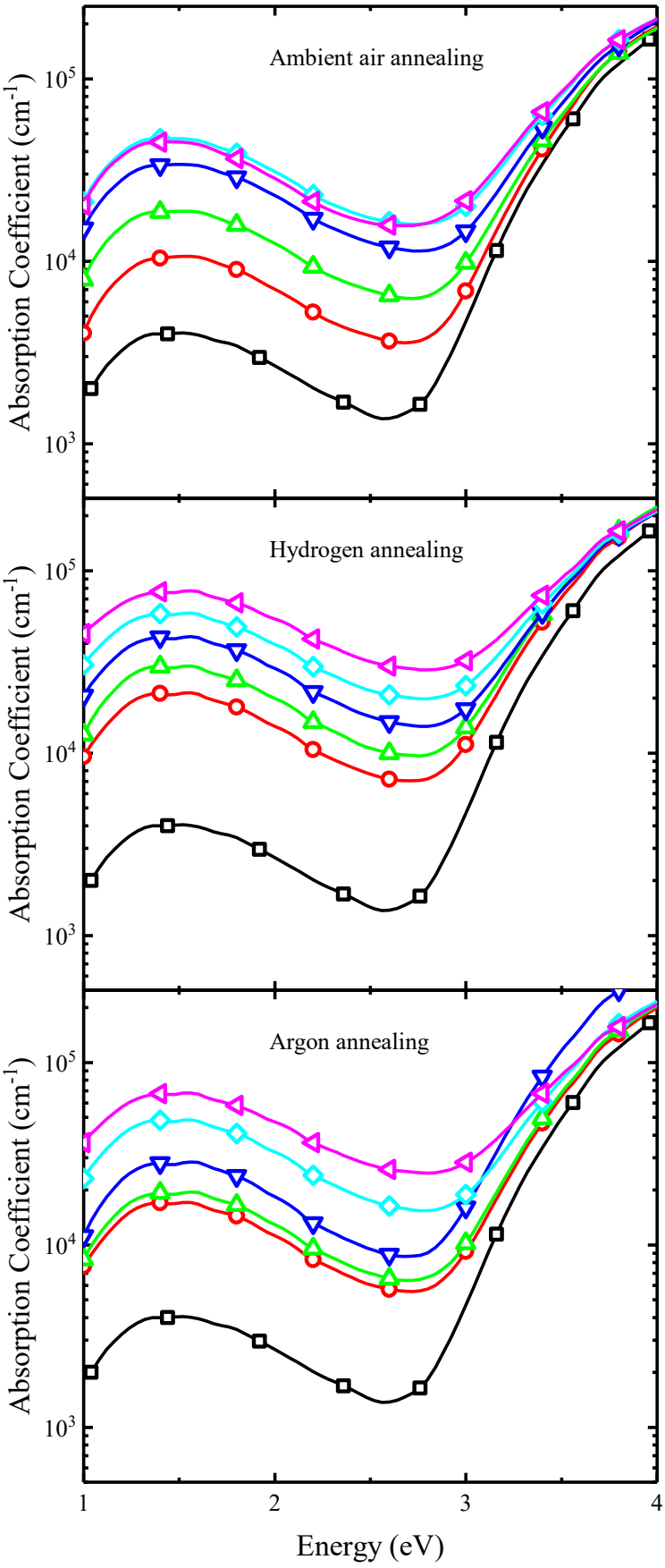

Figure 4.3 *Absorption spectra of MoO_x layers 20 nm thick annealed in different atmospheres: a) ambient air, b) hydrogen and c) argon.*

The optical band gap, E_{opt}, of each sample has been evaluated by using the Tauc's law [69], that is from the linear extrapolation of the (αhν)2 versus hν plot. Resulting values lay within the range from 2.7 to 3 eV for the 20-nm thick annealed MoO_x films (see Figure 4.4a). The as-deposited film presents the highest E_{opt}, with a value slightly above 3 eV; while, by increasing the annealing temperature, the gap decreases steadily with the lowest E_{opt} when the annealing is carried out in hydrogen.

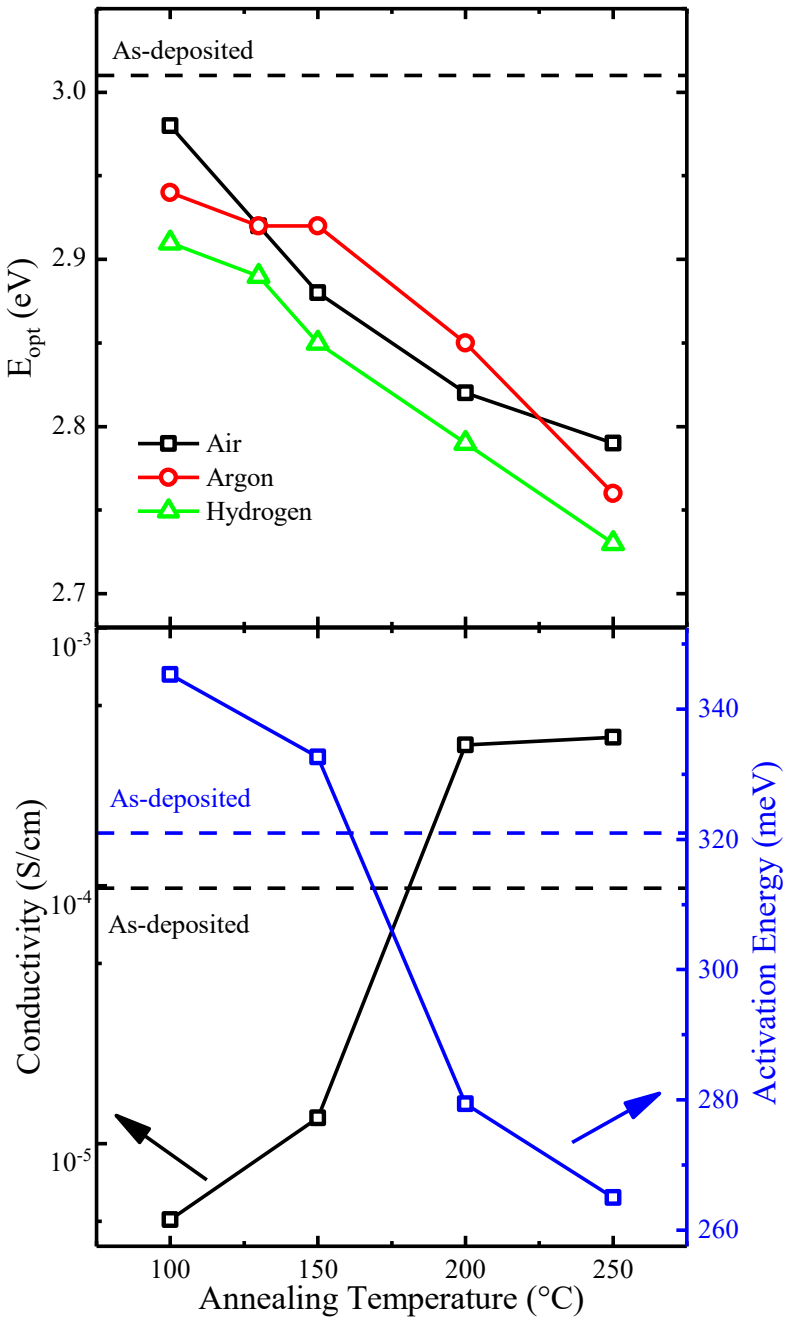

Figure 4.4 *a) Optical bandgap energies of 20-nm thick MoO_x annealed in different atmospheres. b) Conductivity (right axis) and activation energy (left axis) of 20-nm thick MoO_x annealed in air. The dashed lines in b) correspond to the as-deposited reference sample.*

The optical bandgap has been further evaluated by means of other two models. With respect to the Tauc's model, the Ulrich's empirical model for the direct bandgap or the band fluctuation models [70, 71] allow distinguishing between the absorption edge and absorption tails [72]. The resulting optical bandgaps are summarized in Table 4.1. Regarding Ulrich's model, the bandgap values are slightly higher (around 3%) than the corresponding optical gaps obtained with Tauc's model. Moreover, these values confirm the descending trend with the increasing annealing temperature. The band fluctuating model resulted in higher bandgap values respect to the Ulrich's and Tauc's ones (about 24% higher). Even in this case, the same trend with the annealing temperature observed with the previous models is confirmed. Indeed, the values retrieved with the Tauc's plot are close to the ones retrieved with Ulrich's model and agree with previous observations [30], while the values retrieved with the band fluctuation model are higher.

Table 4.1 *Optical energy gap extracted with different models from the absorption coefficient of the 20-nm thick MoO_x films annealed at different temperatures and in different annealing ambiances*

Temp. (°C)	*Atm.*	*Tauc, E_{opt} (eV)*	*Ulrich, E_{Ulrich} (eV)*	*Band fluctuation, E_{BF} (eV)*
As-deposited		3.01	3.12	3.67
100	Air	2.98	3.07	3.62
130	Air	2.92	3.02	3.62
150	Air	2.88	2.95	3.57
200	Air	2.82	2.87	3.54
250	Air	2.79	2.83	3.54
100	H_2	2.91	2.98	3.57
130	H_2	2.89	2.94	3.53
150	H_2	2.85	2.90	3.56
200	H_2	2.79	2.87	3.55
250	H_2	2.73	2.73	3.55
100	Ar	2.94	3.03	3.60
130	Ar	2.92	3.00	3.58
150	Ar	2.92	2.86	3.40
200	Ar	2.85	2.89	3.54
250	Ar	2.76	2.77	3.57

Figure 4.4b reports the measured conductivity and the activation energy, E_A, extracted from the Arrhenius equation [57] for the same samples of Figure 4.4a. With respect to the reference as-deposited sample, the conductivity is lower after annealing at 100 °C and 150 °C, while it increases drastically for annealing temperature at 200 °C. In line with what observed in the absorption spectra of the air-annealed samples (see Figure 4.3a), saturation

in the conductivity of the material is noted for temperature from 200 °C to 250 °C. As expected, the opposite trend (lower values at a higher temperature) was observed for the activation energy. E_A at 250 °C is in fact 266 meV against the 320 meV of the reference sample. This reveal, consistently with [66], that the annealing treatment produces oxygen vacancies, thus increasing the number of free electrons. As previously reported [73], the higher presence of free electrons due to oxygen vacancies makes the position of the Fermi level closer to the conduction band edge, rising the conductivity of the material while decreasing its optical gap.

Since the determination of the constant *C* is needed for the quantitative extraction of the DOS parameters, the integral in Eq. (4.4) has been calibrated using the absorption coefficients measured at 4 eV; at this energy, the absorption is dominated by the optical transition from the valence to the conduction band [32]. Moreover, at this energy, the samples share the same value of the absorption coefficient, which strongly suggests that we can assume the same coefficient C, equal to $4.13 \cdot 10^{-31}$ $cm^5 \cdot eV^2$.

Figure 4.5 presents an example of deconvoluted absorption in case of 20-nm thick sample annealed in air at 200 °C. The absorption spectrum is composed of many contributions and the fit is excellent when they are all summed together. More precisely, the optical transitions considered in our procedure are: between bands, from $N_{VB}(E)$ to $N_{CB}(E)$, $T_{VB\text{-}CB}$; between band tails, from $N_{VBT}(E)$ to $N_{CBT}(E)$, $T_{VBT\text{-}CBT}$; from the valence band tail to the conduction band, $T_{VBT\text{-}CB}$; from the valence band to the conduction band tail, $T_{VB\text{-}CBT}$; from inter-band defects to the conduction band, TD-CB; from inter-band defects to the conduction band tails, $T_{D\text{-}CBT}$; polaronic transitions, $T_{Polaron}$, which give rise to the optical absorption peak around 1.5 eV.

A summary of the parameters resulted from the deconvolution process is given in Table 4.2. The fitting values of distributions described by Eq. (4.2) are related to the 20-nm thick MoO_x layers. We applied this procedure systematically to analyze all absorption spectra measured and a perfect fit can be obtained also in samples with greater thickness.

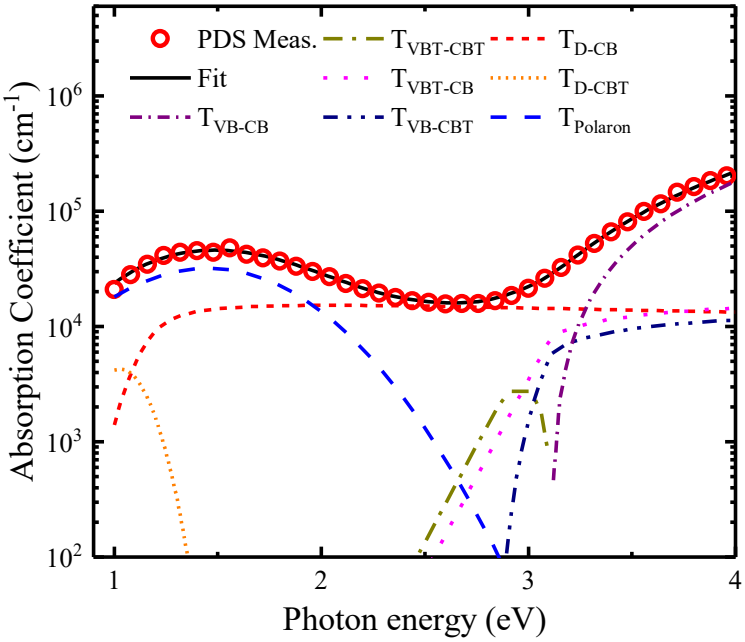

Figure 4.5 *Fit (solid line) of the PDS measurement of absorption coefficient (empty circles) of the 20-nm thick MoO_x sample annealed in air at 200 °C.*

Table 4.2 *DOS parameters extracted from the deconvolution of the absorption coefficient for the 20-nm thick MoO_x films annealed at different temperatures and in different annealing ambiances*

Temp. (°C)	*Atm*	*E_{0V} (meV)*	*E_{0C} (meV)*	*A_D ($eV^{-1}\cdot cm^{-3}$)*	*E_D (eV)*	*W (meV)*	*A_P ($eV^{-1}\cdot cm^{-3}$)*	*E_P (eV)*	*E_{op} (meV)*
As-deposited		109	84	9.21E+14	1.10	30	4.32E+03	0.800	50.0
100	Air	89	59	2.69E+15	1.10	20	1.13E+04	0.795	50.3
130	Air	93	55	3.86E+15	1.10	20	2.18E+04	0.810	54.4
150	Air	84	43	6.79E+15	1.10	20	3.95E+04	0.810	62.5
200	Air	88	56	1.15E+16	1.10	20	5.06E+04	0.795	52.9
250	Air	99	59	1.05E+16	1.10	20	4.89E+04	0.785	51.0
100	H2	91	49	4.32E+15	1.11	20	2.46E+04	0.805	57.4
130	H2	84	35	5.75E+15	1.09	20	3.52E+04	0.810	59.8
150	H2	86	42	8.93E+15	1.09	30	4.91E+04	0.810	59.8
200	H2	93	64	1.37E+16	1.11	30	6.12E+04	0.800	55.1
250	H2	104	65	1.86E+16	1.14	30	7.53E+04	0.805	54.8
100	Ar	87	51	3.71E+15	1.11	20	1.93E+04	0.795	58.1
130	Ar	85	52	3.93E+15	1.09	20	2.25E+04	0.810	57.1
150	Ar	63	59	4.29E+15	1.11	20	3.44E+04	0.825	61.4
200	Ar	85	38	1.09E+16	1.10	30	5.24E+04	0.800	50.0
250	Ar	103	65	1.72E+16	1.12	30	7.01E+04	0.795	66.5

We note that for all the samples the values of E_{0V} are higher than the respective E_{0C}, while the as-deposited sample highlights the highest values of slope in both the valence and conduction band tails. While the values of E_{0V} and E_{0C} related to the annealed samples do not show any specific trend in function of the temperature, they fluctuate around a mean

value of 89 meV for the valence band and 53 meV for the conduction band.

Regarding the defect density, since the absorption coefficient of the sample annealed in air at 250 °C does not differ from the one annealed at 200 °C, A_D saturates at these temperatures. However, as Figure 4.6a shows, when the annealing is performed in different atmospheres, the area of the defects increases linearly with temperature. This analysis brings evidence that annealing in the oxygen-rich atmosphere slows down the generation of oxygen vacancies. The defect area of the as-deposited layer is always lower than the ones relative to the annealed sample; in particular, A_D of the sample annealed in hydrogen or in air ambiance at 250 °C is 13 or 7 times, respectively, larger than in the case of as-deposited sample. The resulting values of the other Gaussian parameters are rather insensitive to the annealing process: E_D is fixed at around 1.10 eV below the conduction band edge with standard deviations varying among 20 and 30 meV. This energy position is in agreement with reported results from density functional theory [42]. Figure 4.6 also shows the data related to the pre-exponential factor of the polaron absorption, A_P. The trend is similar to the one observed for the area of the inter-band defects. Also, in this case, the parameters related to the polaron absorption after annealing are always higher than the as-deposited case, given as a reference. Finally, E_P and E_{op} resulted unchanged by the annealing conditions, with mean values of 800 meV and 55 meV, respectively.

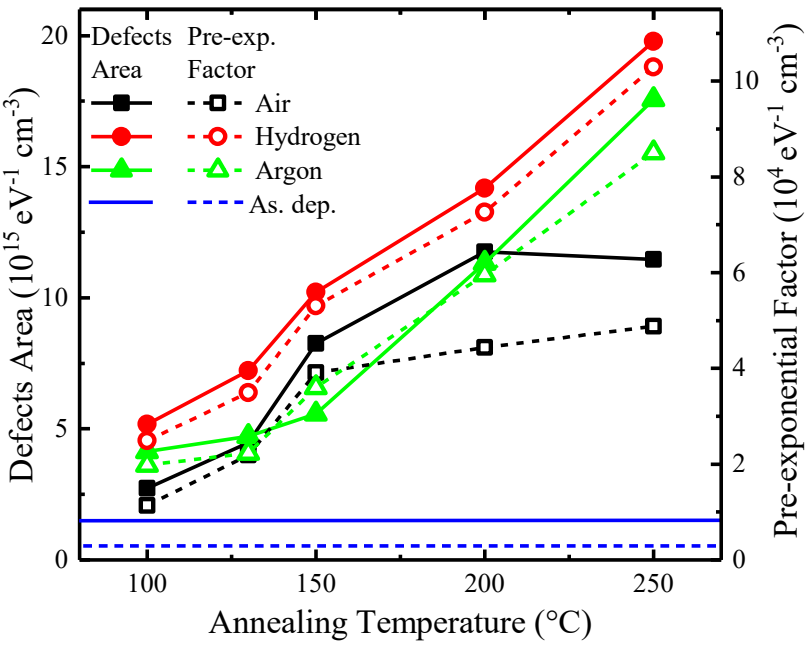

Figure 4.6 *Area of the inter-band defects (left axis) and pre-exponential factor of the polaron absorption (right axis) as a function of the annealing temperature for different annealing ambiances.*

4.3.3 Application in HJT solar cells

The energy band diagram of a solar cell with hole-selective contact based on MoOx, with a high trap density inside its bandgap, can be sketched as in Figure 4.7. The high bandgap of MoOx and its low activation energy leads to a broad band-bending at the c-Si absorber interface that is crucial for transport selectivity and fill factor [74]. The significant energy barrier at the interface between the TMO layer and the intrinsic a-Si:H creates an efficient electron blocking at the p-type contact whereas the photogenerated holes can be collected via tunneling mechanisms [75] such as the band to band (BTB) and the trap assisted (TA). Since the conduction band, EC, of the MoOx is aligned with the valence band, E_V, of the a-Si:H(i), the BTB tunneling is predominant. Nevertheless, the presence of defects states in the bandgap, as investigated previously, plays a crucial role that supports the carrier transport by TAT [25]. Notably, the carrier transport by trap assisted tunneling relies on the extended states close to the conduction band of the TMO rather than the oxygen vacancies, which are located about 1.1 eV below the band edge. It is worth noting that any optimization of MoO_x-based solar cells has to take into account the effects of thermal annealing as any post-deposition treatment increases the defects DOS, reduces the activation energy and lowers the energy gap of the material.

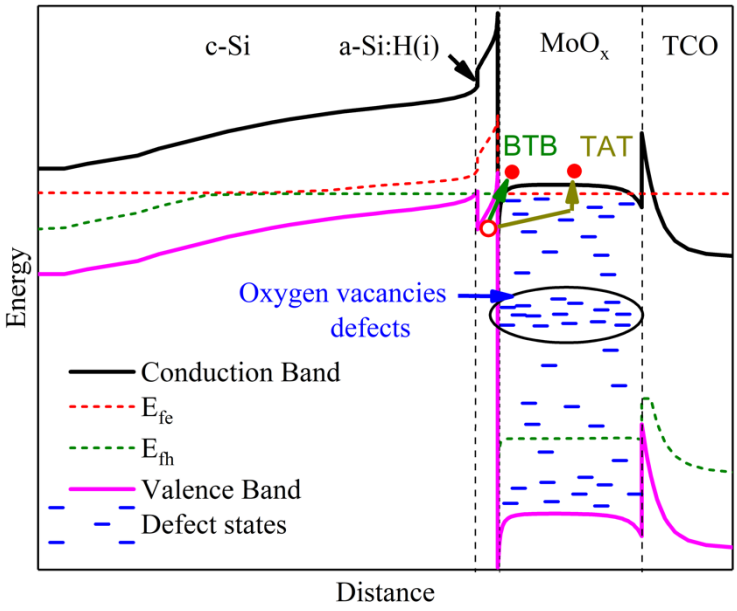

Figure 4.7 *Sketch of the energy band diagram across the c-Si/a-Si:H(i)/MoO_x/TCO stack in a Si heterojunction solar cell under illumination. The dashed lines mark the quasi-Fermi level of electrons, E_{fe}, and holes, E_{fh}. The scale of x-axis is logarithmic for better readability.*

4.4 Conclusions

In this chapter, analysis and characterization of amorphous molybdenum oxide samples have been performed. For this purpose, thin films of non-stoichiometric amorphous MoO_x oxide were produced by thermal evaporation in vacuo at room temperature. The thickness of the films was varied between 20 and 100 nm and these values were confirmed through spectroscopic ellipsometry. Optical spectra displayed a pronounced absorption peak in the near-infrared range which has been associated with small polaron absorption. The related energy positions remained constant after the post-deposition thermal treatment while its peak values increased. The explanation of this phenomenon can be found in the binding between the small polaron formation and the defect formation, since, during the annealing, oxygen deficiencies create positively charged oxygen vacancies with accompanying charge-compensating electrons. From the fitting of the experimental absorption spectra, through the evaluation of optical transition over the bandgap and from the result of polaron theory, it was found that the inter-band defect density lays centered around 1.1 eV below the edge of the conduction band with a width of 20 meV while the peak rises in function of the annealing temperature, moreover the sample annealed in air are quite insensitive to temperature variation over 200 °C. The polaron binding energy resulted in approximately 1.57 eV while the longitudinal-optical phonon energy in 55 meV. The value of the slope of the exponential valence tail resulted slightly higher than the conduction tail and showed no change during the annealing process while both values are lower than the as-deposited sample.

Numerical information on the DOS of MoO_x as well as other transition metal oxides is still missing. Without this data, any simulation of solar cells endowed with such materials risk to be not accurate or even physically feasible. From our analysis and polaron theory, it was possible to obtain parameters useful to simulate MoO_x in advanced device simulators appropriately. Data shown here represent a first step in the characterization framework that can be extended to other transition metal oxides exhibiting similar behavior, such as tungsten trioxide, vanadium pentoxide, and titanium dioxide.

References

[1] K. Masuko *et al.,* "Achievement of more than 25% conversion efficiency with crystalline silicon heterojunction solar cell," *IEEE J. Photovoltaics*, vol. 4, no. 6, pp. 1433–1435, 2014, doi: https://doi.org/10.1109/JPHOTOV.2014.2352151.

[2] H. A. Gatz, J. K. Rath, M. A. Verheijen, W. M. M. Kessels, and R. E. I. Schropp, "Silicon heterojunction solar cell passivation in combination with nanocrystalline silicon oxide emitters," *Phys. Status Solidi Appl. Mater. Sci*., vol. 213, no. 7, pp. 1932–1936, Jul. 2016, doi: https://doi.org/10.1002/pssa.201532945.

[3] G. Yang *et al*., "High-efficiency black IBC c-Si solar cells with poly-Si as carrier-selective passivating contacts," *Sol. Energy Mater. Sol. Cells*, vol. 186, pp. 9–13, 2018, doi: https://doi.org/10.1016/j.solmat.2018.06.019.

[4] K. Yoshikawa *et al*., "Silicon heterojunction solar cell with interdigitated back contacts for a photoconversion efficiency over 26%," i, vol. 2, no. 5, May 2017, doi: https://doi.org/10.1038/nenergy.2017.32.

[5] M. A. Green *et al*., "Solar cell efficiency tables (version 57)," *Prog. Photovoltaics Res. Appl*., vol. 29, no. 1, pp. 3–15, 2017, doi: https://doi.org/10.1002/pip.3371.

[6] Z. C. Holman *et al*., "Current losses at the front of silicon heterojunction solar cells," *IEEE J. Photovoltaics*, vol. 2, no. 1, pp. 7–15, Jan. 2012, doi: https://doi.org/10.1109/JPHOTOV.2011.2174967.

[7] J. Melskens, B. W. H. Van De Loo, B. Macco, L. E. Black, S. Smit, and W. M. M. Kessels, "Passivating Contacts for Crystalline Silicon Solar Cells: From Concepts and Materials to Prospects," *IEEE J. Photovoltaics,* vol. 8, no. 2, pp. 373–388, 2018, doi: https://doi.org/10.1109/JPHOTOV.2018.2797106.

[8] L. G. Gerling *et a*l., "Transition metal oxides as hole-selective contacts in silicon heterojunctions solar cells," *Sol. Energy Mater. Sol. Cells*, vol. 145, pp. 109–115, 2016, doi: https://doi.org/10.1016/j.solmat.2015.08.028.

[9] C. Yu, S. Xu, J. Yao, and S. Han, "Recent advances in and new perspectives on crystalline silicon solar cells with carrier-selective passivation contacts," *Crystals*, vol. 8, no. 11, 2018, doi: https://doi.org/10.3390/cryst8110430.

[10] C. Battaglia *et al*., "Hole selective MoOx contact for silicon solar cells," Nano Lett., vol. 14, no. 2, pp. 967–971, Feb. 2014, doi:

https://doi.org/10.1021/nl404389u.

[11] J. Shi *et al*., "MoOx modified ITO/a-Si:H(p) contact for silicon heterojunction solar cell application," *Mater. Res. Bull*., vol. 97, pp. 176–181, Jan. 2018, doi: https://doi.org/10.1016/j.materresbull.2017.09.005.

[12] M. Bivour, J. Temmler, H. Steinkemper, and M. Hermle, "Molybdenum and tungsten oxide: High work function wide band gap contact materials for hole selective contacts of silicon solar cells," *Sol. Energy Mater. Sol. Cells*, vol. 142, pp. 34–41, 2015, doi: https://doi.org/10.1016/j.solmat.2015.05.031.

[13] J. Geissbühler *et al*., "22.5% Efficient Silicon Heterojunction Solar Cell With Molybdenum Oxide Hole Collector," *Appl. Phys. Lett*., vol. 107, no. 8, 2015, doi: https://doi.org/10.1063/1.4928747.

[14] K. Mallem *et al.,* "Molybdenum oxide: A superior hole extraction layer for replacing p-type hydrogenated amorphous silicon with high efficiency heterojunction Si solar cells," *Mater. Res. Bull*., vol. 110, pp. 90–96, Feb. 2019, doi: https://doi.org/10.1016/j.materresbull.2018.10.018.

[15] M. Mews, A. Lemaire, and L. Korte, "Sputtered Tungsten Oxide as Hole Contact for Silicon Heterojunction Solar Cells*," IEEE J. Photovoltaics*, vol. 7, no. 5, pp. 1209–1215, 2017, doi: https://doi.org/10.1109/JPHOTOV.2017.2714193.

[16] X. Yang, Q. Bi, H. Ali, K. Davis, W. V. Schoenfeld, and K. Weber, "High-Performance TiO2-Based Electron-Selective Contacts for Crystalline Silicon Solar Cells," *Adv. Mater*., vol. 28, no. 28, pp. 5891–5897, 2016, doi: https://doi.org/10.1002/adma.201600926.

[17] R. García-Hernansanz *et al*., "Transport mechanisms in silicon heterojunction solar cells with molybdenum oxide as a hole transport layer*," Sol. Energy Mater. Sol. Cells,* vol. 185, no. January, pp. 61–65, 2018, doi: https://doi.org/10.1016/j.solmat.2018.05.019.

[18] W. Lan, Y. Wang, J. Singh, and F. Zhu, "Omnidirectional and Broadband Light Absorption Enhancement in 2-D Photonic-Structured Organic Solar Cells," *ACS Photonics,* vol. 5, no. 3, pp. 1144–1150, 2018, doi: https://doi.org/10.1021/acsphotonics.7b01573.

[19] H. Wu *et al*., "Improving CNT-Si solar cells by metal chloride-to-oxide transformation," *Nano Res.,* vol. 13, no. 2, pp. 543–550, 2020, doi:

https://doi.org/10.1007/s12274-020-2648-5.

[20] J. Dréon *et al*., "23.5%-Efficient Silicon Heterojunction Silicon Solar Cell Using Molybdenum Oxide As Hole-Selective Contact," *Nano Energy*, vol. 70, 2020, doi: https://doi.org/10.1016/j.nanoen.2020.104495.

[21] S. K. Hau, H. L. Yip, N. S. Baek, J. Zou, K. O'Malley, and A. K. Y. Jen, "Air-stable inverted flexible polymer solar cells using zinc oxide nanoparticles as an electron selective layer," *Appl. Phys. Lett.,* vol. 92, no. 25, pp. 1–4, 2008, doi: https://doi.org/10.1063/1.2945281.

[22] X. Yin *et al*., "19.2% Efficient InP Heterojunction Solar Cell with Electron-Selective TiO2 Contact," *ACS Photonics*, vol. 1, no. 12, pp. 1245–1250, 2014, doi: https://doi.org/10.1021/ph500153c.

[23] B. Li, H. Ren, H. Yuan, A. Karim, and X. Gong, "Room-Temperature, Solution-Processed MoOx Thin Film as a Hole Extraction Layer to Substitute PEDOT/PSS in Polymer Solar Cells," *ACS Photonics*, vol. 1, no. 2, pp. 87–90, 2014, doi: https://doi.org/10.1021/ph4000168.

[24] K. Zilberberg *et al.,* "Inverted organic solar cells with sol-gel processed high work-function vanadium oxide hole-extraction layers*," Adv. Funct. Mater*., vol. 21, no. 24, pp. 4776–4783, 2011, doi: https://doi.org/10.1002/adfm.201101402.

[25] C. Messmer, M. Bivour, J. Schon, S. W. Glunz, and M. Hermle, "Numerical Simulation of Silicon Heterojunction Solar Cells Featuring Metal Oxides as Carrier-Selective Contacts*," IEEE J. Photovoltaics*, vol. 8, no. 2, pp. 456–464, 2018, doi: https://doi.org/10.1109/JPHOTOV.2018.2793762.

[26] R. A. Vijayan *et al*., "Hole-Collection Mechanism in Passivating Metal-Oxide Contacts on Si Solar Cells: Insights from Numerical Simulations," *IEEE J. Photovoltaics,* vol. 8, no. 2, pp. 473–482, 2018, doi: https://doi.org/10.1109/JPHOTOV.2018.2796131.

[27] P. M. P. Salomé *et al.,* "Passivation of Interfaces in Thin Film Solar Cells: Understanding the Effects of a Nanostructured Rear Point Contact Layer," *Adv. Mater. Interfaces,* vol. 5, no. 2, pp. 1–10, 2018, doi: https://doi.org/10.1002/admi.201701101.

[28] L. C. Hao, M. Zhang, M. Ni, J. M. Liu, and X. D. Feng, "Simulation of high efficiency silicon heterojunction solar cells with molybdenum oxide carrier

selective layer," *Mater. Res. Express*, vol. 5, no. 7, 2018, doi: https://doi.org/10.1088/2053-1591/aace80.

[29] J. Werner *et al*., "Parasitic Absorption Reduction in Metal Oxide-Based Transparent Electrodes: Application in Perovskite Solar Cells," *ACS Appl. Mater. Interfaces*, vol. 8, no. 27, pp. 17260–17267, 2016, doi: https://doi.org/10.1021/acsami.6b04425.

[30] T. S. Sian and G. B. Reddy, "Optical, structural and photoelectron spectroscopic studies on amorphous and crystalline molybdenum oxide thin films," *Sol. Energy Mater. Sol. Cells,* vol. 82, no. 3, pp. 375–386, 2004, doi: https://doi.org/10.1016/j.solmat.2003.12.007.

[31] A. Lyubchyk *et a*l., "Influence of post-deposition annealing on electrical and optical properties of ZnO-based TCOs deposited at room temperature," *Phys. Status Solidi Appl. Mater. Sci.*, vol. 213, no. 9, pp. 2317–2328, 2016, doi: https://doi.org/10.1002/pssa.201532891.

[32] H. Fritzsche, J. Kočka, M. Vaněček, and A. Tříska, " ENERGY AND DENSITY OF GAP STATES IN a-Si:H ," in *Amorphous Silicon and Related Materials*, H. Frtitzsche, Ed. WORLD SCIENTIFIC, 1989, pp. 297–327, doi: https://doi.org/10.1142/9789814434157_0011.

[33] M. Vaněček, J. Kočka, J. Stuchlík, Z. Kožíšek, O. Štika, and A. Tříska, "Density of the gap states in undoped and doped glow discharge a-Si:H," *Sol. Energy Mater*., vol. 8, no. 4, pp. 411–423, 1983, doi: https://doi.org/10.1016/0165-1633(83)90006-0.

[34] Z. Remes, R. Vasudevan, K. Jarolimek, A. H. M. Smets, and M. Zeman, "The optical spectra of a-Si:H and a-SiC:H thin films measured by the absolute photothermal deflection spectroscopy (PDS)," *Solid State Phenom*., vol. 213, pp. 19–28, 2014, doi: https://doi.org/10.4028/www.scientific.net/SSP.213.19.

[35] D. Scirè, P. Procel, A. Gulino, O. Isabella, M. Zeman, and I. Crupi, "Sub-gap defect density characterization of molybdenum oxide: An annealing study for solar cell applications," *Nano Res*., vol. 13, no. 12, pp. 3416–3424, 2020, doi: https://doi.org/10.1007/s12274-020-3029-9.

[36] M. Singh *et al*., "Optical characterization of poly-SiOx and poly-SiCx carrier-selective passivating contacts," *Sol. Energy Mater. Sol. Cells*, vol. 210, 2020, doi:

https://doi.org/10.1016/j.solmat.2020.110507.

[37] Y. Bouizem, A. Belfedal, J. D. Sib, and L. Chahed, "Density of states in hydrogenated amorphous germanium seen via optical absorption spectra," *Solid State Commun.*, vol. 126, no. 12, pp. 675–680, 2003, doi: https://doi.org/10.1016/S0038-1098(03)00271-0.

[38] W. B. Jackson, S. M. Kelso, C. C. Tsai, J. W. Allen, and S. J. Oh, "Energy dependence of the optical matrix element in hydrogenated amorphous and crystalline silicon," *Phys. Rev. B*, vol. 31, no. 8, pp. 5187–5198, Apr. 1985, doi: https://doi.org/10.1103/PhysRevB.31.5187.

[39] M. Van Sebille, R. A. Vasudevan, R. J. Lancee, R. A. C. M. M. Van Swaaij, and M. Zeman, "Optical characterization and density of states determination of silicon nanocrystals embedded in amorphous silicon based matrix," *J. Phys. D. Appl. Phys.*, vol. 48, no. 32, p. 325302, Aug. 2015, doi: https://doi.org/10.1088/0022-3727/48/32/325302.

[40] S. M. Sze and K. N. Kwok, *Physics of Semiconductor Devices,* 3rd ed. Wiley, 2006.

[41] A. H. Reshak, "Specific features of electronic structures and optical susceptibilities of molybdenum oxide," *RSC Adv.*, vol. 5, no. 28, pp. 22044–22052, 2015, doi: https://doi.org/10.1039/c5ra00081e.

[42] S. O. Akande, A. Chroneos, M. Vasilopoulou, S. Kennou, and U. Schwingenschlögl, "Vacancy formation in MoO3: Hybrid density functional theory and photoemission experiments," *J. Mater. Chem. C*, vol. 4, no. 40, pp. 9526–9531, 2016, doi: https://doi.org/10.1039/c6tc02571d.

[43] C. Y. Cheng, H. Kim, and N. C. Giebink, "Charged Polariton Luminescence from an Organic Semiconductor Microcavity," *ACS Photonics*, vol. 6, no. 2, pp. 308–313, 2019, doi: https://doi.org/10.1021/acsphotonics.8b01502.

[44] J. Ederth, A. Hoel, G. A. Niklasson, and C. G. Granqvist, "Small polaron formation in porous WO3-x nanoparticle films," *J. Appl. Phys.*, vol. 96, no. 10, pp. 5722–5726, 2004, doi: https://doi.org/10.1063/1.1804617.

[45] G. A. Niklasson, J. Klasson, and E. Olsson, "Polaron absorption in tungsten oxide nanoparticle aggregates*," Electrochim. Acta*, vol. 46, no. 13–14, pp. 1967–1971, 2001, doi: https://doi.org/10.1016/S0013-4686(01)00388-7.

[46] T. Koyama, A. Nakamura, and H. Kishida, "Microscopic Mobility of Polarons in

Chemically Doped Polythiophenes Measured by Employing Photoluminescence Spectroscopy," *ACS Photonics*, vol. 1, no. 8, pp. 655–661, 2014, doi: https://doi.org/10.1021/ph5000488.

[47] M. Dieterle, G. Weinberg, and G. Mestl, "Raman spectroscopy of molybdenum oxides - Part I. Structural characterization of oxygen defects in MoO3-x by DR UV/VIS, Raman spectroscopy and X-ray diffraction," *Phys. Chem. Chem. Phys*., vol. 4, no. 5, pp. 812–821, 2002, doi: https://doi.org/10.1039/b107012f.

[48] A. Gulino and G. Tabbì, "CdO thin films: A study of their electronic structure by electron spin resonance spectroscopy," Appl. Surf. Sci., vol. 245, no. 1–4, pp. 322–327, 2005, doi: https://doi.org/10.1016/j.apsusc.2004.10.026.

[49] R. J. Colton, A. M. Guzman, and J. W. Rabalais, "Photochromism and Electrochromism in Amorphous Transition Metal Oxide Films*," Acc. Chem. Res*., vol. 11, no. 4, pp. 170–176, Apr. 1978, doi: https://doi.org/10.1021/ar50124a008.

[50] J. Livage, "Small Polarons in Transition Metal Oxide Glasses", *in Glass … Current Issues,* Dordrecht: Springer Netherlands, 1985, pp. 408–418, doi: https://doi.org/10.1007/978-94-009-5107-5_34.

[51] M. Reticcioli, "Polarons in Transition-Metal Oxides," in *Comments Solid State Phys*, vol. 1, no. 4, W. Andreoni and S. Yip, Eds. Cham: Springer International Publishing, 1968, pp. 105–111, doi: https://doi.org/10.1007/978-3-319-50257-1_52-1.

[52] M. B. Johansson, A. Mattsson, S. E. Lindquist, G. A. Niklasson, and L. Österlund, "The Importance of Oxygen Vacancies in Nanocrystalline WO3-x Thin Films Prepared by DC Magnetron Sputtering for Achieving High Photoelectrochemical Efficiency," *J. Phys. Chem. C*, vol. 121, no. 13, pp. 7412–7420, 2017, doi: https://doi.org/10.1021/acs.jpcc.7b00856.

[53] I. G. Austin and N. F. Mott, "Polarons in crystalline and non-crystalline materials," *Adv. Phys.,* vol. 50, no. 7 SPEC., pp. 757–812, Nov. 2001, doi: https://doi.org/10.1080/00018730110103249.

[54] B. Henderson, "Optical Spectroscopy of Color Centers in Ionic Crystal," *in Spectroscopy of Solid-State Laser-Type Materials*, vol. 53, no. 9, Intergovernmental Panel on Climate Change, Ed. Boston, MA: Springer US, 1987, pp. 109–139, doi: https://doi.org/10.1007/978-1-4613-0899-7_3.

[55] S. I. Pekar and M. F. Deigen, “Quantum States and Optical Transitions of Electron in a Polaron and At a Color Center of a Crystal,” *Eksp. Teor. Fiz*, vol. 18, no. 6, pp. 481–486, 1948, [Online]. Available: http://archive.ujp.bitp.kiev.ua/files/journals/53/si/53SI17p.pdf.

[56] S. F. Wang, “Polaron model of electron-excess color centers,” *Phys. Rev.*, vol. 153, no. 3, pp. 939–947, 1967, doi: https://doi.org/10.1103/PhysRev.153.939.

[57] S. Krishnakumar and C. S. Menon, “Electrical and optical properties of molybdenum trioxide thin films,” *Bull. Mater. Sci.*, vol. 16, no. 3, pp. 187–191, 1993, doi: https://doi.org/10.1007/BF02745144.

[58] P. Spinelli et al., “Moly-poly solar cell: Industrial application of metal-oxide passivating contacts with a starting efficiency of 18.1%,” AIP Conf. Proc., vol. 1999, no. 1, p. 040021, 2018, doi: https://doi.org/10.1063/1.5049284.

[59] M. F. J. Vos, B. Macco, N. F. W. Thissen, A. A. Bol, and W. M. M. (Erwin) Kessels, “ Atomic layer deposition of molybdenum oxide from (N t Bu) 2 (NMe 2) 2 Mo and O 2 plasma,” *J. Vac. Sci. Technol. A Vacuum, Surfaces, Film.*, vol. 34, no. 1, p. 01A103, Jan. 2016, doi: https://doi.org/10.1116/1.4930161.

[60] S. Morawiec et al., “Experimental quantification of useful and parasitic absorption of light in plasmon-enhanced thin silicon films for solar cells application,” *Sci. Rep.*, vol. 6, 2016, doi: https://doi.org/10.1038/srep22481.

[61] E. Horynová *et al.*, “Optical characterization of low temperature amorphous MoOx, WOX, and VOx prepared by pulsed laser deposition,” *Thin Solid Films*, vol. 693, no. November 2019, 2020, doi: https://doi.org/10.1016/j.tsf.2019.137690.

[62] A. Gulino, G. G. Condorelli, and I. Fragalà, “Synthesis and spectroscopic characterization of MoO 3 thin films,” *J. Mater. Chem.*, vol. 6, no. 8, pp. 1335–1338, 1996, doi: https://doi.org/10.1039/JM9960601335.

[63] D. O. Scanlon, G. W. Watson, D. J. Payne, G. R. Atkinson, R. G. Egdell, and D. S. L. Law, “Theoretical and experimental study of the electronic structures of MoO 3 and MoO2,” *J. Phys. Chem. C,* vol. 114, no. 10, pp. 4636–4645, 2010, doi: https://doi.org/10.1021/jp9093172.

[64] S. K. Deb and J. A. Chopoorian, “Optical properties and color-center formation in thin films of molybdenum trioxide,” *J. Appl. Phys.*, vol. 37, no. 13, pp. 4818–4825, 1966, doi: https://doi.org/10.1063/1.1708145.

[65] P. A. Spevack and N. S. McIntyre, “A Raman and XPS investigation of supported molybdenum oxide thin films. 2. Reactions with hydrogen sulfide,” *J. Phys. Chem*., vol. 97, no. 42, pp. 11031–11036, 1993, doi: https://doi.org/10.1021/j100144a021.

[66] K. Kanai *et a*l., “Electronic structure of anode interface with molybdenum oxide buffer layer,” *Org. Electron.*, vol. 11, no. 2, pp. 188–194, Feb. 2010, doi: https://doi.org/10.1016/j.orgel.2009.10.013.

[67] R. K. Biswas, P. Khan, S. Mukherjee, A. K. Mukhopadhyay, J. Ghosh, and K. Muraleedharan, “Study of short range structure of amorphous Silica from PDF using Ag radiation in laboratory XRD system, RAMAN and NEXAFS,” *J. Non. Cryst. Solids*, vol. 488, no. March, pp. 1–9, 2018, doi: https://doi.org/10.1016/j.jnoncrysol.2018.02.037.

[68] V. Jadkar et al., “Synthesis of orthorhombic-molybdenum trioxide (α-MoO3) thin films by hot wire-CVD and investigations of its humidity sensing properties,” *J. Mater. Sci. Mater. Electron*., vol. 28, no. 21, pp. 15790–15796, 2017, doi: https://doi.org/10.1007/s10854-017-7473-6.

[69] J. Tauc, R. Grigorovici, and A. Vancu, “Optical Properties and Electronic Structure of Amorphous Germanium,” *Phys. Status Solidi*, vol. 15, no. 2, pp. 627–637, 1966, doi: https://doi.org/10.1002/pssb.19660150224.

[70] J. J. Thevaril and S. K. O’Leary, “A dimensionless joint density of states formalism for the quantitative characterization of the optical response of hydrogenated amorphous silicon,” *J. Appl. Phys*., vol. 107, no. 8, 2010, doi: https://doi.org/10.1063/1.3385434.

[71] J. A. Guerra, A. Tejada, J. A. Töfflinger, R. Grieseler, and L. Korte, “Band-fluctuations model for the fundamental absorption of crystalline and amorphous semiconductors: A dimensionless joint density of states analysis,” *J. Phys. D. Appl. Phys*., vol. 52, no. 10, 2019, doi: https://doi.org/10.1088/1361-6463/aaf963.

[72] J. A. Guerra *et al.,* “The Urbach focus and optical properties of amorphous hydrogenated SiC thin films,” *J. Phys. D. Appl. Phys*., vol. 49, no. 19, 2016, doi: https://doi.org/10.1088/0022-3727/49/19/195102.

[73] D. Zu *et al.,* “Oxygen-deficient metal oxides: Synthesis routes and applications in energy and environment,” *Nano Res*., vol. 12, no. 9, pp. 2150–2163, 2019, doi: https://doi.org/10.1007/s12274-019-2377-9.

[74] P. Procel, G. Yang, O. Isabella, and M. Zeman, “Theoretical evaluation of contact stack for high efficiency IBC-SHJ solar cells,” *Sol. Energy Mater. Sol. Cells*, vol. 186, pp. 66–77, 2018, doi: https://doi.org/10.1016/j.solmat.2018.06.021.

[75] P. Procel, P. Löper, F. Crupi, C. Ballif, and A. Ingenito, “Numerical simulations of hole carrier selective contacts in p-type c-Si solar cells,” *Sol. Energy Mater. Sol. Cells*, vol. 200, 2019, doi: https://doi.org/10.1016/j.solmat.2019.109937.

5 Density of States in Titanium Oxide

The application of titanium oxide in the photovoltaic field is gaining traction as this material can be deployed in doping-free heterojunction solar cells in the role of electron selective contact. For modeling-based optimization of such contact, knowledge of the titanium oxide defect density of states is crucial. In this chapter, we report a method to extract the defect density through nondestructive optical measures, including the contribution given by small polaron optical transitions. The presence of defects related to oxygen-vacancy and of polaron is supported by the results of optical characterizations along with the evaluation of previous observations resulting in a defect band fixed at 1 eV below the conduction band edge of the oxide.

5.1 Introduction

As already mentioned in the previous chapters, the c-Si heterojunction technology (HJT) represents an interesting innovation leading to solar cells with record efficiency over 26% [1, 2] and at industrial level of 24.63% [3]. Such results were achieved thanks to the excellent passivation properties of the a-Si:H [4]; despite these achievements, exploiting a-Si:H introduces some drawbacks due to the large presence of defects and parasitic absorption [5], moreover, the further optimization of the hydrogenated amorphous silicon layer is challenging [6]. Therefore, other materials such as the transition metal oxides (TMOs) are currently investigated to replace a-Si:H in HJT and implement passivating carrier selective contacts (CSC) [7]. These contacts are typically made of TMOs like TiO_2, ZnO and TaO (for the electron selective contact) and can be deposited reliably with a variety of different techniques such as atomic layer deposition, atmospheric pressure chemical vapor deposition, physical vapor deposition and wet chemical methods [8]. Examples of HJT cells implementing TMOs selective contacts have be reported [6, 9-11], reaching efficiency up to 23.5% [12]. For the electron selective contact, titanium dioxide in its sub-stoichiometric form (TiO_x) ($x < 2$) represents a suitable choice. Indeed, such material presents at the interface with the n-type silicon a large offset in the valence band, forming a barrier that blocks the hole transport; at the same time, it presents a good alignment of the conduction bands presenting a small offset, allowing the electrons to pass through the selective contact [11, 13]. The formation of the sub-stoichiometric TiO_x compound is essential to achieve adequate selectivity and passivation. The presence of oxygen vacancies is necessary for achieving a low contact resistivity; in fact, the film conductivity rise as oxygen vacancies

increment provides *n*-type doping [14]. TiO_x is one of the most employed TMOs as an electron selective contact, with several studies highlighting its characteristics, implementing them in HJT [15-17] and reaching efficiency over 22% [18]. Although this transition metal oxide was previously studied and characterized for various electronic devices, its performances in heterojunction solar cells are currently under a process of optimization. Thus, gaining insight into the role of the bandgap defects related to the oxygen vacancies is of particular importance [19, 20], since these defect states actively contribute to the carrier transport and simulations of TMOs-based cells [21].

Indeed, lack of information on the defect density of states of TMO layer may compromise any optimization of such solar cell architecture leading to sub-optimal DC characteristics with S-shaped J–V curves [22], with a considerable decrease in the cell electrical performances. However, a quantitative study on the defect density of states in the bandgap of the TiOx for solar cells devices has not yet proposed. For this reason, expanding the knowledge behind the formation mechanisms of the S-shaped current is essential in order to avoid such behavior and further the dissemination of the TMO-based heterojunction technology.

As reported on Chapter 4, the defect density of states of a thin film can be extrapolated from its absorption coefficient and by evaluating the optical transitions between available states and the conduction band. For this purpose, an absolute PDS setup has been used to measure the optical transmissivity values, reflectance, and absorptance in a wide spectral range [23, 24] simultaneously; such technique has been extensively used to get information on the defectivity of semiconductors [23–25]. Furthermore, the contribution to the absorption coefficient due to the small polaron has also been considered; such technique was previously used for characterizing the sub-gap defect density in transition metal oxides such as molybdenum oxide [26, 27].

5.2 Methodology

5.2.1 Density of states evaluation

We have fitted the PDS absorption spectra, *α(hv)*, by using the so-called *one-electron approximation* [24] expressed in the Chapter 4 (see Eq.s (4.1)-(4.4)). The densities of states of the valence and conduction band are respectively N_V equal to $7.09 \cdot 10^{19}$ $cm^{-3}eV^{-3/2}$, and N_C equal to $6.77 \cdot 10^{20}$ $cm^{-3}eV^{-3/2.}$ These values have been calculated considering the values of effective masses for electrons and holes reported in [28].

The constant *C* of Eq. (4.1) was evaluated for each spectrum to obtain the quantitative DOS parameters by calculating (4.1) at 4 eV. It should be noted that, at this energy, the optical transition from the valence to the conduction band give the most prominent contribution to the absorption; therefore, only this contribution is considered for the constant calculation. Depending on the deposition conditions, the resulting *C* values lay in the range $(1.11\text{-}2.02)\times10^{-34}$ $cm^5 \cdot eV^2$ and are listed in Table 5.1.

Table 5.1 *Constant C values for different deposition conditions*

PO_2 (mbar)	Temp (°C)	C ($cm^5 \cdot eV^2$)
1×10^{-3}	Amb.	1.31E-34
	200°C	2.02E-34
1×10^{-2}	Amb.	1.13E-34
	200°C	1.37E-34
2×10^{-2}	Amb.	1.11E-34
	200°C	1.18E-34

5.2.2 Experimental details

Layers of titanium oxide were deposited by Pulsed Laser Deposition (PLD) technique on quartz substrates from a titanium dioxide (Balzers, 99.5%) precursor. The main depositions were conducted at ambient temperature and at 200 °C under three different oxygen pressures of 2×10^{-2}, 1×10^{-2} and 1×10^{-3} mbar. Three additional samples were deposited in vacuum at room temperature and at 200 °C and at 400 °C with a PO_2 of 1×10^{-2} mbar.

The layers thicknesses were evaluated using spectroscopic ellipsometry (SE) with a single Cody-Lorentz oscillator [29]. The mean thickness resulted in 155 nm with a small variation among the samples deposited in the oxidating ambiance at room temperature and at 200 °C, whereas the sample deposited at 400 °C resulted in a thinner film (35 nm) and the samples deposited in vacuum presented a thickness of 113 nm (at room temperature) and of 95 nm (at 200 °C).

XPS was used to identify the elements present onto the surface and for the determination of the relative composition. Samples were excited with Al-K_α source ($h\nu$=1486.6 eV). The morphological evaluation of the TiO_x layers has been investigated by a Raman spectroscopy (λ=514 nm). The absorption coefficient of the samples was extracted from a photothermal deflection spectroscopy (PDS) setup [30, 31], by measuring the

deflection of a He-Ne laser beam tangent to surface of the film.

5.3 Results and discussion

5.3.1 Chemical and structural characterization

The composition of the deposited samples was analyzed through X-ray photoemission spectroscopy (XPS). The spectra shown in Figure 5.1 are related to the samples deposited at ambient temperature with a partial pressure of oxygen of 1×10^{-3} mbar (Figure 5.1a) and 2×10^{-2} mbar (Figure 5.1b); results highlight for both samples the presence of a doublet with the Ti $2p_{3/2}$ (458.6 eV) and Ti $2p_{1/2}$ (464.4 eV): these components are associated with the Ti^{4+} oxidation state [32, 33], which correspond to the stoichiometric TiO_2 compound. The oxygen region of the 1s binding is then deconvoluted in Figure 5.2a (for the sample deposited at PO_2=1×10^{-3} mbar) and in Figure 5.2b (for the sample deposited at PO_2=2×10^{-2} mbar), showing the presence of two peaks: one at 530.0 eV, corresponding to the Ti^{4+} oxidation state, while the other one at 531.4 eV corresponds to the Ti^{3+} oxidation state introduced by the oxygen vacancies [33], thus confirming that both the samples are sub-stochiometric.

The morphology of the deposited oxide was analyzed by evaluating the Raman spectrum. The results are highlighted in Figure 5.3; in particular, Figure 5.3a shows the Raman spectra for the samples deposited with PO_2 equal to 1×10^{-3} mbar and 2×10^{-2} mbar at ambient temperature and 200°C. Similar behavior was measured for the samples deposited with PO_2=1×10^{-2} mbar; besides, it is not reported here for the sake of brevity. It can be observed that there are no sharp peaks in the spectra, confirming that the material is amorphous even when deposited at 200°C. Indeed, a higher temperature is required to start crystallization [34-38]. For comparison purposes, Figure 5.3b shows the Raman spectrum of a TiO_x sample deposited at 400°C with PO_2=1×10^{-2} mbar in which the presence of sharp peaks (145, 198, 399, 516, 640 cm^{-1}) is highlighted; such peaks are correlated to the anatase crystalline phase [39, 40].

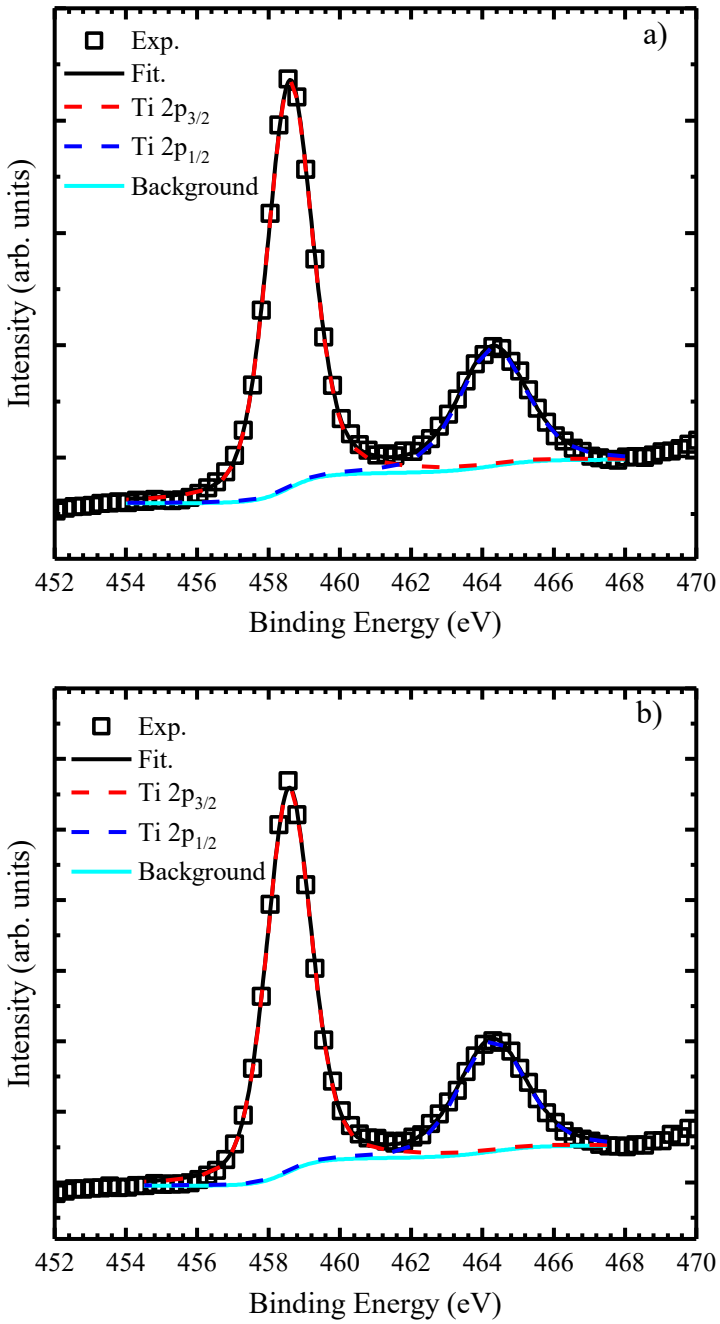

Figure 5.1 *Ti 2p binding region curve fitting of samples deposited with PO_2 of: a) 1×10^{-3} mbar, b) 2×10^{-2} mbar.*

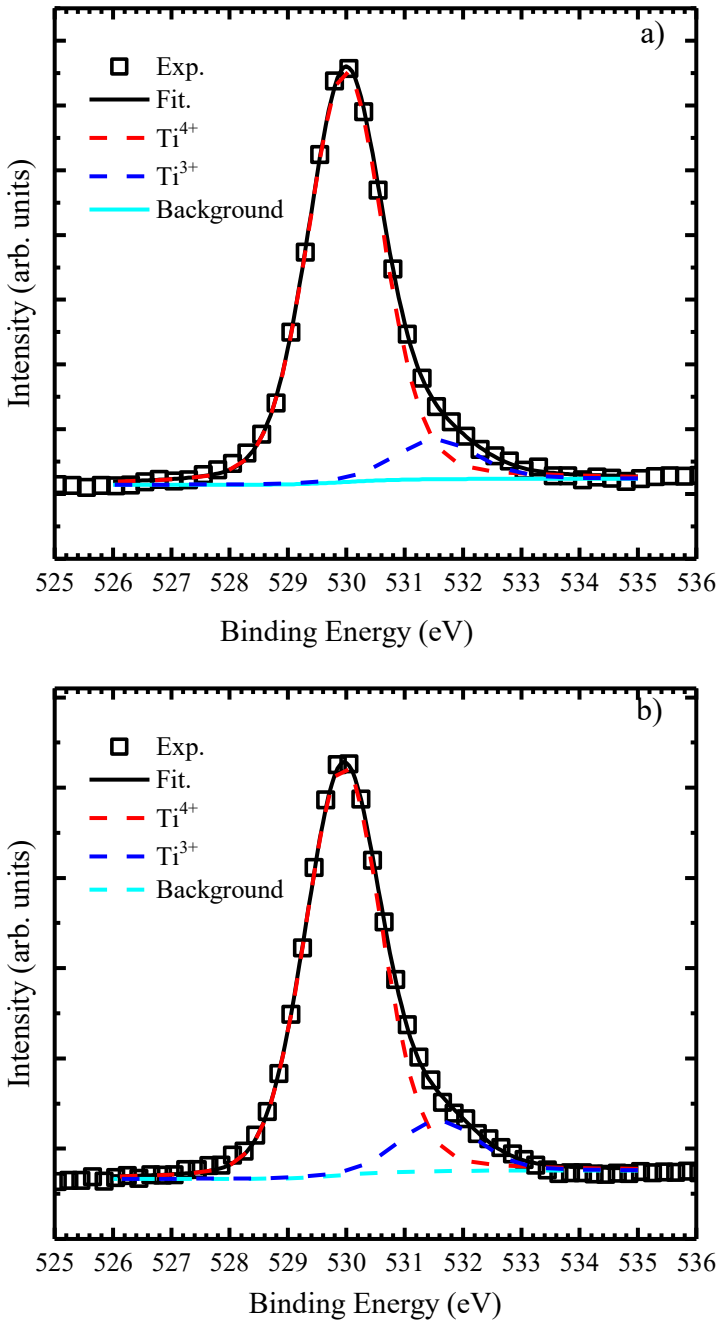

Figure 5.2 *O 1s binding region curve fitting of samples deposited with PO_2 of: a) 1×10^{-3} mbar, b) 2×10^{-2} mbar.*

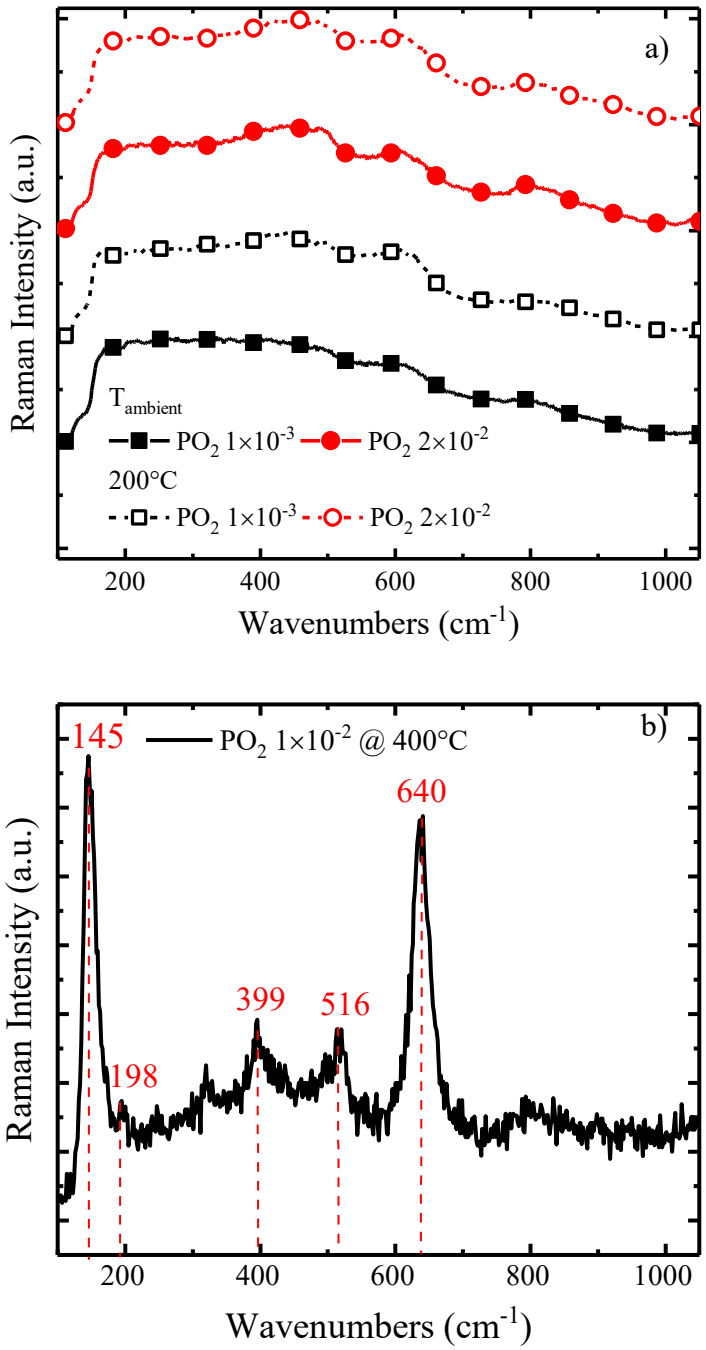

Figure 5.3 *a) Raman spectra of the deposited TiO_x samples for different PO_2 (in mbar) and deposition temperature (mean thickness of 155 nm); b) Raman spectrum of the TiO_x sample deposited at 400°C with $PO_2=1\times10^{-2}$ mbar (thickness of 35 nm).*

5.3.2 Optical characterization

The optical absorption spectra of the TiO_x samples are shown in Figure 5.4. We report for reference the spectra of samples deposited in a vacuum without introducing oxygen in the PLD chamber at ambient temperature and 200 °C. The spectra of these two samples are similar, expressing an almost constant value ($\alpha\approx10^5$ cm^{-1}) throughout the whole measurement range. It should be noted that the deposition of the sample in the absence of O_2 led to very different samples with opaque-black coloration and a high absorption

spectrum (Figure 5.4); such behavior is typical of the *black-TiO_2* [41] and is caused by a large defect concentration due to the oxygen vacancies.

For the other samples obtained adding O_2 in the deposition chamber, the absorption in each spectrum grows from lower energies to a small peak in the region located between 1.4 eV and 1.8 eV; then, except for the samples with PO_2=1×10^{-2} mbar, it decreases to a lower value at 3 eV and then rises again exponentially. These absorption characterizations are in good accordance with the literature [42]. It can be noted that from 1 eV to 3 eV, the absorption spectra of the samples deposited at ambient temperature are slightly higher than the ones deposited with the same PO_2 and at 200 °C. Remarkably, this effect is more evident for the sample deposited with PO_2=1×10^{-3} mbar at 200 °C, which exhibits significantly larger absorption than the sample deposited for the same oxygen pressure at ambient temperature. This behavior can be attributed to a less defective lattice than the materials deposited at ambient temperature, giving a minor oxygen vacancy content which leads to a lower absorption coefficient. A different behavior is present for the higher energy, from 3 eV to 4 eV; in this case, the absorption coefficient of the samples deposited at 200 °C is slightly lower for the samples deposited with the same pressure at ambient temperature. Finally, a general trend can be highlighted as the samples deposited with higher oxygen pressure exhibit a lower absorption coefficient. A minor content of oxygen vacancies in the material lattice can explain this behavior; indeed, the higher PO_2 improves the stoichiometric ratio of the compound [43], reducing the defects due to the oxygen vacancies, thus reducing the absorption.

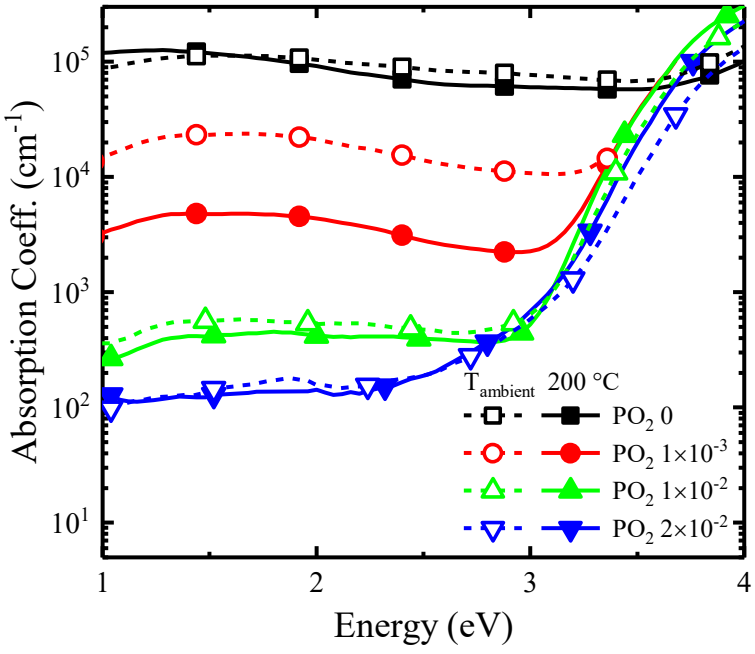

Figure 5.4 *Absorption spectra for TiO_x samples deposited at different deposition temperatures and*

pressures (mbar)

The optical band gap, E_{opt}, of the sample was evaluated by Tauc's law [44] and are summarized in Table 5.2. Resulting values lay within the range from 3.3 to 3.4 eV. The results show a small difference between the optical band gap values except for the samples deposited with the highest oxygen pressure (PO_2=2×10^{-2} mbar), which are slightly higher than the other samples.

The Urbach energy, E_U, of the samples was evaluated using Urbach's relation and the results are reported in Table 5.2. It can be observed that, for the films deposited with the same PO_2, the samples grown at ambient temperature are characterized by a higher E_U respect to the ones deposited at 200 °C. The increase in Urbach's energy and the narrowing of the optical gap can be related to the increased defect density induced by the oxygen vacancies in the oxide film [45, 46].

Table 5.2 *Tauc gap and Urbach energy evaluation*

PO_2 (mbar)	Temp (°C)	Tauc gap, E_T (eV)	Urbach Energy, E_U (meV)
1×10^{-3}	Amb.	3.31	185
	200 °C	3.31	143
1×10^{-2}	Amb.	3.32	124
	200 °C	3.30	110
2×10^{-2}	Amb.	3.38	142
	200 °C	3.34	131

Figure 5.5 presents an example of the absorption fit for the sample deposited with PO_2=1×10^{-3} mbar at 200 °C. The absorption spectrum is composed of many elements representing the contribution due to the optical transitions from the valence to the conduction band ($T_{VB\text{-}CB}$); from valence band tail to conduction band tail ($T_{VBT\text{-}CBT}$); from the valence band tail to the conduction band ($T_{VBT\text{-}CB}$); from the valence band to the conduction band tail ($T_{VB\text{-}CBT}$); from inter-band defects to the conduction band ($T_{D\text{-}CB}$); from defects in the bandgap to the conduction band tail ($T_{D\text{-}CBT}$) and finally to the transition due to the polaron ($T_{Polaron}$).

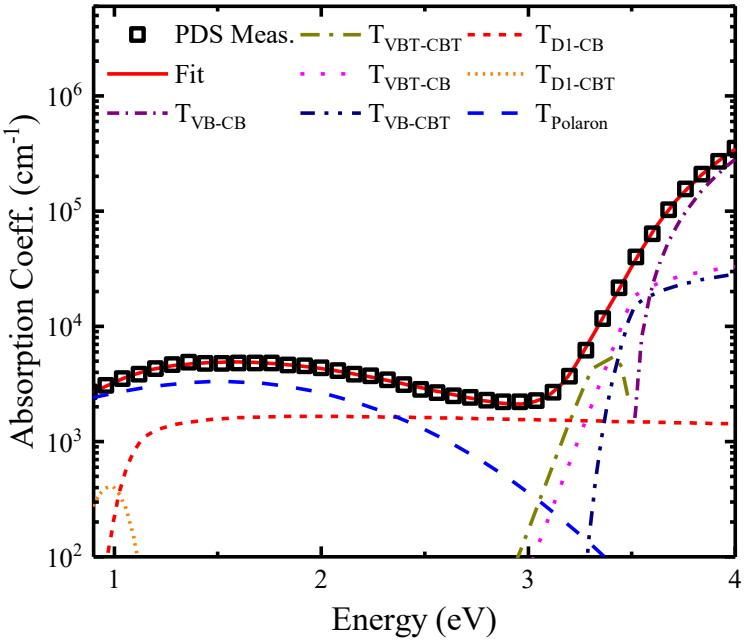

Figure 5.5 *Absorption spectrum deconvolution for the TiO_x sample deposited at PO_2=1×10^{-3} at 200°C*

The parameters obtained by the deconvolution of the absorption spectra are listed in Table 5.3 and are related to the samples of titanium oxide deposited with PO_2 of 1×10^{-3}, 1×10^{-2} and 2×10^{-2} mbar at ambient temperature and 200°C.

Table 5.3 *The density of states and small polaron parameters for different deposition conditions*

PO_2 (mbar)	Temp (°C)	E_{0V} (meV)	E_{0C} (meV)	A_D (ev^{-1}cm^{-3})	E_D (eV)	W (eV)	A_P (ev^{-1}cm^{-3})	E_P (eV)	E_{op} (meV)
1×10^{-3}	Amb.	136	609	4.96×10^{16}	1.02	0.08	5.17×10^{4}	0.94	86.41
	200°C	128	628	1.54×10^{16}	1.05	0.06	4.58×10^{6}	0.93	117.10
1×10^{-2}	Amb.	114	585	7.33×10^{15}	1.05	0.08	3.05×10^{2}	0.91	105.60
	200°C	104	568	6.37×10^{15}	1.00	0.08	1.19×10^{2}	0.93	110.11
2×10^{-2}	Amb.	136	519	1.34×10^{15}	1.05	0.05	1.23×10^{2}	0.94	112.37
	200°C	101	602	1.12×10^{15}	1.08	0.08	1.08×10^{2}	0.94	120.03

It is worth noting that the slope of the valence band (E_{0V}) of the samples deposited at ambient temperature is always higher than the samples deposited at the same oxygen pressure at 200 °C; a different trend is reported for the slope of the conduction band (E_{0C}) which for the samples deposited at ambient temperature is lower than the samples deposited with the same PO_2 at 200 °C. For the defects distribution in the bandgap, the energy position of the defects (E_D) oscillates around a mean value of 1 eV below the conduction band edge with standard deviations varying from 50 to 80 meV. The energy position agrees with previous observations reporting localized oxygen vacancy in TiO_x at about 1 eV below the

conduction band [47-49]. The defects area (A_D) shows a significant trend in the function of both the deposition temperature and pressure; as shown in Figure 5.6a, is observable that the rise of the deposition temperature at 200 °C reduces the A_D at parity of PO_2. This effect is more evident for the sample deposited at 1×10^{-3} mbar at T_{amb}, which presents a defects area roughly three times higher than the samples deposited at 200 °C.

Moreover, Figure 5.6a shows a descending trend in the defects area for increasing oxygen pressure for both deposition temperatures. This study highlights that the deposition of the oxides in an atmosphere with a high oxygen content reduces the formation of oxygen vacancies; furthermore, this effect is enhanced by using a high deposition temperature. Figure 5.6b also shows the data extrapolated from the fitting relative to the pre-exponential factor of the polaron absorption (A_p), which presents a similar trend to the area of the defects with a descending A_p for increasing deposition oxygen pressure and temperature. Finally, E_P resulted unchanged by the deposition conditions, with mean values of 0.93 eV; E_{op}, instead, fluctuates between 86 and 120 meV with a mean value of 113.4 eV.

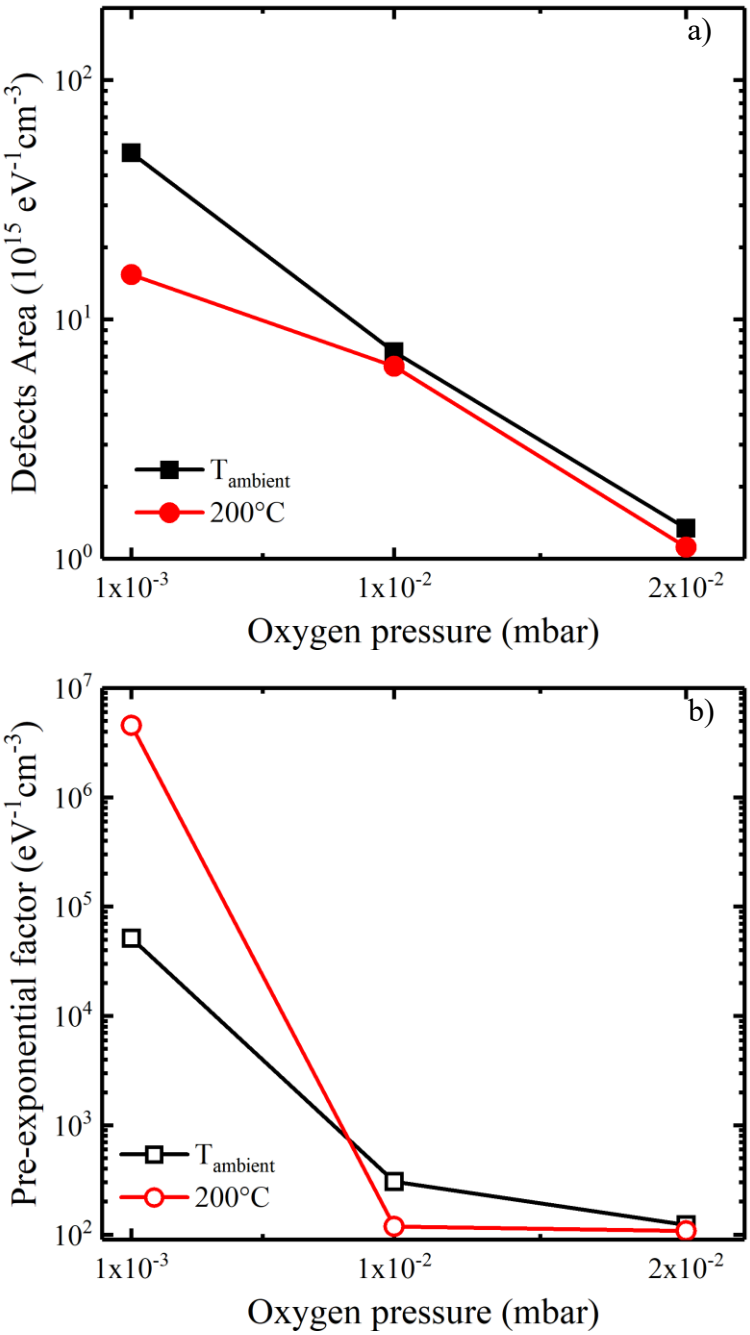

Figure 5.6 *Defects area of the distributions centered 1 eV below the conduction band (a) and pre-exponential factor of the polaron absorption (b) in function of the oxygen deposition pressure at ambient temperature and 200 °C.*

5.4 Conclusions

In this chapter, the analysis and characterization of amorphous titanium oxide have been performed. For this purpose, thin films of sub-stoichiometric amorphous TiO_x were deposited by pulsed laser deposition with different deposition conditions (in terms of oxygen pressure and substrate temperature). Optical spectra displayed a pronounced absorption peak in the near-infrared range associated with a contribution given by small polaron, energy positions of which remained constant after the post-deposition thermal treatment. In contrast, the peak values decreased with rising pressure of oxygen during deposition. The defects area shows a similar trend in the function of both the deposition temperature and pressure. This effect is more evident for the sample deposited at 1×10^{-3} mbar at T_{amb}, which presents a defects area roughly three times higher than the samples deposited at 200 °C. The explanation for this phenomenon can be found in the binding between the polaron formation and the defect formation, as during the annealing, oxygen deficiencies create positively charged oxygen vacancies with accompanying charge-compensating electrons. From the fitting of the experimental absorption spectra, through the evaluation of optical transition over the bandgap and from the polaron theory, it was found that the inter-band defect density lays around 1 eV below the edge of the conduction band with amplitude decreasing with increasing temperature and oxygen pressure. The polaron binding energy resulted approximately in 0.93 eV while the longitudinal-optical phonon energy in 85 meV. The exponential valence tail value slope resulted in about five times lower than the conduction tail and showed no change among the samples made with different deposition conditions. From this analysis, it was possible to obtain parameters functional to simulate TiO_x appropriately in advanced device simulators; the method proposed can be applied to other materials exhibiting similar absorption coefficients, such as transition metal oxides. By using the results from the small polaron theory, it was possible to improve an existing approach in the defects density characterization. This approach and the data are of great importance in the field of simulation of solar cells. Information and analysis on the defects DOS are still missing for many materials and without this data, any simulation of titanium dioxide cell may not be enough accurate or physically feasible.

References

[1] M. Green, E. Dunlop, J. Hohl-Ebinger, M. Yoshita, N. Kopidakis, and X. Hao, "Solar cell efficiency tables (version 57)," *Prog. Photovoltaics Res. Appl.*, vol. 29, no. 1, pp. 3–15, 2021, doi: https://doi.org/10.1002/pip.3371.

[2] K. Yoshikawa *et al.*, "Silicon heterojunction solar cell with interdigitated back contacts for a photoconversion efficiency over 26%," *Nat. Energy*, vol. 2, no. 5, May 2017, doi: https://doi.org/10.1038/nenergy.2017.32.

[3] Enel Green Power, "New efficiency record for the innovative solar cells produced by 3SUN based on heterojunction technology." https://www.enelgreenpower.com/media/news/2020/02/3sun-solar-cell-bifacials-efficiency-record (accessed Mar. 11, 2021).

[4] A. McEvoy, T. Markvart, and L. Castaner, Practical Handbook of Photovoltaics. 2012, doi: https://doi.org/10.1016/C2011-0-05723-X.

[5] Z. C. Holman *et al.*, "Current losses at the front of silicon heterojunction solar cells," *IEEE J. Photovoltaics*, vol. 2, no. 1, pp. 7–15, Jan. 2012, doi: https://doi.org/10.1109/JPHOTOV.2011.2174967.

[6] J. Bullock *et al.*, "Efficient silicon solar cells with dopant-free asymmetric heterocontacts," *Nat. Energy*, vol. 1, no. 3, 2016, doi: https://doi.org/10.1038/nenergy.2015.31.

[7] J. Melskens, B. W. H. Van De Loo, B. Macco, L. E. Black, S. Smit, and W. M. M. Kessels, "Passivating Contacts for Crystalline Silicon Solar Cells: From Concepts and Materials to Prospects," *IEEE J. Photovoltaics*, vol. 8, no. 2, pp. 373–388, 2018, doi: https://doi.org/10.1109/JPHOTOV.2018.2797106.

[8] K. Gesheva *et al.*, "Technologies for deposition of transition metal oxide thin films: Application as functional layers in 'smart windows' and photocatalytic systems," in *Journal of Physics: Conference Series*, 2016, vol. 682, no. 1, doi: https://doi.org/10.1088/1742-6596/682/1/012011.

[9] M. Mews, A. Lemaire, and L. Korte, "Sputtered Tungsten Oxide as Hole Contact for Silicon Heterojunction Solar Cells," *IEEE J. Photovoltaics*, vol. 7, no. 5, pp. 1209–1215, 2017, doi: https://doi.org/10.1109/JPHOTOV.2017.2714193.

[10] K. Mallem *et al.*, "Molybdenum oxide: A superior hole extraction layer for

replacing p-type hydrogenated amorphous silicon with high efficiency heterojunction Si solar cells," *Mater. Res. Bull.*, vol. 110, pp. 90–96, Feb. 2019, doi: https://doi.org/10.1016/j.materresbull.2018.10.018.

[11] C. Yu, S. Xu, J. Yao, and S. Han, "Recent advances in and new perspectives on crystalline silicon solar cells with carrier-selective passivation contacts," *Crystals,* vol. 8, no. 11, 2018, doi: https://doi.org/10.3390/cryst8110430.

[12] J. Dréon *et al.*, "23.5%-Efficient Silicon Heterojunction Silicon Solar Cell Using Molybdenum Oxide As Hole-Selective Contact," *Nano Energy*, vol. 70, 2020, doi: https://doi.org/10.1016/j.nanoen.2020.104495.

[13] M. Perego, G. Seguini, G. Scarel, M. Fanciulli, and F. Wallrapp, "Energy band alignment at Ti O2 Si interface with various interlayers," *J. Appl. Phys.*, vol. 103, no. 4, 2008, doi: https://doi.org/10.1063/1.2885109.

[14] J. Yang, L. Li, W. Li, and L. Mao, "Formation mechanism of conduction path in titanium dioxide with Ti-interstitials-doped: Car-Parrinello molecular dynamics," in *AIP Conference Proceedings*, 2017, vol. 1794, doi: https://doi.org/10.1063/1.4971906.

[15] X. Yang, Q. Bi, H. Ali, K. Davis, W. V. Schoenfeld, and K. Weber, "High-Performance TiO2-Based Electron-Selective Contacts for Crystalline Silicon Solar Cells," *Adv. Mater.*, vol. 28, no. 28, pp. 5891–5897, 2016, doi: https://doi.org/10.1002/adma.201600926.

[16] K. A. Nagamatsu et al., "Titanium dioxide/silicon hole-blocking selective contact to enable double-heterojunction crystalline silicon-based solar cell," *Appl. Phys. Lett.*, vol. 106, no. 12, 2015, doi: https://doi.org/10.1063/1.4916540.

[17] J. Cho *et al.*, "Passivating electron-selective contacts for silicon solar cells based on an a-Si:H/TiOx stack and a low work function metal," *Prog. Photovoltaics Res.* Appl., vol. 26, no. 10, pp. 835–845, 2018, doi: https://doi.org/10.1002/pip.3023.

[18] X. Yang, K. Weber, Z. Hameiri, and S. De Wolf, "Industrially feasible, dopant-free, carrier-selective contacts for high-efficiency silicon solar cells," *Prog. Photovoltaics Res. Appl.*, vol. 25, no. 11, pp. 896–904, 2017, doi: https://doi.org/10.1002/pip.2901.

[19] Y. Li *et al.*, "Defective TiO2 with high photoconductive gain for efficient and stable planar heterojunction perovskite solar cells," *Nat. Commun.*, vol. 7, 2016, doi:

https://doi.org/10.1038/ncomms12446.

[20] A. Lewis *et al*., "In-depth analysis of defects in TiO2 compact electron transport layers and impact on performance and hysteresis of planar perovskite devices at low light," *Sol. Energy Mater. Sol. Cells*, vol. 209, 2020, doi: https://doi.org/10.1016/j.solmat.2020.110448.

[21] C. Messmer, M. Bivour, J. Schon, S. W. Glunz, and M. Hermle, "Numerical Simulation of Silicon Heterojunction Solar Cells Featuring Metal Oxides as Carrier-Selective Contacts," *IEEE J. Photovoltaics*, vol. 8, no. 2, pp. 456–464, 2018, doi: https://doi.org/10.1109/JPHOTOV.2018.2793762.

[22] C. Messmer, M. Bivour, J. Schön, and M. Hermle, "Requirements for efficient hole extraction in transition metal oxide-based silicon heterojunction solar cells," *J. Appl. Phys*., vol. 124, no. 8, 2018, doi: https://doi.org/10.1063/1.5045250.

[23] M. Vaněček, J. Kočka, J. Stuchlík, Z. Kožíšek, O. Štika, and A. Tříska, "Density of the gap states in undoped and doped glow discharge a-Si:H," *Sol. Energy Mater*., vol. 8, no. 4, pp. 411–423, 1983, doi: https://doi.org/10.1016/0165-1633(83)90006-0.

[24] H. Fritzsche, J. Kočka, M. Vaněček, and A. Tříska, " ENERGY AND DENSITY OF GAP STATES IN a-Si:H ," in *Amorphous Silicon and Related Materials*, H. Frtitzsche, Ed. WORLD SCIENTIFIC, 1989, pp. 297–327, doi: https://doi.org/10.1142/9789814434157_0011.

[25] S. Morawiec *et al*., "Experimental quantification of useful and parasitic absorption of light in plasmon-enhanced thin silicon films for solar cells application," *Sci. Rep*., vol. 6, 2016, doi: https://doi.org/10.1038/srep22481.

[26] D. Scirè, P. Procel, A. Gulino, O. Isabella, M. Zeman, and I. Crupi, "Sub-gap defect density characterization of molybdenum oxide: An annealing study for solar cell applications," *Nano Res*., vol. 13, no. 12, pp. 3416–3424, 2020, doi: https://doi.org/10.1007/s12274-020-3029-9.

[27] D. Scirè, R. Macaluso, M. Mosca, S. Mirabella, A. Gulino, O. Isabella, M. Zeman, and I. Crupi, "Characterization of the defect density states in MoOx for c-Si solar cell applications," *Solid. State. Electron.*, vol. 185, p. 108135, Nov. 2021, doi: https://doi.org/10.1016/j.sse.2021.108135.

[28] C. Kormann, D. W. Bahnemann, and M. R. Hoffmann, “Preparation and characterization of quantum-size titanium dioxide,” *J. Phys. Chem.*, vol. 92, no. 18, pp. 5196–5201, 1988, doi: https://doi.org/10.1021/j100329a027.

[29] H. Mati, C. Pongpan, and L. Pichet, “A spectroscopic ellipsometry study of TiO2 thin films prepared by dc reactive magnetron sputtering: Annealing temperature effect,” *Chinese Phys. Lett.*, vol. 24, no. 6, pp. 1505–1508, 2007, doi: https://doi.org/10.1088/0256-307X/24/6/021.

[30] Z. Remes, R. Vasudevan, K. Jarolimek, A. H. M. Smets, and M. Zeman, “The optical spectra of a-Si:H and a-SiC:H thin films measured by the absolute photothermal deflection spectroscopy (PDS),” *Solid State Phenom.*, vol. 213, pp. 19–28, 2014, doi: https://doi.org/10.4028/www.scientific.net/SSP.213.19.

[31] M. Singh *et al.*, “Optical characterization of poly-SiOx and poly-SiCx carrier-selective passivating contacts,” *Sol. Energy Mater. Sol. Cells*, vol. 210, 2020, doi: https://doi.org/10.1016/j.solmat.2020.110507.

[32] B. Bharti, S. Kumar, H. N. Lee, and R. Kumar, “Formation of oxygen vacancies and Ti3+ state in TiO2 thin film and enhanced optical properties by air plasma treatment,” *Sci. Rep.*, vol. 6, 2016, doi: https://doi.org/10.1038/srep32355.

[33] R. Sanjinés, H. Tang, H. Berger, F. Gozzo, G. Margaritondo, and F. Lévy, “Electronic structure of anatase TiO2 oxide,” *J. Appl. Phys.*, vol. 75, no. 6, pp. 2945–2951, 1994, doi: https://doi.org/10.1063/1.356190.

[34] A. A. Akl, H. Kamal, and K. Abdel-Hady, “Fabrication and characterization of sputtered titanium dioxide films,” *Appl. Surf. Sci.*, vol. 252, no. 24, pp. 8651–8656, 2006, doi: https://doi.org/10.1016/j.apsusc.2005.12.001.

[35] J. Y. Zhang, I. W. Boyd, B. J. O’Sullivan, P. K. Hurley, P. V. Kelly, and J. P. Sénateur, “Nanocrystalline TiO2 films studied by optical, XRD and FTIR spectroscopy,” J. *Non. Cryst. Solids*, vol. 303, no. 1, pp. 134–138, 2002, doi: https://doi.org/10.1016/S0022-3093(02)00973-0.

[36] K. Katagiri, T. Suzuki, H. Muto, M. Sakai, and A. Matsuda, “Low temperature crystallization of TiO2 in layer-by-layer assembled thin films formed from water-soluble Ti-complex and polycations,” *Colloids Surfaces A Physicochem. Eng. Asp.*, vol. 321, no. 1–3, pp. 233–237, 2008, doi: https://doi.org/10.1016/j.colsurfa.2007.11.028.

[37] A. Matthews, “The crystallization of anatase and rutile from amorphous titanium dioxide under hydrothermal conditions,” *Am. Mineral.*, vol. 61, pp. 419–424, 1976, [Online]. Available: http://www.minsocam.org/ammin/AM61/AM61_419.pdf.

[38] A. S. Bakri *et al.*, “Effect of annealing temperature of titanium dioxide thin films on structural and electrical properties,” in *AIP Conference Proceedings*, 2017, vol. 1788, doi: https://doi.org/10.1063/1.4968283.

[39] Q. Zhang *et al.*, “Anodic oxidation synthesis of one-dimensional TiO2 nanostructures for photocatalytic and field emission properties,” *Journal of Nanomaterials*, vol. 2014. 2014, doi: https://doi.org/10.1155/2014/831752.

[40] L. Stagi, C. M. Carbonaro, R. Corpino, D. Chiriu, and P. C. Ricci, “Light induced TiO 2 phase transformation: Correlation with luminescent surface defects,” *Phys. status solidi*, vol. 252, no. 1, pp. 124–129, Jan. 2015, doi: https://doi.org/10.1002/pssb.201400080.

[41] T. S. Rajaraman, S. P. Parikh, and V. G. Gandhi, “Black TiO2: A review of its properties and conflicting trends,” *Chemical Engineering Journal*, vol. 389. Elsevier B.V., p. 123918, Jun. 01, 2020, doi: https://doi.org/10.1016/j.cej.2019.123918.

[42] L. S. Daniel, H. Nagai, N. Yoshida, and M. Sato, “Photocatalytic activity of vis-responsive Ag-nanoparticles/TiO2 composite thin films fabricated by molecular precursor method (MPM),” *Catalysts*, vol. 3, no. 3, pp. 625–645, Jul. 2013, doi: https://doi.org/10.3390/catal3030625.

[43] G. Koster, D. H. A. Blank, and G. A. J. H. M. Rijnders, “Oxygen in Complex Oxide Thin Films Grown by Pulsed Laser Deposition: a Perspective,” *J. Supercond. Nov. Magn.*, vol. 33, no. 1, pp. 205–212, 2020, doi: https://doi.org/10.1007/s10948-019-05276-5.

[44] J. Tauc, R. Grigorovici, and A. Vancu, “Optical Properties and Electronic Structure of Amorphous Germanium,” *Phys. Status Solidi*, vol. 15, no. 2, pp. 627–637, 1966, doi: https://doi.org/10.1002/pssb.19660150224.

[45] Q. Zhong, J. M. Vohs, and D. A. Bonnell, “Effect of reduction on the topographic and electronic structure of TiO2(110) surfaces,” *Surf. Sci.*, vol. 274, no. 1, pp. 35–43, 1992, doi: https://doi.org/10.1016/0039-6028(92)90097-P.

[46] B. Choudhury and A. Choudhury, “Oxygen defect dependent variation of band gap,

Urbach energy and luminescence property of anatase, anatase-rutile mixed phase and of rutile phases of TiO2 nanoparticles," *Phys. E Low-Dimensional Syst. Nanostructures*, vol. 56, pp. 364–371, Feb. 2014, doi: https://doi.org/10.1016/j.physe.2013.10.014.

[47] Y. Nakano, T. Morikawa, T. Ohwaki, and Y. Taga, "Origin of visible-light sensitivity in N-doped TiO2 films," *Chem. Phys*., vol. 339, no. 1–3, pp. 20–26, 2007, doi: https://doi.org/10.1016/j.chemphys.2007.05.031.

[48] J. Chen, N. A. Bogdanov, D. Usvyat, W. Fang, A. Michaelides, and A. Alavi, "The color center singlet state of oxygen vacancies in TiO2," *J. Chem. Phys*., vol. 153, no. 20, 2020, doi: https://doi.org/10.1063/5.0030658.

[49] P. G. Moses, A. Janotti, C. Franchini, G. Kresse, and C. G. Van De Walle, "Donor defects and small polarons on the TiO2(110) surface," *J. Appl. Phys*., vol. 119, no. 18, 2016, doi: https://doi.org/10.1063/1.4948239.

6 TMO Application in HJT Cells

The use of transition metal oxides for the selective carrier contact in the crystalline silicon solar cells technology is rising interest for the excellent optoelectrical properties of these materials whose implementation, however, can result in lousy performing cells due to an S-shaped electrical characteristic.

In this chapter, we fabricated solar cells showing S-shaped J-V curve and carried out a detailed analysis of the reasons of such behavior. We use a model involving the series of a standard cell equivalent circuit with a Schottky junction in order to explain these atypical performances. A good matching between the experimental measurements and the adopted theoretical model was obtained. The extracted parameters are listed and analyzed to shade light on the reasons behind the low-performance cells.

6.1 Introduction

The passivation properties of a-Si:H can be jeopardized by annealing at temperatures higher than 200°C [1]; therefore, the thermal budget of cells involving this material is limited and the manufacturing steps have to be carried out at lower temperatures. In this scenario, replacing the doped amorphous silicon with other materials like TMOs, which have excellent transparency (energy gap higher than 3 eV), is a viable alternative [2]. These materials can be deposited with low-temperature processes and can then meet the requirements for being inserted in the overall cells manufacturing process at a reduced cost. Several studies on the use of transition metal oxides for both hole and electron selective contacts have been published and there is interest in further investigation of TMOs-based heterojunction solar cells. In particular, molybdenum trioxide (MoO_3) and tungsten trioxide (WO_3) have been individuated as excellent candidates for the hole selective contact [3, 4]. However, the application of TMOs in HJT is recent compared to amorphous silicon and there is an intense interest in the optimization of solar cells involving such materials [5, 6]. On the other hand, TMO based solar cells can be affected by the formation of S-shaped J–V curves [7], which lead to a considerable decrease in the electrical performances of the cells influencing the fill factor negatively and increasing the losses. For this reason, expanding the knowledge behind the formation mechanisms of the S-shaped current is essential in order to avoid such behavior and further the dissemination of the TMO-based heterojunction technology.

In this chapter, we aim to collect information and improve knowledge about the

behavior of TMOs in solar cells by applying sub-stoichiometric MoO_x and WO_x ($x\approx3$) as selective hole contacts and TiO_x ($x\approx2$) as selective electron contact in c-Si HJT. First, we investigated the optical properties of the TMO layers deposited on quartz substrates by means of PLD, a technique that allows obtaining a controllable and reproducible deposition of a broad number of metal oxides [8-17]. Then we used the same process to fabricate the TMO-based hole selective contact in solar cell prototypes based on n-type nanocrystalline silicon oxide [18]. After the electrical characterization, we reported S-shaped DC characteristics for all the prototypes. Finally, we used a validated electrical model [19] to fit the DC electrical characteristics and extract the parameters of the equivalent circuit.

6.2 Experimental details

The films of MoO_x, WO_x and TiO_x were deposited by PLD at room temperature (25 °C). Commercially available quartz (2 cm × 2 cm) was used as substrates. Before deposition, the substrates were cleaned by ultrasonic bath in acetone for 10 min and then rinsed in isopropyl alcohol and dried up with compressed air. The PLD employed system is described in section 3.1.2. and includes a Q-switched tripled Nd:YAG laser (Quantel mod. YG78C20; λ = 355 nm) generating 6 ns width pulses with an energy of 80 mJ per pulse. MO_3 and WO_3 targets (99.9% pure) were both a 1-inch diameter, 0.25-inch thick, sintered MO_3 and WO_3 ceramic disks, respectively. For the TiO_2 a 99.5% pure precursor was used.

The films were deposited with different oxygen pressures (for MoO_x and WO_x: PO_2 of 3×10^{-2}, 6×10^{-2}, 1×10^{-1} mbar, for TiO_x: PO_2 of 2×10^{-2}, 1×10^{-2}, 1×10^{-3} mbar) to evaluate the influence of this deposition parameter on the optoelectrical properties of the transition metal oxides. The thicknesses of these samples were evaluated by ellipsometry to calibrate the number of pulses needed to obtained a desired thickness. A mean thickness of 400 nm resulted for the molybdenum samples, 1000 nm for the tungsten oxide and 150 for the titania ones. The transmissivity measurements of such films were carried out in the UV-VIS range using a Varian DMS 90 spectrophotometer system.

The solar cell prototypes were fabricated following the process described in [18] based on stacks of hydrogenated nanocrystalline silicon oxide (nc-SiO_x:H) and hydrogenated nanocrystalline silicon (nc-Si:H) implementing one of the carrier selective contact with a transition metal oxide layer. The absorber is a n-type <111> oriented c-Si wafer (280 µm thick, resistivity of 2.5 Ω·cm and doping concentration of 1.9×10^{15} cm^{-3}).

Figure 6.1a sketches the structure of the cells with a TMO-based hole selective

contact (MoO_x and WO_x); first, the electron contact was formed by PECVD (Plasma Enhanced Chemical Vapor Deposition) with a stack of 8 nm thick a-Si:H(i) passivation layer and then 11 nm of nc-SiO_x:H(n)/nc-Si:H(n); subsequently, on the other face of the wafer, a passivation layer of 9 nm of a-Si:H(i) was deposited by PECVD. Afterward, the prototypes were obtained by dicing the wafer in squares of 1.5×1.5 cm^2 and prepared for the deposition of the hole selective contact. The prototypes were divided into two sets of three cells each: MoO_x was used in one set while WO_x for the other one. These layers of TMO were deposited on top of the a-Si:H(i) passivation layer as sketched in Figure 6.1a setting the thickness of these layers at 7 nm. Similarly, to the films deposited on quartz, PO_2 of 3×10^{-2}, 6×10^{-2} and 10×10^{-2} mbar were used for the deposition of the oxides onto the solar cell stack in order to study the performances of the cells against different PO_2 deposition conditions. Finally, the prototypes were finalized by sputtering of indium tin oxide (ITO) as an anti-reflecting coating (70 nm on the front side, 140 nm on the backside) while metallization was obtained by thermal evaporation of 1 μm-thick aluminum on both faces of the devices. In particular, the bottom contact was obtained with a plan Al deposition onto the nc-SiO_x:H/nc-Si:H film, whilst the top contact, having a grid pattern, was deposited onto the ITO film through a shadow mask. A photo of the final device is presented in Figure 6.2; the area of the completed cell is 1 cm^2.

Figure 6.1b sketches the structure of the cells with a TMO-based electron selective contact based on TiO_x. The p-contact was formed by Plasma Enhanced Chemical Vapor Deposition (PECVD) with a stack of 9 nm a-Si:H(i), 10 nm of nc-SiO_x:H and 10 nm of nc-Si:H; the n-contact was prepared with a passivation layer of 9 nm of a-Si:H(i). From the wafer, a square of 1.5 cm×1.5 cm was obtained from the dicing of the wafer and used for the electron selective contact depositing 5 nm of TiO_x by Pulsed Laser Deposition on top of passivation layer. The prototypes were finalized by sputtering of indium tin oxide (ITO) as an anti-reflecting coating (70 nm on the front side, 140 nm on the backside) while metallization was obtained by thermal evaporation of 1 μm-thick aluminum on both faces of the devices. In particular, the bottom contact was obtained with a full Al deposition onto the TiO_x film, while the top contact was deposited onto the ITO film through a shadow mask with a grid pattern (see Figure 6.2).

The current density–voltage (J–V) characteristics of the devices were measured with a source-meter under standard test condition (STC: 1 sun, T_{CELL} 25°C, air mass 1.5).

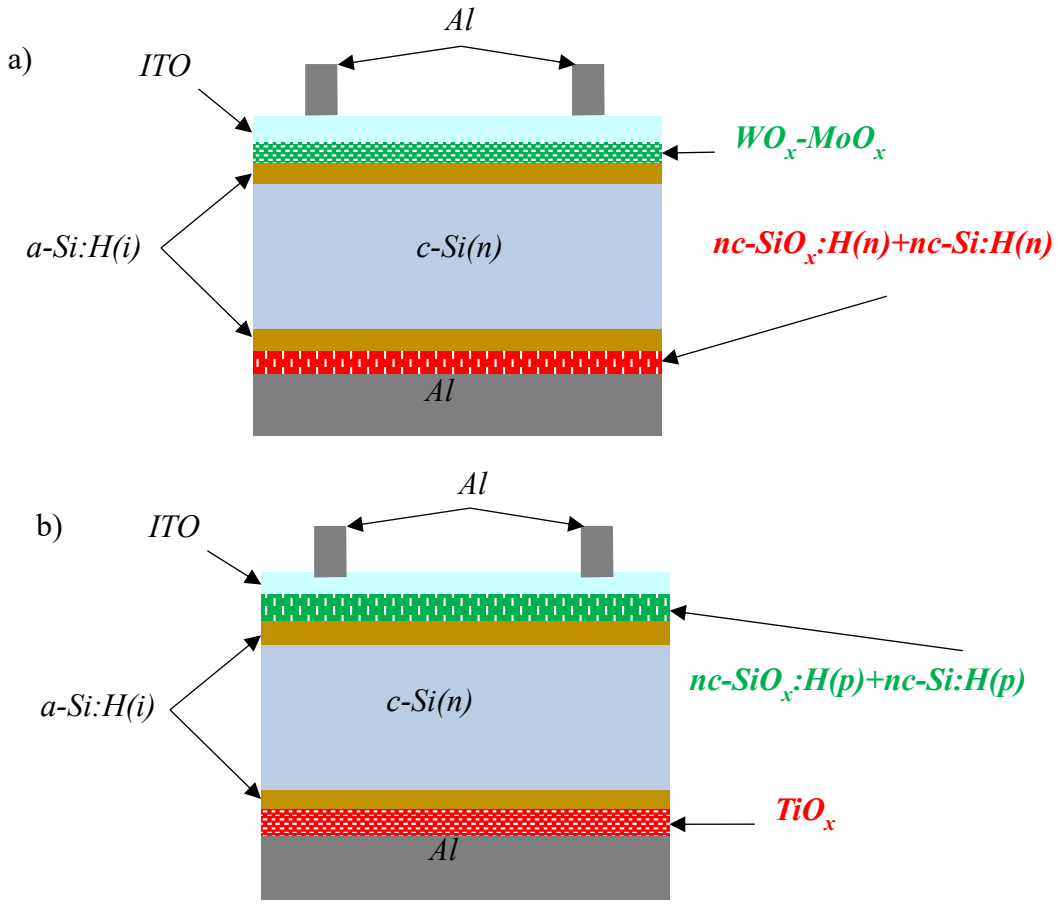

Figure 6.1 *Sketch of the HJT solar cell with a) TMO-based hole selective contact, b) TMO-based electron selective contact,*

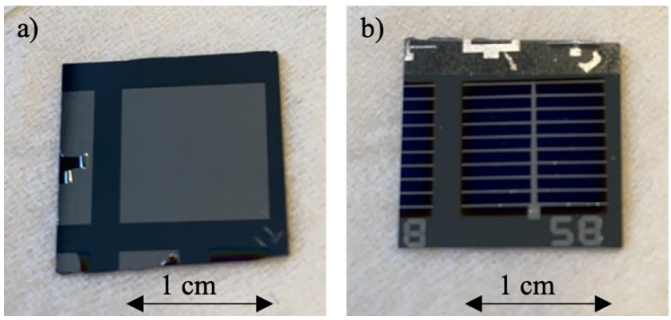

Figure 6.2 *Solar cell prototype: a) back contact, b) top contact*

6.3 Optoelectrical characterization

6.3.1 Film characterization

The optical properties of the TMOs were evaluated from the samples grown by PLD on quartz. The transmissivity spectra of the MoO_x samples, presented in Figure 6.3, show that the material absorbs most of the light in the 200-350 nm range and is transparent for higher wavelengths. Moreover, the transmissivity depends on the PO_2: the higher is the oxygen pressure, the higher is the film transmissivity.

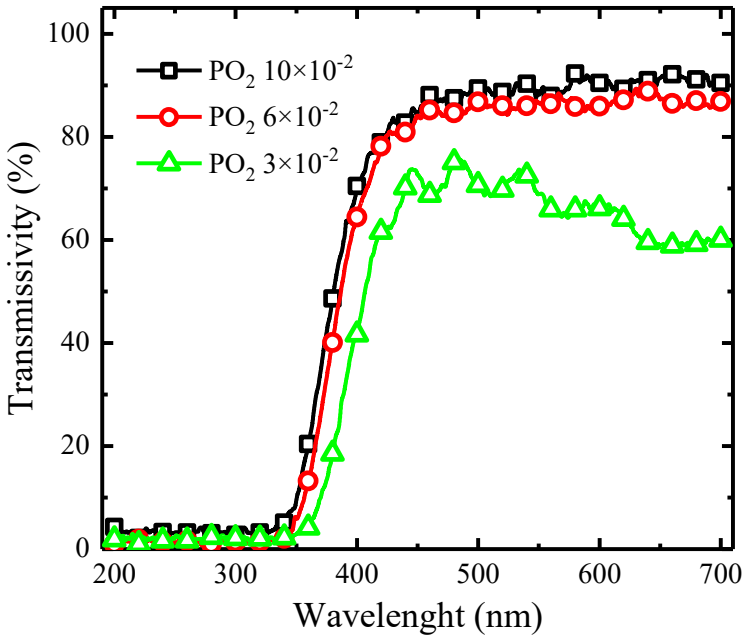

Figure 6.3 *Transmissivity spectra of the MoO_x films on a quartz substrate for different deposition pressures (mbar)*

Regarding the tungsten oxide films, the transmissivity spectra are presented in Figure 6.4; similar to the molybdenum oxide case, the films are opaque in the 200-310 nm range and then transparent for higher wavelengths; while the highest transmissivity values are obtained with the intermediate oxygen pressures of 6×10^{-2} mbar.

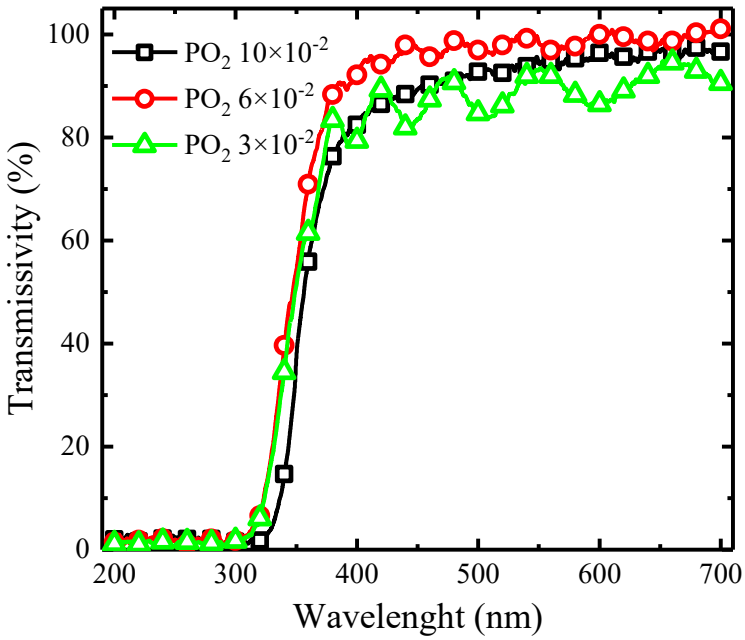

Figure 6.4 *Transmissivity spectra of the WO_x films on a quartz substrate for different deposition pressures (mbar)*

Finally, the TiO_x transmissivity is presented in Figure 6.5. highlighting the influence of the oxygen pressure on transmissivity. Indeed, the curves shift to shorter wavelengths for

rising PO_2, indicating that the material becomes more transparent.

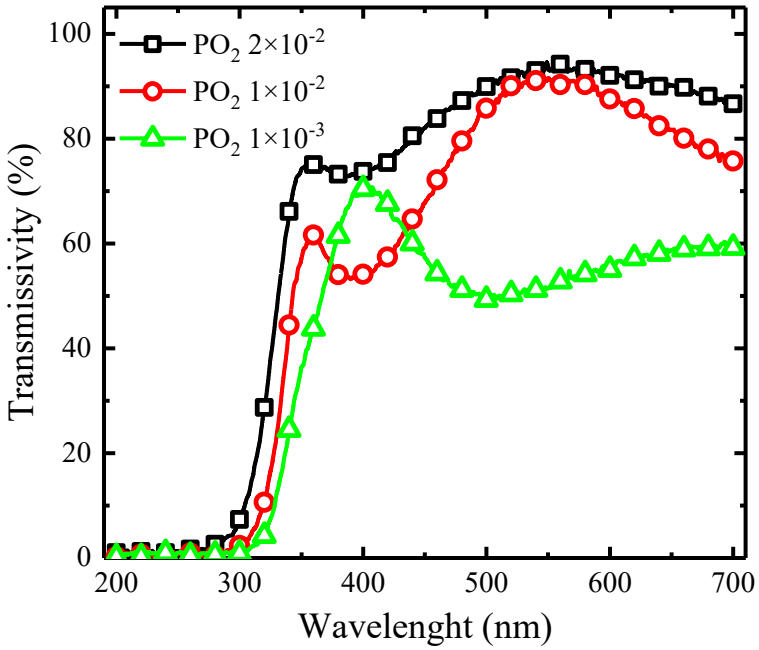

Figure 6.5 *Transmissivity spectra of the TiO_x films on a quartz substrate for different deposition pressures (mbar)*

From the transmissivity data is also possible to evaluate optical bandgap (E_{opt}) of the material through the linear regression of the Tauc's relation [20] reported in the following equation:

$$(\alpha h\nu)^n = B\,(h\nu - E_{opt}) \tag{6.1}$$

Where α is the absorption coefficient (calculated from the transmissivity through the *Lambert-Beer's Law*), $h\nu$ is the energy of the incident photon, n is a material-dependent coefficient, equals to 2 for direct bandgap materials as molybdenum and tungsten oxides [21, 22] and ½ for the indirect bandgap materials as titanium oxide [23, 24]. Table 6.1 summarizes the optical energy gap data for all the samples. The energy gap is always above 3 eV and the optical energy gap is higher for the samples deposited at the intermediate pressure for the MoO_x and WO_x films (6×10^{-2} mbar) whereas for the TiO_x the highest value was achieved with a deposition pressure of 2×10^{-2} mbar. Variations in the optical gap and the transparency of the transition metal oxides are due to the significant presence of oxygen vacancies formed during the deposition; particularly, a low oxygen pressure during deposition enhances this phenomenon. The oxygen vacancies cause the films to be sub-stoichiometric (MoO_x and WO_x with x approaching 3, TiO_x with x approaching 2). This characterization underlines the remarkable optical properties of these transition metal oxides, highlighting the high transparency for wavelengths higher than 350 nm, making them excellent candidates for the carrier selective contacts for HJT. Moreover, with respect to a-

Si:H, the transition metal oxides have a higher optical gap, reducing the parasitic absorption.

Table 6.1 *Optical energy gap*

Deposition pressure (mbar)	*Optical band gap (eV)*		*Deposition pressure (mbar)*	*Optical band gap (eV)*
	MoO_x	WO_x		TiO_x
3×10^{-2}	3.00	3.29	1×10^{-3}	3.31
6×10^{-2}	3.16	3.39	1×10^{-2}	3.32
10×10^{-2}	3.03	3.23	2×10^{-2}	3.38

6.3.2 Solar cell characterization

The experimental J-V curve characteristics under AM 1.5 illumination for the HJT solar cells with TMOs as selective carrier contacts are presented in Figure 6.6 (MoO_x), Figure 6.7 (WO_x) and Figure 6.8 (TiO_x).

All the samples showed an S-shaped J-V characteristic, except for titanium oxide case: only the cell with the TiO_x deposited at 1×10^{-3} mbar presents a valuable DC characteristic, whereas the other cells failed. This phenomenon can be associated with a barrier for the extraction of the charge carriers through the introduced TMO films. This barrier is due to the imperfect alignment of the band structure in the cell, between the layers of TMO and the intrinsic hydrogenated amorphous silicon as confirmed by several authors [25, 26] and is a limitation in the optimization of the TMO-based solar cells. In fact, the properties of TMOs, such as optical band gap, work function, crystallinity and stoichiometry, depend on the deposition technique as well as the substrate temperature and the deposition oxygen pressure. The variations of these parameters lead to suboptimal electrical DC characteristics. It is worth noting a common trend in the open circuit voltage, V_{OC}, and the short circuit current density, J_{SC}, of both materials; in fact, as the oxygen pressure increases both V_{OC} and J_{SC} rise.

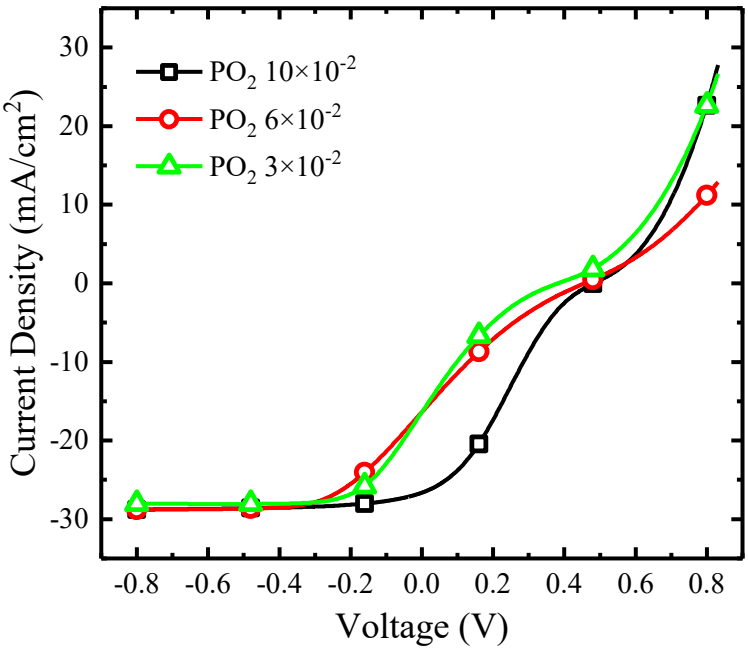

Figure 6.6 *J-V characteristics of the MoOx-based heterojunction solar cells against the different oxygen pressures (mbar)*

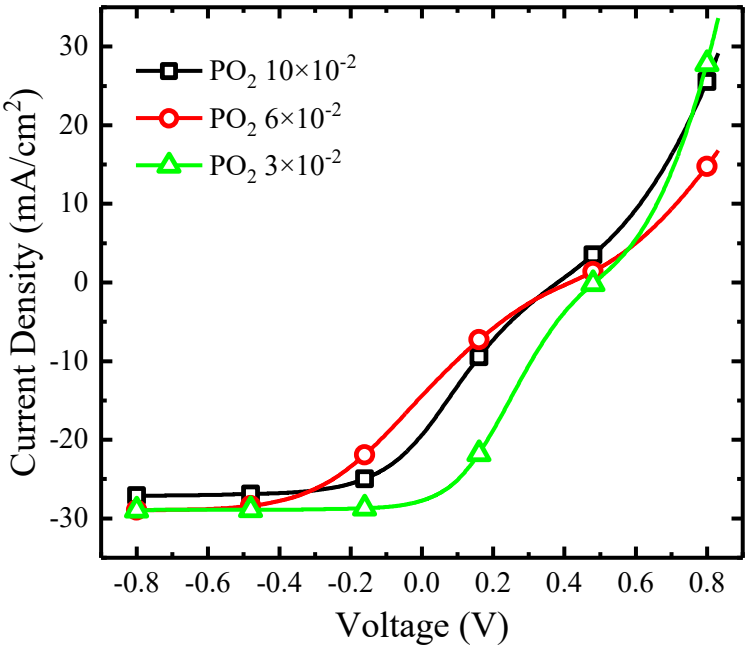

Figure 6.7 *J-V characteristics of the WO_x-based heterojunction solar cells against the different oxygen pressures (mbar)*

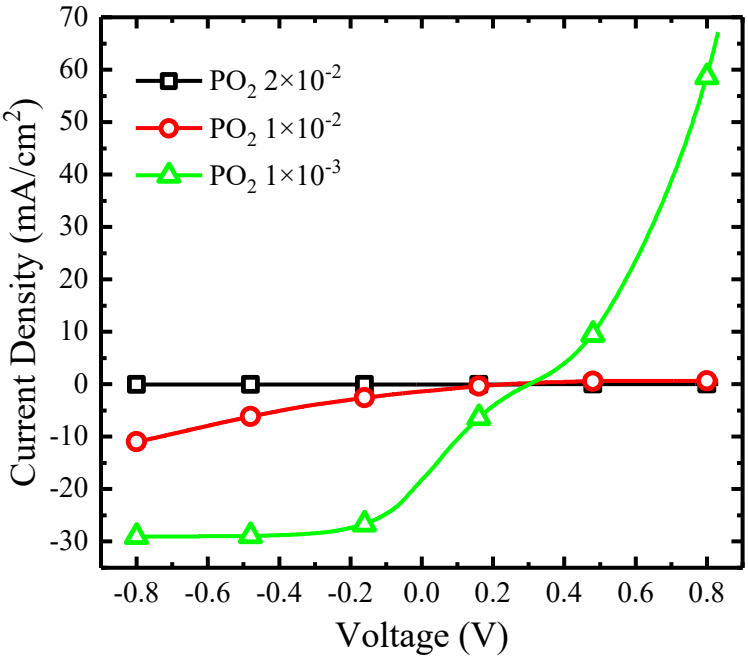

Figure 6.8 *J-V characteristics of the TiO_x-based heterojunction solar cells against the different oxygen pressures (mbar)*

6.4 Solar cell parameters extraction

6.4.1 Theoretical model

The model of a standard HJT is similar to silicon cells based on p–n junctions but the presence of an S-shape J-V characteristic cannot be explained with this model; as a matter of fact, many examples exist in the literature for modeling cells with an anomalous S-shape DC electrical characteristic [27-29]. In this paper, we adopted the equivalent circuit model (Figure 6.9) developed in [19] in which a rectifying junction is connected in series with the heterojunction to model a Schottky barrier.

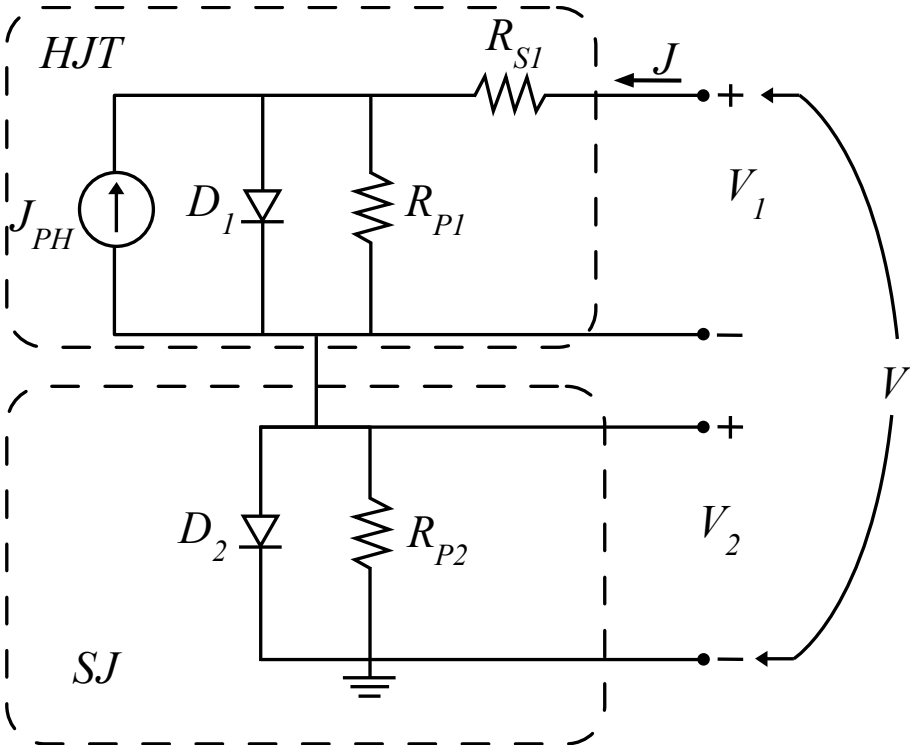

Figure 6.9 *Equivalent circuit of a heterojunction (HJT) solar cell with a series Schottky junction (SJ)*

The heterojunction equivalent model of the solar cell is described by equations (6.2-(6.4)):

$$J = J_{01}\left(\exp\left(\frac{V_1 - JR_{S1}}{n_1 V_T}\right) - 1\right) + \frac{V_1 - JR_{S1}}{R_{P1}} - J_{PH} \tag{6.2}$$

$$J = J_{02}\left(exp\left(\frac{V_2}{n_2 V_T}\right) - 1\right) + \frac{V_2}{R_{P2}} \tag{6.3}$$

$$V = V_1 + V_2 \tag{6.4}$$

where J is the current density through the solar cell, V is the bias voltage of the cell; for the heterojunction, V_1 is the bias voltage, J_{01} is the leakage current density, n_1 is the ideal factor for the diode of the heterojunction, V_T is the thermal voltage (25.85 mV at 300 K) and R_{S1} is the series resistance which includes the exponential diode current, the current loss in the shunt resistance (R_{P1}) and the photogenerated current density (J_{PH}). For the Schottky junction, J_{02} is the leakage current density, V_2 is the bias voltage of the Schottky junction, n_2 is the ideal factor for the diode.

Equation (6.3) includes both an exponential diode current and a leakage current terms due to a shunt resistance (R_{P2}). It should be noted that the current density through both heterojunction and Schottky junction is the same, while the overall voltage (V) is split among the junctions.

An expression of the voltage V_2 in function of J is needed for the calculation of

equation (6.2); such expression can be obtained through algebraic manipulation in a transcendental form which can be solved numerically, i.e., with the Newton-Raphson method. In this work, the *Lambert W* function [30] was used to extract a direct expression of V_2 as expressed in (6.5). This method involves a lighter computational load and higher accuracy in comparison to the Newton-Raphson method.

$$V_2 = R_{P2}(J_{02} + J) + n_2 V_T \, W\left(\frac{J_{02} R_{P2}}{n_2 V_T} \exp\left(\frac{R_{P2}(J_{02} + J)}{n_2 V_T}\right)\right) \tag{6.5}$$

6.4.2 Parameters extraction

Equations (6.2), (6.4) and (6.5) were used to fit the experimental J-V curves of the MoO_x a, WO_x and TiO_x-based solar cells by the minimization of a least-squares problem. By using this procedure, quantitative values of the cell parameters were obtained and listed in Table 6.2 for the MoO_x, in Table 6.3 for the WO_x and in Table 6.4 for the TiO_x-based solar cells. The resulting parameters allow a more in-depth analysis and comprehension of the device and its mechanisms. As shown in Figure 6.10, Figure 6.11 and in Figure 6.12, a proper fitting was obtained for the experimental data in the entire voltage range; moreover, a simulation of the J-V curve involving only the heterojunction parameters without the Schottky junction was added for comparison.

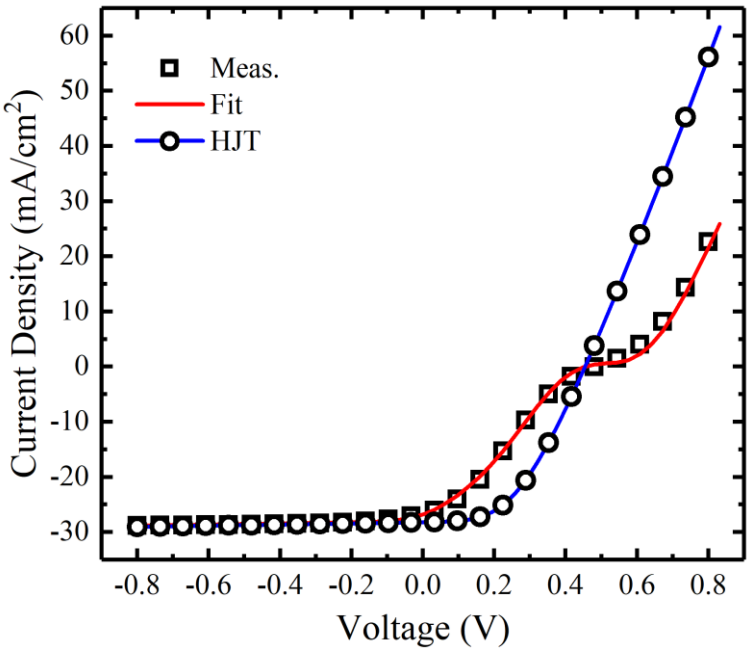

Figure 6.10 *Fitting of the J-V characteristic of the solar cell with MoO_x deposited at $PO_2 = 10\times10^{-2}$ mbar.*

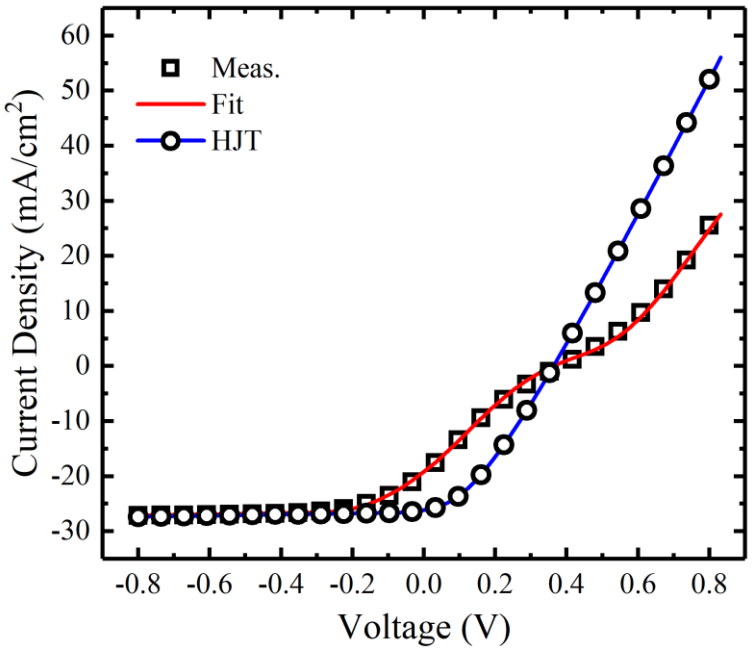

Figure 6.11 *Fitting of the J-V characteristic of the solar cells with WO_x deposited at $PO_2 = 3\times10^{-2}$ mbar.*

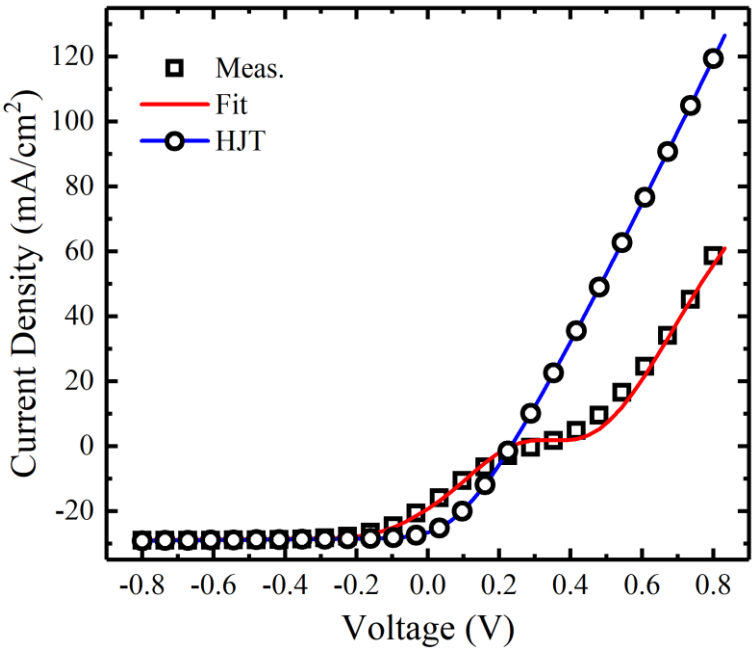

Figure 6.12 *Fitting of the J-V characteristic of the solar cells with TiO_x deposited at $PO_2 = 1\times10^{-3}$ mbar.*

Table 6.2 *MoO_x Solar Cell Parameters*

Deposition pressure (mbar)	*Heterojunction*					*Schottky junction*		
	J_{01}	R_{S1}	R_{P1}	N_1	J_{PH}	J_{02}	R_{S2}	n_2
3×10^{-2}	4.7E-6	7.9	1340	1.5	2.8E-2	6.7E-5	8.9	2.7
6×10^{-2}	3.8E-7	10.9	1010	1.5	2.9E-2	5.0E-5	11.6	2.7
10×10^{-2}	6.5E-7	5.3	1010	1.6	2.9E-2	2.6E-4	6.7	2.7

Table 6.3 *WO_x Solar Cell Parameters*

Deposition pressure (mbar)	*Heterojunction*					*Schottky junction*		
	J_{01}	R_{S1}	R_{P1}	N_1	J_{PH}	J_{02}	R_{S2}	n_2
3×10^{-2}	2.5E-6	7.6	1000	1.5	2.7E-2	1.40E-4	8.5	2.7
6×10^{-2}	7.9E-7	11.4	1000	1.5	2.9E-2	9.20E-5	12.0	2.7
10×10^{-2}	9.2E-7	4.7	1030	1.7	2.9E-2	3.91E-4	6.0	2.7

Table 6.4 *TiO_x Solar Cell Parameters*

Deposition pressure (mbar)	*Heterojunction*					*Schottky junction*		
	J_{01}	R_{S1}	R_{P1}	N_1	J_{PH}	J_{02}	R_{S2}	n_2
1×10^{-3}	1.4E-4	4.14	1000	1.69	2.82E-2	1.59E-4	5.2	2.7

Comparing the experimental data with the simulated heterojunction cell makes it possible to highlight several aspects valid for both the TMOs-based cells.

First, the HJT curves and the experimental ones share the same V_{OC}. In fact, when the input voltage reaches the open circuit value, the current density in the whole device is zero and the total bias voltage is then applied at the top section of the circuit model (Figure 6.9), implying that the Schottky junction is not involved in the determination of the V_{OC}. Moreover, the open-circuit voltage grows as the deposition pressure rises, meaning that the devices with the higher oxygen deposition pressure have the lowest recombination losses. It is worth noting that the V_{OC} depends on the saturation current density J_{01} whose values were extracted through the fitting and exhibit a descending trend as the PO_2 rises. This applies to both the MoO_x and WO_x cells.

Second, the slope in the DC characteristic near the open-circuit voltage depends on the differential conductance of the device. The Schottky barrier conductance dominates this value at the open-circuit voltage ($1/R_{P2}$), which is much lower than the differential conductance of the heterojunction ($1/R_{P1}$). For this reason, the slope of the characteristic changes at around V_{OC} forming the S-shaped curve. When the bias voltage further increases, D_2 enters in conduction, shortening R_{P2} and the J-V curve slope is now equal to $1/R_{P1}$ as in the HJT simulated cell. The Schottky barrier causes a shift of the J-V curve toward higher voltage with respect to the simulated heterojunction cell; in fact, D_2 increases the forward turn-on voltage of the cell.

Finally, for bias voltage smaller than V_{OC}, the Schottky junction is reversely biased, which represents an obstacle for the charge transport through the device. Due to this, current density of the prototypes, at a parity of voltage, is lower than the corresponding HJT cells resulting in a lower fill factor. As the bias voltage further decreases, the photogenerated current density is dominant and J reaches its minimum value, which is equal to the HJT simulated one.

6.5 Conclusions

The transition metal oxides MoO_x, WO_x and TiO_x were first deposited onto quartz substrates, and then optically characterized. The impact of these materials as selective carrier contacts in c-Si heterojunction solar cells was successively tested by realizing a set of prototypes with TMOs deposited at different oxygen pressures. Afterward, the fabricated cells were electrically characterized and all the devices exhibited an S-shaped DC J-V curve. The behavior of these cells was analyzed by the implementation of a model previously developed for solar cells presenting anomalous electrical characteristics. The experimental data were used to determine a quantitative parameter for the solar cell equivalent parameters. The simulated characteristics resulted in a good fit with the measured data for a broad voltage range. The results show the potential of the TMO-based c-Si HJT and giving input for further optimization of the *doping-free* TMO-based cells.

References

[1] B. Macco *et al*., "Correlating the silicon surface passivation to the nanostructure of low-temperature a-Si:H after rapid thermal annealing," *J. Appl. Phys.,* vol. 122, no. 3, 2017, doi: https://doi.org/10.1063/1.4994795.

[2] J. Melskens, B. W. H. Van De Loo, B. Macco, L. E. Black, S. Smit, and W. M. M. Kessels, "Passivating Contacts for Crystalline Silicon Solar Cells: From Concepts and Materials to Prospects," *IEEE J. Photovoltaics*, vol. 8, no. 2, pp. 373–388, 2018, doi: https://doi.org/10.1109/JPHOTOV.2018.2797106.

[3] C. Battaglia *et al.,* "Hole selective MoOx contact for silicon solar cells," *Nano Lett*., vol. 14, no. 2, pp. 967–971, Feb. 2014, doi: https://doi.org/10.1021/nl404389u.

[4] M. Bivour, J. Temmler, H. Steinkemper, and M. Hermle, "Molybdenum and tungsten oxide: High work function wide band gap contact materials for hole selective contacts of silicon solar cells," *Sol. Energy Mater. Sol. Cells*, vol. 142, pp. 34–41, 2015, doi: https://doi.org/10.1016/j.solmat.2015.05.031.

[5] R. A. Vijayan *et al*., "Hole-Collection Mechanism in Passivating Metal-Oxide Contacts on Si Solar Cells: Insights from Numerical Simulations," *IEEE J. Photovoltaics,* vol. 8, no. 2, pp. 473–482, 2018, doi: https://doi.org/10.1109/JPHOTOV.2018.2796131.

[6] D. Scirè, P. Procel, A. Gulino, O. Isabella, M. Zeman, and I. Crupi, "Sub-gap defect density characterization of molybdenum oxide: An annealing study for solar cell applications," *Nano Res*., vol. 13, no. 12, pp. 3416–3424, 2020, doi: https://doi.org/10.1007/s12274-020-3029-9.

[7] C. Messmer, M. Bivour, J. Schön, and M. Hermle, "Requirements for efficient hole extraction in transition metal oxide-based silicon heterojunction solar cells," *J. Appl. Phys.*, vol. 124, no. 8, 2018, doi: https://doi.org/10.1063/1.5045250.

[8] T. Cesca *et al*., "Correlation between in situ structural and optical characterization of the semiconductor-to-metal phase transition of VO2 thin films on sapphire," *Nanoscale*, vol. 12, no. 2, pp. 851–863, 2020, doi: https://doi.org/10.1039/c9nr09024j.

[9] A. Boughelout, R. Macaluso, I. Crupi, B. Megna, M. S. Aida, and M. Kechouane, "Improved Cu2O/AZO Heterojunction by Inserting a Thin ZnO Interlayer Grown

by Pulsed Laser Deposition," *J. Electron. Mater.*, vol. 48, no. 7, pp. 4381–4388, 2019, doi: https://doi.org/10.1007/s11664-019-07195-6.

[10] A. Boughelout, R. Macaluso, M. Kechouane, and M. Trari, "Photocatalysis of rhodamine B and methyl orange degradation under solar light on ZnO and Cu2O thin films," *React. Kinet. Mech. Catal.*, vol. 129, no. 2, pp. 1115–1130, 2020, doi: https://doi.org/10.1007/s11144-020-01741-8.

[11] M. Barbouche et al., "New process of silicon carbide purification intended for silicon passivation," *Superlattices Microstruct.*, vol. 101, pp. 512–521, 2017, doi: https://doi.org/10.1016/j.spmi.2016.11.064.

[12] A. Sacco *et al.*, "Enhancement of photoconversion efficiency in dye-sensitized solar cells exploiting pulsed laser deposited niobium pentoxide blocking layers," *Thin Solid Films*, vol. 574, pp. 38–42, 2015, doi: https://doi.org/10.1016/j.tsf.2014.11.054.

[13] M. Mosca *et al.*, "Optical, structural, and morphological characterisation of epitaxial ZnO films grown by pulsed-laser deposition," *Thin Solid Films*, vol. 539, pp. 55–59, 2013, doi: https://doi.org/10.1016/j.tsf.2013.04.146.

[14] R. Macaluso *et al.*, "Erroneous p-type assignment by Hall effect measurements in annealed ZnO films grown on InP substrate," *J. Appl. Phys.*, vol. 113, no. 16, 2013, doi: https://doi.org/10.1063/1.4803080.

[15] C. Calì, R. Macaluso, and M. Mosca, "In situ monitoring of pulsed laser indium-tin-oxide film deposition by optical emission spectroscopy," *Spectrochim. Acta - Part B At. Spectrosc.*, vol. 56, no. 6, pp. 743–751, 2001, doi: https://doi.org/10.1016/S0584-8547(01)00193-8.

[16] R. Macaluso *et al.*, "Resistive switching behaviour in ZnO and VO2 memristors grown by pulsed laser deposition," *Electron. Lett.*, vol. 50, no. 4, pp. 262–263, 2014, doi: https://doi.org/10.1049/el.2013.3175.

[17] R. Macaluso *et al.*, "Progress in violet light-emitting diodes based on ZnO/GaN heterojunction," *Electron.*, vol. 9, no. 6, 2020, doi: 10.3390/electronics9060991.

[18] Y. Zhao *et al.*, "Doped hydrogenated nanocrystalline silicon oxide layers for high-efficiency c-Si heterojunction solar cells," *Prog. Photovoltaics Res. Appl.*, vol. 28, no. 5, pp. 425–435, May 2020, doi: https://doi.org/10.1002/pip.3256.

[19] L. Zuo, J. Yao, H. Li, and H. Chen, "Assessing the origin of the S-shaped I-V curve

in organic solar cells: An improved equivalent circuit model," *Sol. Energy Mater. Sol. Cells*, vol. 122, pp. 88–93, 2014, doi: https://doi.org/10.1016/j.solmat.2013.11.018.

[20] J. Tauc, R. Grigorovici, and A. Vancu, "Optical Properties and Electronic Structure of Amorphous Germanium," *Phys. Status Solidi*, vol. 15, no. 2, pp. 627–637, 1966, doi: https://doi.org/10.1002/pssb.19660150224.

[21] K. Inzani, M. Nematollahi, F. Vullum-Bruer, T. Grande, T. W. Reenaas, and S. M. Selbach, "Electronic properties of reduced molybdenum oxides," *Phys. Chem. Chem. Phys.*, vol. 19, no. 13, pp. 9232–9245, 2017, doi: https://doi.org/10.1039/c7cp00644f.

[22] I. Kostis et al., "Hot-wire substoichiometric tungsten oxide films deposited in hydrogen environment with n-type conductivity," *J. Phys. D. Appl. Phys*., vol. 45, no. 44, 2012, doi: https://doi.org/10.1088/0022-3727/45/44/445101.

[23] R. Dannenberg and P. Greene, "Reactive sputter deposition of titanium dioxide," *Thin Solid Films*, vol. 360, no. 1–2, pp. 122–127, Feb. 2000, doi: https://doi.org/10.1016/S0040-6090(99)00938-4.

[24] A. A. Akl, H. Kamal, and K. Abdel-Hady, "Fabrication and characterization of sputtered titanium dioxide films," *Appl. Surf. Sci*., vol. 252, no. 24, pp. 8651–8656, 2006, doi: https://doi.org/10.1016/j.apsusc.2005.12.001.

[25] S. Mudgal, M. Nayak, S. Singh, and V. K. Komarala , "Study of anomalous S-shape in current density-voltage characteristics of carrier selective contact molybdenum oxide and amorphous silicon based heterojunction silicon solar cells," in *AIP Conference Proceedings*, 2019, vol. 2147, doi: https://doi.org/10.1063/1.5123814.

[26] R. Saive, "S-Shaped Current–Voltage Characteristics in Solar Cells: A Review," in *IEEE Journal of Photovoltaics*, vol. 9, no. 6, pp. 1477-1484, Nov. 2019, doi: https://doi.org/10.1109/JPHOTOV.2019.2930409.

[27] A. Aghassi, C. D. Fay, and A. Mozer, "Investigation of S-shaped current-voltage characteristics in high-performance solution-processed small molecule bulk heterojunction solar cells," *Org. Electron*., vol. 62, pp. 133–141, 2018, doi: https://doi.org/10.1016/j.orgel.2018.07.025.

[28] F. J. García-Sánchez, D. Lugo-Muñoz, J. Muci, and A. Ortiz-Conde, "Lumped parameter modeling of organic solar cells' S-shaped I-V characteristics," *IEEE J.*

Photovoltaics, vol. 3, no. 1, pp. 330–335, 2013, doi: https://doi.org/10.1109/JPHOTOV.2012.2219503.

[29] F. J. García-Sánchez and B. Romero, "Equivalent Circuit Models for Next Generation Photovoltaic Devices with S-shaped I-V Curves," *2019 8th International Symposium on Next Generation Electronics (ISNE)*, Zhengzhou, China, 2019, doi: https://doi.org/10.1109/ISNE.2019.8896544.

[30] R. M. Corless, G. H. Gonnet, D. E. G. Hare, D. J. Jeffrey, and D. E. Knuth, “On the Lambert W function,” *Adv. Comput. Math*., vol. 5, no. 1, pp. 329–359, Dec. 1996, doi: https://doi.org/10.1007/bf02124750.

7 Conclusions

The use of TMOs as carrier selective contact represents a viable alternative to the more common a-Si:H. Transition metal oxides with high work function, such as molybdenum oxide, tungsten oxide, and vanadium oxide, allow for a good alignment of the TMO's valence band with the conduction band of c-Si, consenting to an efficient collection of the photogenerated holes while blocking the electrons. Instead, for the electron selective contact, a lower work function material, such as titanium oxide and zinc oxide, makes a good alignment between the TMO and absorber conduction bands, allowing the electron transport while blocking the holes. It is worth noting that for both types of carrier selective contact (CSC), extensive knowledge of the materials optical and electrical properties is fundamental in their optimization process. The information regarding the defect density of states (DOS) at the TMO interface was highlighted to be essential for understanding the tunnelling mechanisms, improving the conductivity of the material and addressing the parasitic absorption. Simulation studies reported optimizing CSC in HJT solar cells, but considering the limited data on the DOS, such results may not be reproduced in an actual solar cell. Indeed, the numerical information on the DOS of MoO_x and other transition metal oxides is still missing. Without this data, any solar cells simulation endowed with such materials risk to be not accurate or even physically feasible.

Therefore, the characterization of the transition metal oxides defect density of states is essential for the researchers' request for reliable and accurate information that can be used for their simulations and subsequent optimization of the doping-free solar cells. In this scenario, th analysis and characterization of amorphous molybdenum oxide and titanium oxide have been performed. Optical spectra displayed a pronounced absorption peak in the near-infrared range, associated with small polaron absorption. The explanation of this phenomenon can be found in the binding between the small polaron formation and the defect formation. From the fitting of the experimental absorption spectra, through the evaluation of optical transition over the bandgap and from the result of polaron theory, it was found that the inter-band defect distribution.

From our analysis and polaron theory, it was possible to obtain parameters useful to simulate MoO_x in advanced device simulators appropriately. Data shown here represent a first step in the characterization framework that can be extended to other transition metal oxides exhibiting similar behavior.

Finally, transition metal oxides (MoO_x, WO_x and TiO_x) were deposited and

characterized to address the impact of these materials as selective carrier contacts in c-Si heterojunction solar cells. A set of prototypes with TMOs deposited at different oxygen pressures was provided and the cells were electrically characterized, exhibiting an S-shaped DC J-V curve. The behavior of these cells was analyzed by implementing a previously developed model for solar cells presenting anomalous electrical characteristics. The experimental data were used to determine a quantitative parameter for the solar cell equivalent parameters. The simulated characteristics resulted in a good fit with the measured data for a broad voltage range. The results show the potential of the TMO-based c-Si HJT and giving input for further optimization of the *doping-free* TMO-based cells.

List of the Figures

Figure 1.1 Photon absorption in a semiconductor: a) photon energy E_{ph} equal to E_G; b) E_{ph} greater than E_G 2
Figure 1.2 Photogenerated carriers behavior inside a p-n junction: a) generation of electron-hole pairs from photon absorption; b) recombination losses; c) separation and emission of electrons; d) the electrons flow through the external circuit e) hole collection at the back contact. 3
Figure 1.3 Equivalent circuit of a solar cell based on the single diode model 5
Figure 1.4 I-V characteristic of a typical solar cell under illumination (red line); P-V characteristic (blue line) with the maximum power point (MPP). 6
Figure 1.5 Architecture of a simple solar cell 7
Figure 1.6 Schematic of a heterojunction solar cell 8
Figure 1.7 Band diagram of a typical HJT cell 9
Figure 2.1 Band diagram of a c-Si cell with a TMO-based p-contact 18
Figure 2.2 HJT solar cells structures using MoO_x as hole-selective-contact. 19
Figure 2.3 Structure of a HJT with a WO_x hole selective contact 21
Figure 2.4 Structure of HJT cell exploiting V_2O_5 as CSC: a) with pyramidal texturing, b) without texturing 23
Figure 2.5 Structure of a HJT solar cell with a NiO:Cu hole selective contact 25
Figure 2.6 band diagram of a c-Si cell with a TMO-based n-contact 27
Figure 2.7 Structure of an HJT solar cell with an ATOM contact 28
Figure 2.8 Structure of a HJT with n selective contact with ZnO or Zn:O 30
Figure 3.1 Thermal evaporation deposition process 39
Figure 3.2 The PROVAC PRO 500S metal evaporator at the Delft University of Technology 39
Figure 3.3 Pulsed Laser Deposition system 41
Figure 3.4 Pulsed laser deposition setup at the Thin Film Laboratory (University of Palermo) 41
Figure 3.5 Radio frequency plasma enhanced chemical vapor deposition setup at Delft University of Technology 42
Figure 3.6 X-ray photoelectron spectroscopy setup at the Institute for the Study of Nanostructured Materials (National Research Council) 43
Figure 3.7 Raman spectroscopy setup at Delft University of Technology 45
Figure 3.8 Photothermal deflection spectroscopy setup at Delft University of Technology

.....46
Figure 4.1 X-ray deconvoluted photoelectron spectrum of the Mo 3d binding region, of the 50-nm thick MoO_x sample annealed in air at 100 °C. Al Kα X-ray satellite structures were subtracted before to process the data. 54
Figure 4.2 Raman spectra of the 100-nm thick MoO_x layer as-deposited and after annealing in air at 100 and 250 °C. The curves are displaced vertically in the graph for better visualization. 55
Figure 4.3 Absorption spectra of MoO_x layers 20 nm thick annealed in different atmospheres: a) ambient air, b) hydrogen and c) argon. 56
Figure 4.4 a) Optical bandgap energies of 20-nm thick MoO_x annealed in different atmospheres. b) Conductivity (right axis) and activation energy (left axis) of 20-nm thick MoO_x annealed in air. The dashed lines in b) correspond to the as-deposited reference sample. 57
Figure 4.5 Fit (solid line) of the PDS measurement of absorption coefficient (empty circles) of the 20-nm thick MoO_x sample annealed in air at 200 °C. 60
Figure 4.6 Area of the inter-band defects (left axis) and pre-exponential factor of the polaron absorption (right axis) as a function of the annealing temperature for different annealing ambiances. 61
Figure 4.7 Sketch of the energy band diagram across the c-Si/a-Si:H(i)/MoO_x/TCO stack in a Si heterojunction solar cell under illumination. The dashed lines mark the quasi-Fermi level of electrons, E_{fe}, and holes, E_{fh}. The scale of x-axis is logarithmic for better readability. ..62
Figure 5.1 Ti 2p binding region curve fitting of samples deposited with PO_2 of: a) 1×10^{-3} mbar, b) 2×10^{-2} mbar. 77
Figure 5.2 O 1s binding region curve fitting of samples deposited with PO_2 of: a) 1×10^{-3} mbar, b) 2×10^{-2} mbar. 78
Figure 5.3 a) Raman spectra of the deposited TiO_x samples for different PO_2 (in mbar) and deposition temperature (mean thickness of 155 nm); b) Raman spectrum of the TiO_x sample deposited at 400°C with $PO_2=1\times10^{-2}$ mbar (thickness of 35 nm). 79
Figure 5.4 Absorption spectra for TiO_x samples deposited at different deposition temperatures and pressures (mbar) 80
Figure 5.5 Absorption spectrum deconvolution for the TiO_x sample deposited at $PO_2=1\times10^{-3}$ at 200°C 82
Figure 5.6 Defects area of the distributions centered 1 eV below the conduction band (a) and pre-exponential factor of the polaron absorption (b) in function of the oxygen deposition pressure at ambient temperature and 200 °C. 84

Figure 6.1 Sketch of the HJT solar cell with a) TMO-based hole selective contact, b) TMO-based electron selective contact, ... 95
Figure 6.2 Solar cell prototype: a) back contact, b) top contact 95
Figure 6.3 Transmissivity spectra of the MoO_x films on a quartz substrate for different deposition pressures (mbar) 96
Figure 6.4 Transmissivity spectra of the WO_x films on a quartz substrate for different deposition pressures (mbar) 96
Figure 6.5 Transmissivity spectra of the TiO_x films on a quartz substrate for different deposition pressures (mbar) 97
Figure 6.6 J-V characteristics of the MoOx-based heterojunction solar cells against the different oxygen pressures (mbar) 99
Figure 6.7 J-V characteristics of the WO_x-based heterojunction solar cells against the different oxygen pressures (mbar) 99
Figure 6.8 J-V characteristics of the TiO_x-based heterojunction solar cells against the different oxygen pressures (mbar) 100
Figure 6.9 Equivalent circuit of a heterojunction (HJT) solar cell with a series Schottky junction (SJ) 101
Figure 6.10 Fitting of the J-V characteristic of the solar cell with MoO_x deposited at $PO_2 = 10\times10^{-2}$ mbar. 102
Figure 6.11 Fitting of the J-V characteristic of the solar cells with WO_x deposited at $PO_2 = 3\times10^{-2}$ mbar. 103
Figure 6.12 Fitting of the J-V characteristic of the solar cells with TiO_x deposited at $PO_2 = 1\times10^{-3}$ mbar. 103

List of the Tables

Table 2.1 Performances of the champion cell exploiting the MoO_x contact [16].....20
Table 2.2 Performances of the champion cell exploiting the WO_x contact [19].....22
Table 2.3 Performances of the champion cell exploiting the V_2O_5 contact [23].....24
Table 2.4 Performances of the champion cell exploiting the NiO:Cu (27.1% Cu content) contact [28].....26
Table 2.5 Performances of the champion cell exploiting the ATOM contact [33].....29
Table 2.6 Performances of the champion cell exploiting the ZnO contact [38].....31
Table 4.1 Optical energy gap extracted with different models from the absorption coefficient of the 20-nm thick MoO_x films annealed at different temperatures and in different annealing ambiances.....58
Table 4.2 DOS parameters extracted from the deconvolution of the absorption coefficient for the 20-nm thick MoO_x films annealed at different temperatures and in different annealing ambiances.....60
Table 5.1 Constant C values for different deposition conditions.....75
Table 5.2 Tauc gap and Urbach energy evaluation.....81
Table 5.3 The density of states and small polaron parameters for different deposition conditions.....82
Table 6.1 Optical energy gap.....98
Table 6.2 MoO_x Solar Cell Parameters.....103
Table 6.3 WO_x Solar Cell Parameters.....104
Table 6.4 TiO_x Solar Cell Parameters.....104

List of the Equations

(1.1)....4
(1.2)....6
(3.1)....43
(4.1)....50
(4.2)....51
(4.3)....52
(4.4)....52
(6.1)....97
(6.2)....101
(6.3)....101
(6.4)....101
(6.5)....102

Acknowledgement

After these years as a PhD student, there are numerous people to thank for their work and support.

First, I would like to thank my supervisor, Prof. Isodiana Crupi, who gave me the prospect to start this journey in the research field. You generously guided me in any aspect of my career with constant trust and support.

I wish to thank my supervisors at the Photovoltaic Materials and Devices at the Delft University of Technology, Prof. Miro Zeman, Prof. Olindo Isabella and Dr. Paul Procel. I also would like to thank the researchers and the PhD students of the PVMD group, Rudi, Guangtao, Luana, Gianluca, Robin, Yifeng, Manvika, Yudai, Andres, Nasim, Rita, Carlos, for welcoming me with your friendship and making me feel like one of you.

I would like to thank the evaluators of this PhD thesis Prof. Manuel João Mendes and Prof. Selcuk Yerci, for their timing suggestions and for their appreciation to my research project.

Thanks to Prof. Roberto Macaluso, Prof. Mauro Mosca, Prof. Giuseppe Lullo and Prof. Gianpaolo Vitale from the University of Palermo for the productive moments of discussion and collaboration.

I wish to thank Prof. Antonino Gulino and Prof. Salvatore Mirabella from the University of Catania for their fruitful collaboration in the experimental field.

I sincerely wish to thank the PhD and Master students at the University of Palermo, Federico, Danilo, Francesco, Gero, Marco, Antonino, fellows for this path through experiments and study jointly with moments of lightness and cheeriness.

Finally, my family and my fiancée Agata, you shared with me this whole experience, supporting me in the hard times and helping me overcome every obstacle.